

# REPORT DOCUMENTATION PAGE

*Form Approved*  
*OMB No. 0704-0188*

Public reporting burden for this collection of information is estimated to average 1 hour per response, including the time for reviewing instructions, searching existing data sources, gathering and maintaining the data needed, and completing and reviewing this collection of information. Send comments regarding this burden estimate or any other aspect of this collection of information, including suggestions for reducing this burden to Department of Defense, Washington Headquarters Services, Directorate for Information Operations and Reports (0704-0188), 1215 Jefferson Davis Highway, Suite 1204, Arlington, VA 22202-4302. Respondents should be aware that notwithstanding any other provision of law, no person shall be subject to any penalty for failing to comply with a collection of information if it does not display a currently valid OMB control number. **PLEASE DO NOT RETURN YOUR FORM TO THE ABOVE ADDRESS.**

<b>1. REPORT DATE (DD-MM-YYYY)</b> 28-02-2010		<b>2. REPORT TYPE</b> Final Technical Report		<b>3. DATES COVERED (From - To)</b> 01-06-2006 to 11-30-2010	
<b>4. TITLE AND SUBTITLE</b> Damage Threshold Characterization in Structural Composite M t i Materials and Composite Joints				<b>5a. CONTRACT NUMBER</b>	
				<b>5b. GRANT NUMBER</b> FA9550-06-1-0444	
				<b>5c. PROGRAM ELEMENT NUMBER</b>	
<b>6. AUTHOR(S)</b> Mandell, John F., Agastra, Pancasatya, Cairns, Douglas S., Badaliane, Robert, Sears, Aaron				<b>5d. PROJECT NUMBER</b>	
				<b>5e. TASK NUMBER</b>	
				<b>5f. WORK UNIT NUMBER</b>	
<b>7. PERFORMING ORGANIZATION NAME(S) AND ADDRESS(ES)</b> Montana State University 307 Montana Hall Bozeman MT 59717-0001				<b>8. PERFORMING ORGANIZATION REPORT NUMBER</b>	
<b>9. SPONSORING / MONITORING AGENCY NAME(S) AND ADDRESS(ES)</b> USAF, AFRL AF Office of Scientific Research 875 N. Randolph St. Rm. 3112 Arlington VA 22203				<b>10. SPONSOR/MONITOR'S ACRONYM(S)</b> AFOSR	
				<b>11. SPONSOR/MONITOR'S REPORT NUMBER(S)</b>	
<b>12. DISTRIBUTION / AVAILABILITY STATEMENT</b> unlimited/ unclass					
<b>13. SUPPLEMENTARY NOTES</b>					
<b>14. ABSTRACT</b> <p style="text-align: center;"><b>Abstract</b></p> <p>This program consisted of three tasks related to damage thresholds. Task A explored test methods for characterizing fatigue damage thresholds in resin infused laminates through a complex structured coupon containing ply drops, representative of large composite structures. The complex coupon provides a context for comparing different infusion resins which is economical, but representative of complex structure. Test results and simulations for damage growth and damage thresholds under reversed fatigue loading are given for several types of infusion resins. Task B explored the potential of qualifying new material damage thresholds with multi-axial testing, wherein the material constitutive response in multi-axial strain space is an empirical parameter instead of an assumed functional form. The onset of damage, plus damage progression was monitored for fiberglass/epoxy and carbon fiber/epoxy laminates. A damage metric, known as Dissipated Energy Density (DED) was developed, as well as nonlinear constitutive relationships for continuum based finite element modeling. In Task C a methodology for adhesive joint characterization using the geometry independent nonlinear constitutive behavior of the adhesives from joint tests was developed in conjunction with Boeing. This methodology enabled the use of dissipated strain energy density as the metric to evaluate onset of damage and growth in strain space, for FM300 adhesive with aluminum and carbon/epoxy joints.</p>					
<b>15. SUBJECT TERMS</b> Composites, Adhesives, Damage, Failure Criteria, Fatigue Thresholds					
<b>16. SECURITY CLASSIFICATION OF:</b>			<b>17. LIMITATION OF ABSTRACT</b> UU	<b>18. NUMBER OF PAGES</b> 62	<b>19a. NAME OF RESPONSIBLE PERSON</b> John F. Mandell
<b>a. REPORT</b> UU	<b>b. ABSTRACT</b> UU	<b>c. THIS PAGE</b> UU			<b>19b. TELEPHONE NUMBER (include area code)</b> (406)994-4543

# **Damage Threshold Characterization in Structural Composite Materials and Composite Joints**

John F. Mandell, Pancasatya Agastra, Douglas S. Cairns, Robert Badaliane and Aaron Sears

Montana State University, Bozeman, Montana

Final Technical Report, for FA9550-06-1-0444, AFOSR/DEPSCOR 06

Program Manager: Byung –Lip Lee

## **Abstract**

This program consisted of three tasks related to damage thresholds. Task A explored test methods for characterizing fatigue damage thresholds in resin infused laminates. The approach was to develop a complex structured coupon containing ply drops which is representative of large complex composite structures with tapered thickness. The complex coupon provides a context for comparing different infusion resins which is economical, but representative of complex structure. Test results and simulations for damage growth and damage thresholds under reversed fatigue loading are given for several types of infusion resins, demonstrating significant effects of resin toughness and fatigue crack resistance.

Task B explored the potential of qualifying new material damage thresholds with multi-axial testing, wherein the material constitutive response in multi-axial strain space is an empirical parameter instead of an assumed functional form. The onset of damage, plus damage progression was monitored for fiberglass/epoxy and carbon fiber/epoxy laminates. A damage metric, known as Dissipated Energy Density (DED) was developed for these materials, as well as nonlinear constitutive relationships for continuum based finite element modeling. A low cost Digital Image Correlation (DIC) procedure was developed to determine onset of damage and damage progression. This work shows great promise for efficiently characterizing new materials for primary structural applications.

In Task C a methodology for adhesive joint characterization using the geometry independent nonlinear constitutive behavior of the adhesives from joint tests was developed. Furthermore, this methodology enabled the use of dissipated strain energy density as the metric to evaluate onset of damage and growth. The method treats the constitutive response as an empirical function of the strain space. The nonlinear response of FM300 was characterized using this method for both aluminum and carbon/epoxy joints.

## **Table of Contents**

Task A. Fatigue Thresholds in Complex Composite Structures.....	3
Task B. Demonstration of Energy Methods for Determining Onset of Damage Under Multi-axial Static Loads in Laminates and Adhesive Joints.....	24
Task C. Characterization of Adhesives and Damage Growth in Joints.....	38

# **TASK A. FATIGUE THRESHOLDS IN COMPLEX COMPOSITE STRUCTURES**

**John F. Mandell and Pancasatya Agastra**

## **Summary**

Complex composite structures fabricated by resin infusion processing are of increasing importance in many applications. These structures are typified by multidirectional reinforcement using knitted, stitch bonded or woven fabrics, and often containing ply drops for thickness tapering. Resins are low viscosity, often with property limitations relative to prepregging resins. Local damage development at locations like ply drops tends to be a combination of in-plane resin cracking and ply delamination. An approach to fatigue based design with these structures is through establishing thresholds for macroscopic damage growth over the service lifetime.

A complex structured test coupon has been developed to represent a simplified version of the substructure around ply drops; the coupon is relatively easy to fabricate and test, including tension, reversed and compression loading in fatigue [1, 2]. The dense, heavy fabrics used are typical of large scale composite structures like wind turbine blades, where fatigue performance is critical, and resin infusion materials and processing have evolved significantly in recent years. The complex coupon is used to compare the performance of five types of commercial resins, and several fabrics and ply drop geometries. The effects of these variables on damage growth are quantified for static and fatigue loading, showing significant effects of the resin. Resin types included in this study are unsaturated polyester (UP), toughened and un-toughened vinyl ester (VE), epoxy (EP) and polydicyclopentadiene (pDCPD). Testing for damage thresholds has been included for several resins under reversed loading.

The strain energy release rates for delamination under pure Modes I and II, and mixed-mode have also been determined using established test methods, as have the in-plane static and fatigue properties. Based on the geometry and in-plane and interlaminar properties, a simulation of the damage growth under static loading has been developed using ANSYS finite element modeling. Simulation results are consistent with the experimental damage growth results, and are helpful in relating the performance back to more fundamental properties such as the pure and mixed mode delamination tests, and, in turn, to resin properties. The simulation study also identifies parameters to which ply drop delamination resistance is sensitive, including: variations in elastic constants related to fiber content variations, assumed and actual boundary conditions, resin cracking in off-axis plies and representation of pure and mixed mode delamination data. Strain fields and strain energies are also explored at several stages of damage evolution near critical fatigue threshold conditions.

## INTRODUCTION

Large scale, complex composite structures typically contain a variety of structural details which can compromise blade performance. Local material properties are affected by variations in fiber content and alignment. Geometric features and material discontinuities as in materials transition areas complicate local stress fields, often introducing significant third-dimensional stresses which can lead to ply delamination. Resin selection has generally been focused on performance in relatively simple laminate coupons with reinforcing fabrics and process parameters representative of manufacturing by resin infusion. The approach used in this program has been to develop a test coupon which is representative of the more complex structural details in blade construction, where resin dominated failures occur in service, and which is still relatively inexpensive to fabricate and test compared to full substructure tests [1, 2]. This allows the evaluation of multiple resin options and geometric details like ply drop thickness and edges in a realistic structural context.

A ply drop is a structural detail integrated into the thick laminates of composite structures to provide thickness tapering in applications such as helicopter flex beams and wind turbine blades. Stress concentration arising at this structural detail can lead to ply delamination and loss of structural integrity [3, 4]. Ply drops have been the subject of many studies in aerospace composite applications [5, 6] as well as wind turbine blades [3, 7-9]. Standard tests cited later give the resistance to ply delamination,  $G_{Ic}$  and  $G_{IIc}$  for pure opening and shearing modes, which are a strong function of the resin toughness [1, 10]. In a composite structure the behavior is more complex than for simple pure mode delamination tests, with the controlling strain energy release rates following mixed opening and shearing modes, and depending on geometry and associated damage development such as matrix cracking in off-axis plies which interacts with ply delamination [1, 3]. While results from the test coupon can be interpreted directly in terms of knockdowns on allowable strains, finite element modeling is required to relate the structural response to more basic in-plane and interlaminar properties, which has been a part of this study.

Several variables affecting delamination at ply drops for thick fiberglass laminates have been explored in the experimental part of this work, and in associated studies with carbon and glass prepregs [1, 11]: resin and fabric types, ply drop thickness (number of individual plies dropped at a single position), applied load level, and damage growth under tensile, compressive, and reversed-loading in fatigue. Taken together, these represent a broad range of parameters commonly encountered in composite structures.

Finite element modeling has been used both to design the test coupon and to simulate damage growth. Coupon design, reported in more detail in References 1 and 2, was focused on minimizing strain gradients across the thickness due to bending of the non-symmetric geometry. As indicated in Figure 1 for a case with two ply drops (total of 2.6 mm dropped unidirectional material), strains across the thickness on the thin side vary by less than 10% when grip lateral movement is effectively constrained. The low strain variation across the thickness allows the test results to be incorporated as a design strain knockdown, rather than requiring a fracture mechanics based design strategy.

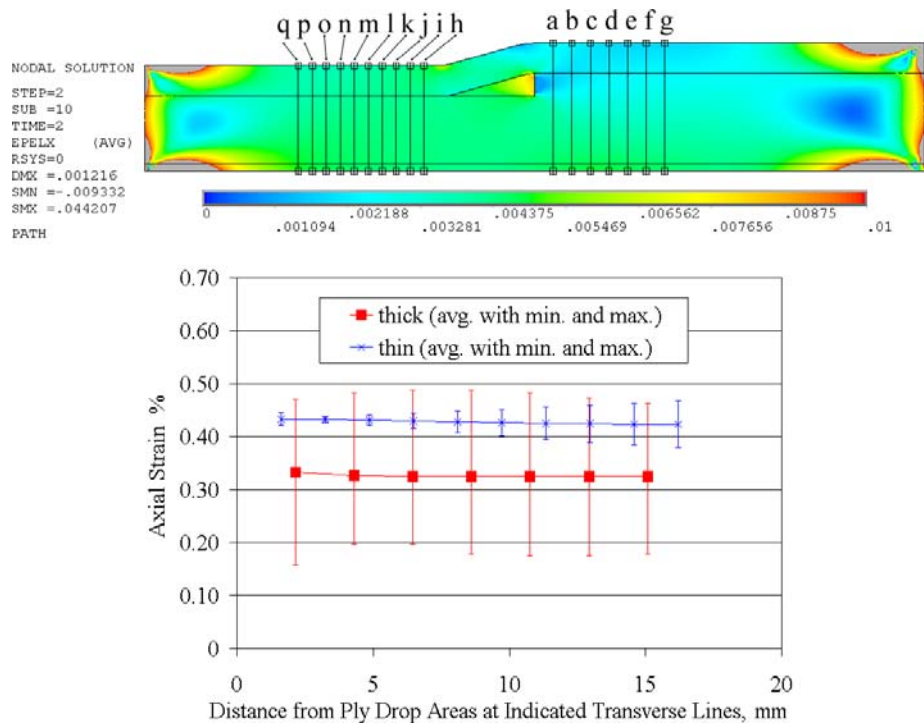


**Figure 1. Axial strain distribution (top), and line plots across thickness at indicated axial locations from FEA for a tensile force of 44.5 kN [1, 2].**

Simulation of damage growth based on experimental observations of damage geometry and basic materials properties has been carried out for static loading. Due to complications associated with fatigue damage growth modeling in complex structures, the fatigue case is being approached through characterizing threshold and near-threshold conditions for significant damage growth. Validated simulations are a key link in relating more basic material properties and geometric features to damage growth, and have been used successfully for delamination problems in composites [12].

## EXPERIMENTAL METHODS

### Materials

Laminates representing the separate components of the complex coupons were tested in addition to the complex coupon laminates containing ply drops. Three types of laminates were fabricated and tested:

- 1) Standard laminates. Unidirectional and biaxial laminates were tested to obtain ply input data and as baseline fatigue cases for comparison to the complex coupon results.
- 2) Delamination laminates. Unidirectional laminates with simulated starter cracks were used in standard delamination tests to obtain  $G_{Ic}$ ,  $G_{IIc}$  and mixed mode data for use in the simulations as well as basic resin comparisons.
- 3) Ply drop laminate. Multidirectional laminates with ply drops for complex coupons.

All laminates were manufactured using vacuum bag resin infusion as summarized in Figure 2. The vacuum bag components are given in Table 1. The aluminum mold was coated with mold release prior to laying up the components. Vacuum pressure of ~640 mm Hg was applied prior to injection to hold everything in place. Table 2 gives the resins and post cure temperatures and Table 3 gives the E-glass reinforcing fabrics. The pDCPD is a new type of thermoset infusion resin with high toughness and low viscosity [1, 13]. Standard laminates without ply drops used flow media on the top only; delamination laminates used an added caul plate on top and flow media top and bottom, with Nylon film crack starter strips; and the complex coupon laminates included ply drops in the top uni fabric plies, under the surfacing biax plies (Figure 2). A typical ply drop panel with four plies dropped at the same location is shown in Figure 3, and cross-sections of the complex coupons with the two different biax fabric are shown in Figure 4.; note that the unidirectional Vectorply fabric actually contains a small amount of 90° strand as backing (Table 3), so that the ply is designated as 0/90. Reference 1 gives local fiber contents corresponding to Figure 4, used in the simulations.

The resin and its components were mixed according to the manufacturer’s recommendation. To minimize micro bubble introduction, a special impeller for viscous resin Jiffy Mixer LS-1 and mixing speed was kept at 300 RPM for 2.6 L resin, and 500 RPM for 4.3 L. Mixing time was five minutes, with an additional five minutes at rest to remove entrapped air bubbles. Injection time varied from 3-15 minutes, depending on the size of the laminates. Laminates were infused at room temperature maintained at ~18°C, cured at this temperature for 24 hours, and postcured for another 24 hours at a prescribed temperature summarized in Table 2.

**Table 1. Molding materials**

Mold	Aluminum 6061 plate, 61 cm × 90 cm × 12.7 mm
Mold Release	Loctite Frekote 44-NC Mold Release Agent
Release Ply	Airtech Release Ply Super F, at top and bottom of laminate
Flow Media	Airtech Greenflow 75, two layers, and 9.5mm-ID Polyethylene spiral wrap
Vacuum Bag	Airtech Vacuum Bag Wrightlon 7400, 76µm thick
Tacky Tape	Airtech AT-200Y
Crack Starter	Richmond Aircraft Products, Inc. VAC-PAK® HS 8171-6 Co-Extruded High Temperature, Nylon 6 Film, 50µm thick

**Table 2. Resin type and post cure schedule**

Resin Type	Resin	24-hr Post Cure Temp.
Epoxy EP-1	Hexion MGS RIMR 135/MGS RIMH 1366	90°C
Polyester UP-1	U-Pica/Hexion TR-1 with 1.5% MEKP	90°C
Vinyl ester VE-1	Ashland Derakane Momentum 411-350 with 0.1% CoNap, 1.0% MEKP, and 0.02 phr 2,4-Pentanedione	100°C
Toughened vinyl ester, VE-2 FIX	Ashland Derakane 8084 with 0.3% CoNap and 1.5% MEKP	90°C
pDCPD (poly-Dicyclopentadiene)	Materia Inc.	N/A

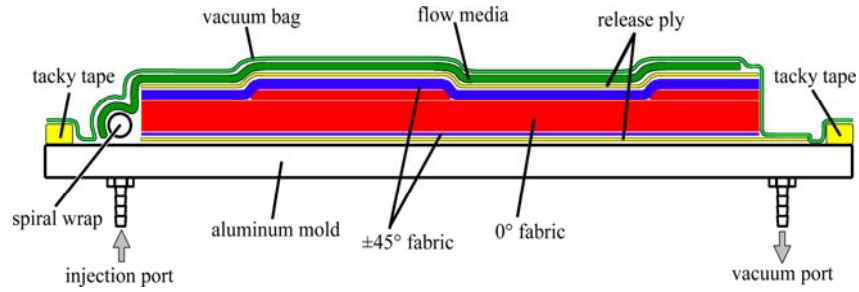


**Figure 2. Infusion processing of laminates with ply drops**

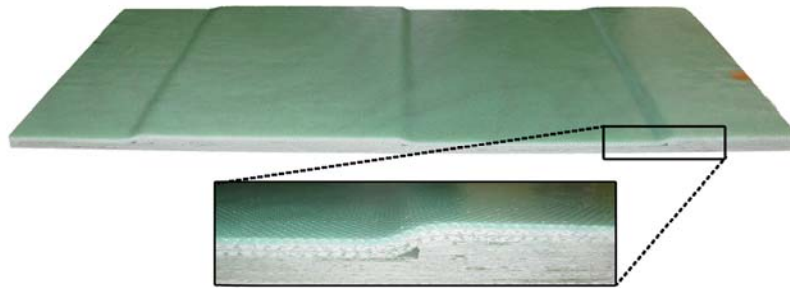


**Figure 3. Typical ply drop laminate panel with four plies dropped at single locations [1, 2] (showing flow media on top)**



**Figure 4. Cross-sections (sectioned at 90°) of complex laminates with two ply drops, thick side, layup from top surface [(±45)<sub>4</sub>/(90/0/0/90)<sub>4</sub>/(±45)]; Fabric M ±45's (left), Fabric L ±45's (right).**

**Table 3. Fabric Definition**

Fabric Type	Manufacturer and Designation	Fiber Areal Weight, g/m <sup>2</sup>						
		Total	0°	90°	-45°	+45°	mat	stitch
Unidir. 0/90 (Fabric D)	Vectorply E-LT-5500	1875	1728	114	0	0	0	33
Biaxial ±45 (Fabric M)	Fiber Glass Ind. (FGI) SX-1708	847	0	0	292	292	258	6
Biaxial ±45 (Fabric L)	Saertex VU-90079-00830-01270-000000	829	0	21	401	401	0	6

## Test methods

The complex laminate coupon with ply drops is shown in Figure 5. The development of this specimen geometry has been described elsewhere [1, 2]; Figure 1 indicates the relatively uniform strain field despite the non-symmetry of the geometry. A composite tab was bonded to the thin side of the specimen to level the thickness. The faces to be gripped were then trimmed to a flat and level condition. Thickness and width were measured at 25 mm away from the edge of ply drop on the thin and thick sections. The non-symmetrical complex coupon requires specialized lateral constraint on the hydraulic grips [1].

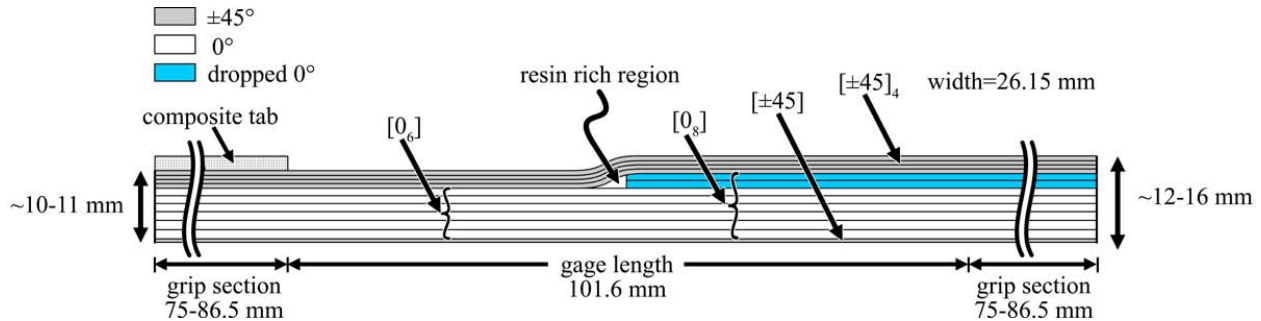


**Figure 5. Complex structured coupon geometry [1, 2]**

Complex coupons with ply drops were tested statically and under fatigue loading at three different R-values,  $R=0.1$  (tensile),  $R=10$  (compressive), and  $R=-1$  (reverse loading), where R is the ratio of minimum to maximum load. Delamination specimens were tested for mode-I, mode-II, and mixed-mode delamination, under displacement control 1.5mm/min. Figure 6 gives mixed mode geometry and test apparatus schematics [14, 15]. These tests follow the ASTM standards with minor modifications: ASTM D5528 for mode I and D6671 for mixed mode; the end notched flexure test was used for mode II [1]. Fatigue test frequency was controlled so that the temperature would not exceed  $5^{\circ}\text{C}$  higher than room temperature. Test specimen surfaces were cooled with a fan. Further test details can be found in Reference 1.

Static testing for the complex coupon specimen was in tension. The load was increased incrementally and crack lengths were measured at each step, until crack length  $L_1$  reached the grip. Figure 7 is a schematic of the damage geometry which was typical for all cases.

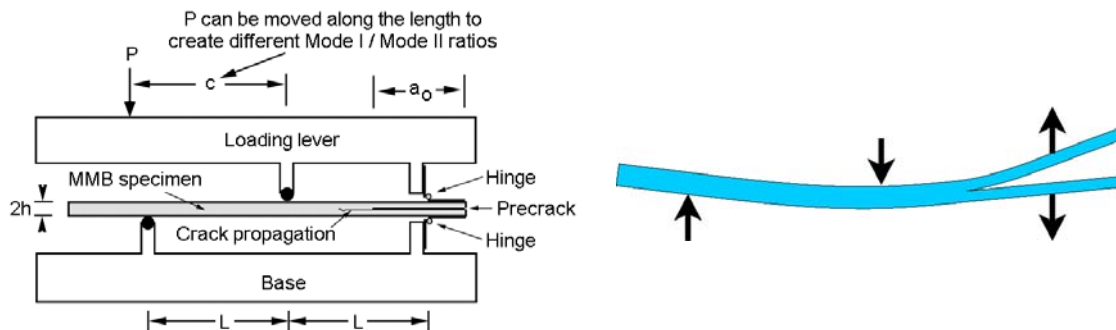


**Figure 6. Mixed mode I and II delamination test geometry**

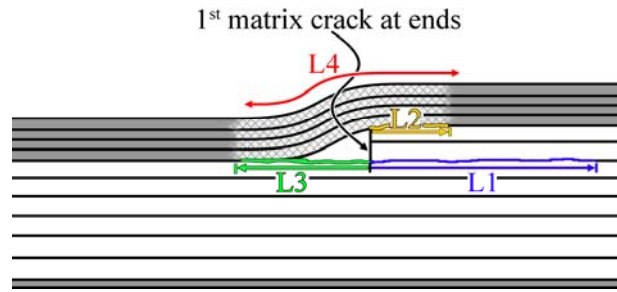


**Figure 7. Damage geometry, where L1, L2, and L3 are delamination cracks and L4 is distributed matrix cracking in the biax plies (adapted from References 1 and 2)**

## SIMULATION METHODS

### Simulation Input

The simulation input was based on experimental data for crack geometry (Figure 7) and material properties either given here or in Reference 1. Observed complex coupon details were included in the model (Figure 8):

- A. Curvature of the overlaying top plies.
- B. Simplification of the junction between the  $\pm 45^\circ$  and the  $0^\circ$  layer
- C. Compaction at the top of the ply drop edge
- D. Resin rich region

Initial simulations reported here assumed crack lengths for L2 and L3 (Figure 7) as 3 mm for higher values of L1 as discussed later. Softening due to the matrix cracking in the off-axis biax plies (L4) was included through a multi-linear elastic stress-strain curve, Figure 9, synthesized from experimental stress-strain curves for fabric M with resins EP-1 and UP-1, which gave nearly identical results [1]. The length of the primary delamination, L1, was assumed in the simulation, and the load to achieve the mixed mode failure criterion was determined. Convergence was difficult when biax modulus changes were included, and this feature was deleted from many runs to reduce run times.

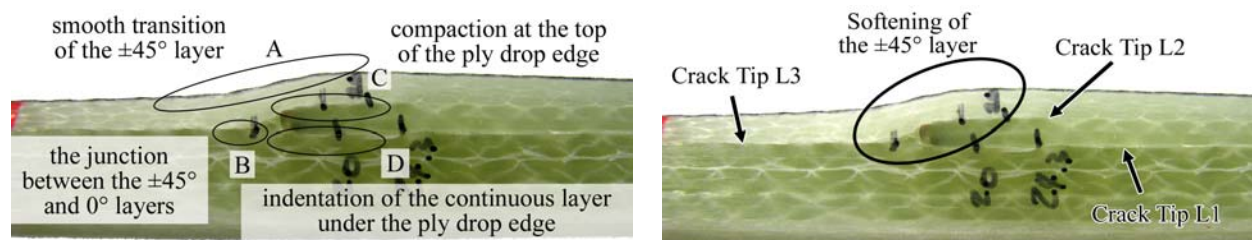


**Figure 8. Ply drop details for the simulation.**

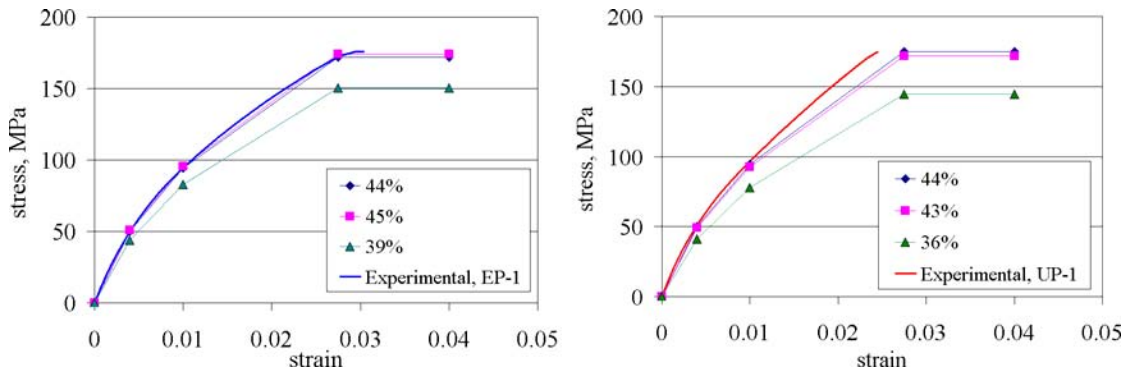


**Figure 9. Multi-linear elastic tensile stress-strain curve for ( $\pm 45$ ) biax fabric M for resins EP-1 (left) and UP-1 (right)**

### Material Properties and Geometry

Figure 10 gives typical element meshes with coordinate systems and material domains. The FEA used ANSYS PLANE82 elements with contact elements (0-friction) on crack surfaces. The elements around the crack tips were sized according to ANSYS recommendation.

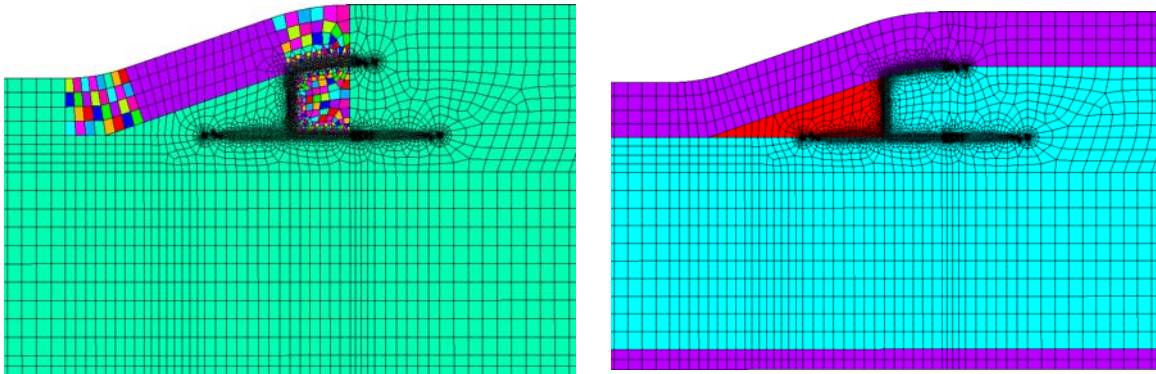


**Figure 10. Finite element model details around the crack tips (left: rotated coordinate system; right: material domains)**

The orthotropic material properties were taken from Reference 1, adjusted for local fiber content variations in particular plies [1] or else were estimated from similar materials [3] where not available. Crack fronts were modeled and the strain energy release rates were calculated using the one-step VCCT method [16].

**Table 4. Material Properties for FE simulation (\*estimated properties from [3]).**

Material Properties	Fabric D 0°	Fabric L ±45	Fabric M ±45	Epoxy Neat Resin
Fiber Volume Content	0.54	0.51	0.44	0
E <sub>X</sub> , GPa	41.80	13.80	13.60	3.20
E <sub>Y</sub> , GPa	7.38*	7.52*	7.52*	X
E <sub>Z</sub> , GPa	14.00	11.80	13.30	
G <sub>XY</sub> , GPa	2.63*	2.83*	2.83*	
G <sub>YZ</sub> , GPa	2.63*	2.83*	2.83*	
G <sub>XZ</sub> , GPa	2.63	9.24	11.8	
ν <sub>XY</sub>	0.280*	0.264*	0.264*	
ν <sub>YZ</sub>	0.280*	0.381*	0.381*	X
ν <sub>XZ</sub>	0.280	0.51	0.55	
Density, kg/m <sup>3</sup>	1924*	1884*	1788*	1190

**Delamination Criterion**

Mixed mode ply delamination is the dominant feature of ply drop behavior. Figure 11 gives typical mixed mode data for two unidirectional fabrics at two fiber content ranges, for three resin types: epoxy (EP), vinyl ester (VE), and unsaturated polyester (UP), from Reference [1], where particular resins and fabrics are identified (fabric D is described in Table 2). The general shape of the mixed mode failure criterion follows that described by Reeder and Crews [14], as related to disruption of planar mode I cracks by hackle formation from the mode II component. Thus, a mode II component allows  $G_I$  to increase above the pure mode  $G_{Ic}$  value. The pure and mixed mode toughness increases for increasing neat resin toughness and decreasing fiber content [10]. Tough resins such as toughened epoxies and thermoplastics, or pDCPD, tend to a linear relationship between  $G_I$  and  $G_{II}$  as [16]:

$$G_I/G_{Ic} + G_{II}/G_{IIc} = 1 \quad [1]$$

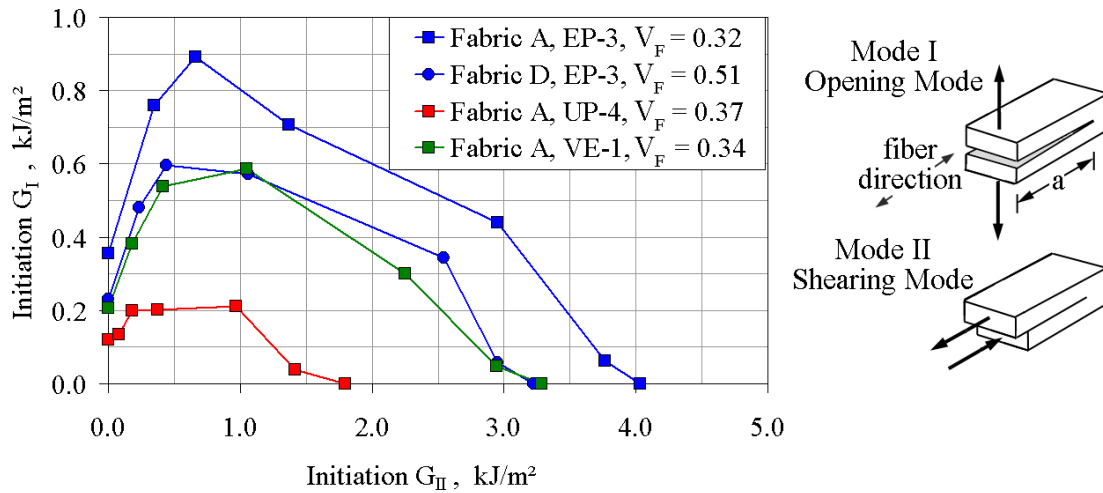


**Figure 11. Mixed mode delamination results for various resin types and fiber contents [1, 15].**

## RESULTS

### Experimental

#### *Delamination Tests*

Pure mode critical strain energy release rates for the various resins with Fabric D are given in Table 5. The  $G$  values are calculated for initial crack growth from the Nylon film using the 5% offset method described elsewhere [1, 3]. Consistent with Figure 11, the general ordering of toughness from low to high is polyester, vinyl ester and epoxy, as reported earlier [1-3], the differences between resins are significant. The Vectorply ELT 5500 fabric (D) contains a small amount of  $90^\circ$  backing strands on the side referenced as 90, so the delamination interface could be 0/0, 90/90 or 0/90. Table 5 contains toughness values for 0/0 and 90/90 only; toughness values are generally higher for the 0/0 interface, where the  $0^\circ$  strands nest, than on the straighter 90/90 interface (Figure 4). The irregular 90 face of the fabric, with occasional backing strands, results in high scatter for this interface. The primary delamination for the complex coupon, L1 (Figure 7), is on a 90/90 interface for the layup used in that test. The results in Table 6 also indicate that the toughened vinyl ester, VE-2, reaches similar toughness levels to the epoxy. Also notable is the pDCPD resin, which is ductile in behavior, and reaches very high  $G_{Ic}$  levels, similar to highly toughened epoxy or thermoplastic resin laminates like PEEK [17,18]; only the 0/0 interface has been tested for the pDCPD resin. Use of initiation values for  $G_{Ic}$  results in the lowest value for infused fabrics of this type; as the crack extends, mechanisms like fiber bridging can significantly raise the critical  $G_I$  value by several times the initial value, with stronger effects seen for the more brittle resins like polyesters [3]. Mixed mode data for the Fabric D laminates with epoxy EP-1 and polyester UP-1 are given in Figure 12. This figure also illustrates the mixed mode failure criterion used in the simulations.

**Table 5. Pure mode delamination test results. (Numbers in parenthesis are standard deviations for 3-5 tests.)**

Resin	0-0 Interface				90-90 Interface			
	V <sub>F</sub> , %	Initial G <sub>IC</sub> , J/m <sup>2</sup>	V <sub>F</sub> , %	Initial G <sub>IIc</sub> , J/m <sup>2</sup>	V <sub>F</sub> , %	Initial G <sub>IC</sub> , J/m <sup>2</sup>	V <sub>F</sub> , %	Initial G <sub>IIc</sub> , J/m <sup>2</sup>
EP-1	60	303 (40)	60	3446 (201)	62	321 (38)	61	1887 (97)
UP-1	60	166 (17)	60	1662 (200)	62	175 (27)	62	928 (353)
VE-1	64	252 (24)	63	2592 (130)	64	223 (13)	63	1653 (124)
VE-2	61	433 (53)	61	2998 (313)	61	272 (33)	61	1689 (349)
pDCPD	64	1560(241)	64	2728 (305)	---	---	---	---

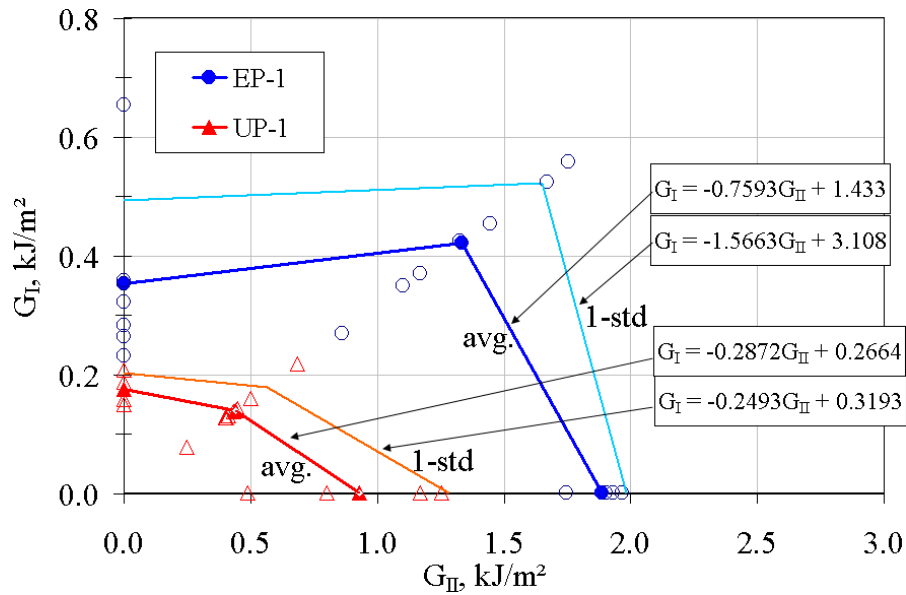


**Figure 12. Mixed mode results for EP-1 and UP-1 resins, fabric D unidirectional laminates, crack positioned on the 90/90 interface, showing delamination criteria assumed in simulations**

### ***Complex Coupon Static Tests***

Figures 13 and 14 give comparisons of the delamination growth curves for the various resins [1]. The results in Figure 13, for biax Fabric M with unidirectional Fabric D, show the same ordering by resin as Figure 11 and Table 5: epoxy, vinyl ester and polyester, from highest to lowest. Load levels are reduced in Figure 14 for the baseline epoxy, EP-1, using the lighter biax Fabric L, which does not contain mat. The pDCPD resin outperforms the epoxy for the longer cracks, where the G<sub>I</sub> component becomes significant, as shown later. The last growth step (highest load) is unstable, so the final point shown represents the highest stable load achieved, but the crack length plotted is the value at crack arrest due to the grips.

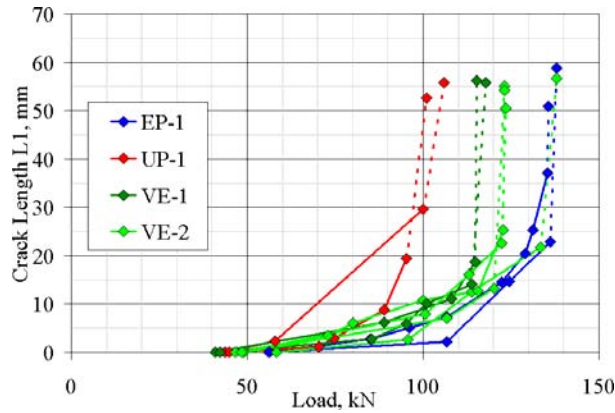


**Figure 13. Static ply drop results for delamination growth, L1, vs. load, various resins, two plies dropped, fabrics M and D.**

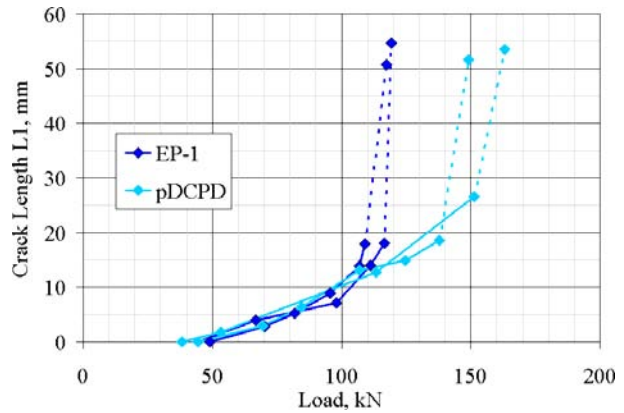


**Figure 14. Comparison of epoxy and pDCPD under static loading, two plies dropped, fabrics L and D.**

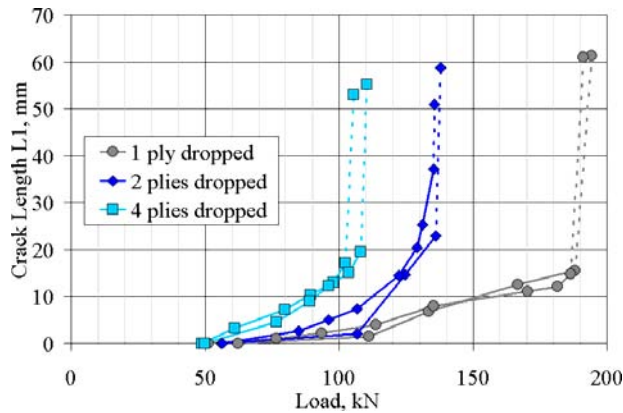


**Figure 15. Effect of number of plies dropped, static tension, fabrics D and M, epoxy EP-1**

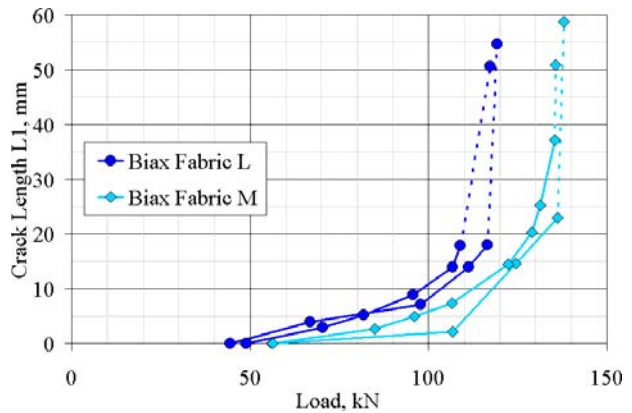


**Figure 16. Effect of biax fabrics L vs. M with unidirectional fabric D and epoxy EP-1, two plies dropped**

Figures 15 and 16 show the effects of the number of plies dropped at the single location, where the total thickness dropped is approximately 1.3 mm/ply. A strong effect of the dropped thickness is evident in Figure 15, as predicted [1]. One result of Figures 14-16 and the corresponding fatigue results is that thickness tapering can be more rapid for the tougher resins, to achieve similar static or fatigue delamination resistance [1, 2]. The results depend on the types and number of plies of fabrics used in addition to the resin effects. The lighter biax fabric L results in delamination at lower loads than fabric M, which has an added layer of mat.

### ***Fatigue Results***

Typical tensile fatigue results ( $R = 0.1$ ) for resin and geometric variations in Figures 16 and 17 show effects which correspond to the respective static Figures 13 and 15. Figure 18 compares epoxy EP-1 with pDCPD under reversed loading fatigue ( $R = -1$ , the most severe case) at three maximum load levels, and Figure 19 gives the corresponding delamination crack growth rates. The pDCPD shows increasing advantage in fatigue at lower loads and longer lifetimes more representative of the wind blade loading environment. Many other static and fatigue results can be found in References 1 and 2.

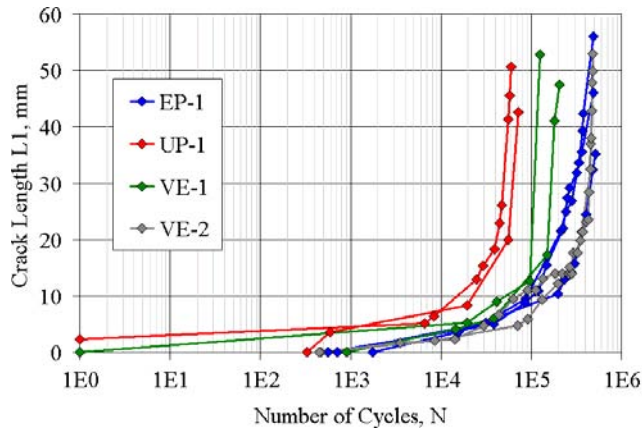


**Figure 16. Fatigue test results with R=0.1 at 44.5 kN maximum load for various resins with two plies dropped, fabrics M and D**

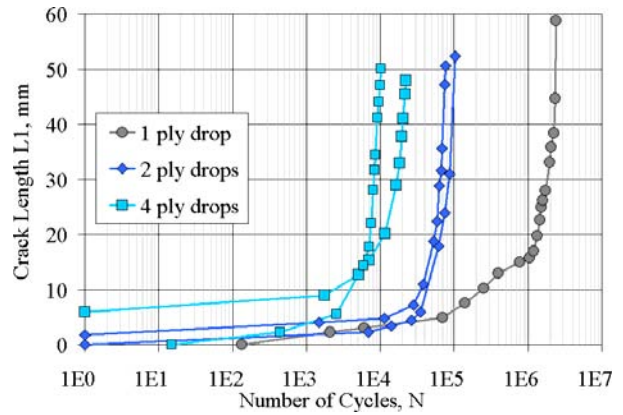


**Figure 17. Effect of number of plies dropped on delamination growth in fatigue, resin EP-1, with a maximum load of 55.6 kN, R = 0.1, fabrics M and D.**

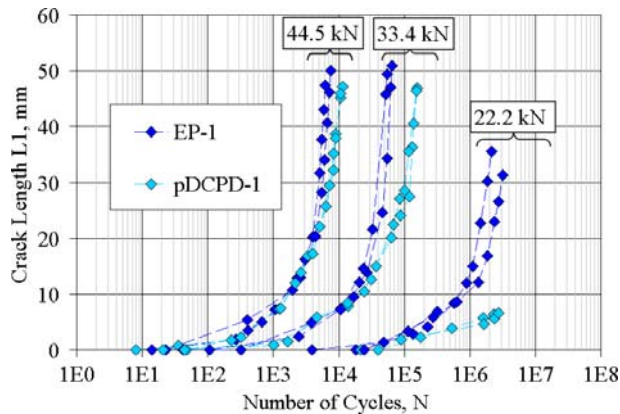


**Figure. 18 Epoxy and pDCPD under reversed loading R=-1, at various maximum load levels, fabrics L and D**

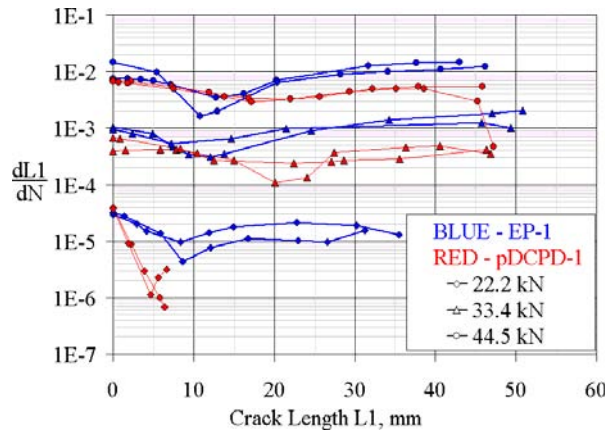


**Figure 19. Crack growth rate,  $dL1/dN$ , vs. crack length for epoxy and pDCPD data in Figure 18**

### Threshold Behavior

Near-threshold results are presented in Figure 20 for reversed loading of complex coupons with three resins: polyester UP-1, epoxy EP-1 and pDCPD. While more detailed testing is required to accurately define crack growth thresholds (see, for example, ASTM E647), these results indicate the load range where crack initiation and growth become very difficult (compare Figure 18). The near-threshold condition is defined here as where the crack extension,  $L1$ , is limited to 5 mm at  $10^6$  cycles. The apparent load and strain range where threshold behavior is apparent are listed in Table 6, along with damage components which were observed by light microscopy. The experimental data indicate that load and strain levels for near-threshold behavior, relative to the baseline epoxy, EP-1, are about 16% higher for pDCPD, and 26% lower for polyester UP-1. At this point the polyester resin laminate also shows significant matrix cracking in the  $\pm 45$  plies, but this is not observed for the epoxy and pDCPD resin laminates. These findings are discussed in Section 4.3 in conjunction with FEA results.

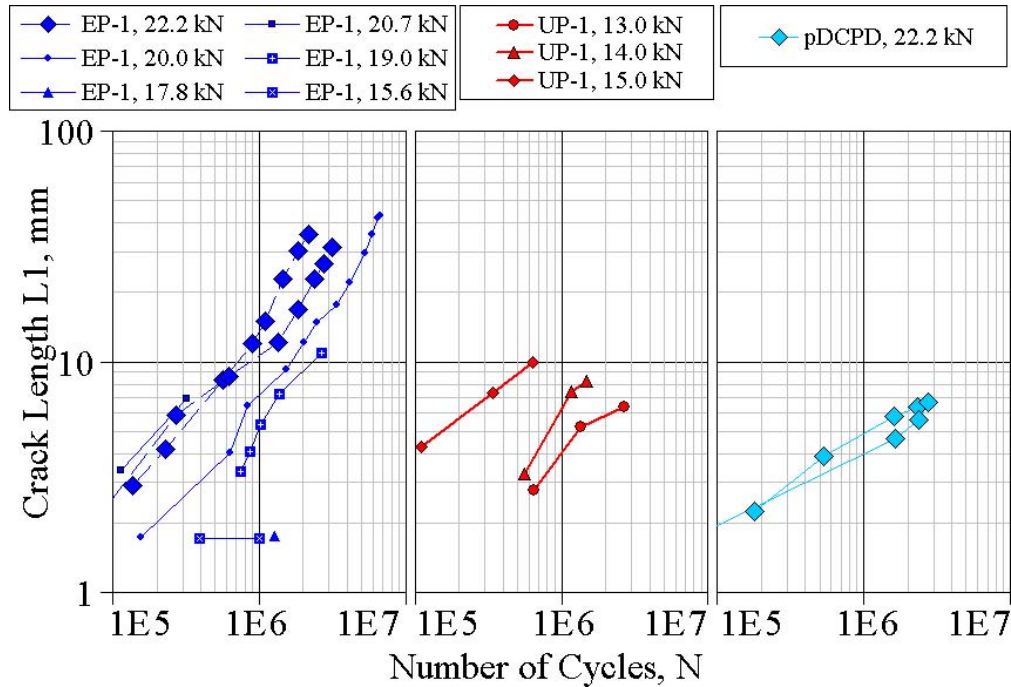


**Figure 20. Near-threshold damage growth results for three resins: epoxy (EP-1), polyester (UP-1) and pDCPD; R = -1, two ply drops, fabrics D and L.**

**Table 6. Near threshold results (5-mm delamination length L1 in  $10^6$  cycles), R = -1, two ply drops, fabrics D and L**

Resin	Near-Threshold Maximum Force, kN, and thin side average strain (%)	Force Change From Epoxy	Observed Damage (Fig. 7)
Epoxy EP-1	19 (0.18%)	—	L1, L2, crack at ply ends
Polyester UP-1	14 (0.13%)	-26%	L1, L2, biax cracking, crack at ply ends
pDCPD	22 (0.21 %)	+16%	L1, crack at ply ends

### Simulation

Initial simulations have been carried out for static loading only, with resins EP-1 and UP-1 and fabrics D and M. Experimental results are given in Figure 13. The simulations were limited to the middle load and crack length (L1) range, and, when included, assumed a length of about 3 mm for the secondary cracks L2 and L3 (Figure 7), which primarily extend further when L1 becomes unstable. As noted earlier, softening of the biax plies was included in selected cases by using the multi-linear stress-strain curve in Figure 9. Early attempts at the simulation produced expected trends, but at significantly lower loads than found experimentally. Careful examination of the experimental setup showed slight lateral movement (at higher loads) of the grip due to the test coupon non-symmetry, before the grip constraint took full effect; lateral movement was on the order of one mm maximum. The boundary conditions were then modified to allow up to 1-

mm lateral movement of the grip above 100 kN load (applying only to the epoxy resin). This modification significantly lowered the  $G_I$  and  $G_{II}$  values for a particular load and crack length, raising the predicted loads to the range observed experimentally (Figure 21 and Table 7). When free lateral movement was allowed the simulated loads were too high due to the reduced  $G_I$  and  $G_{II}$ . FEA values for  $G_I/G_{II}$  ratios in Figure 22 are generally similar to those found for prepreg ply drops by Wilson [18].

Figure 21 indicates good agreement between experimental data and simulated loads for the simulation parameters indicated. The difference between the epoxy and polyester resins is accurately represented by the simulation, primarily through the mixed mode failure criterion difference (Figure 12). Table 7 gives the sensitivity of the simulated loads at 15-mm delamination, L1. In addition to the parameters discussed above, predicted loads are increased by adjusting the failure criterion to the average value plus one standard deviation or adjusting the elastic constants to the measured in-situ ply fiber contents (from the listed values at a slightly lower fiber content), but decreased by the presence of secondary delaminations L2 and L3, or softening of the biax plies following Figure 9.

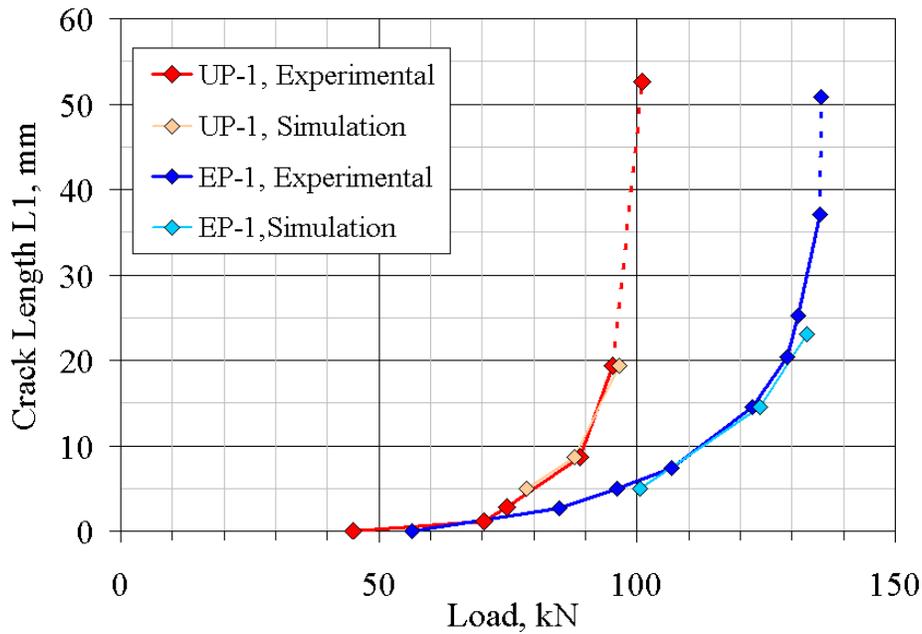


**Figure 21. Simulated vs. experimental static tension results using the average mixed-mode failure criterion, 1 mm lateral displacement limit above 100 kN load, and no L2, L3 or biax softening.**

**Table 7. Sensitivity results for resin EP-1 relative to standard case simulation**

Mixed Mode Criterion	Lateral Movement Allowed	L2 and L3	E's Adjusted For $V_F$	Biax Softening	% Load Change at L1=15 mm
average	1 mm	0	yes	no	0 (std case)
average	free	0	yes	no	+19%
ave.+1 SD	free	0	yes	no	+26%
average	0 mm	0	yes	no	-15%
average	1 mm	3 mm	yes	no	-21%
average	1 mm	0	yes	yes	-24%
average	1 mm	0	no	no	-3%
average	0 mm	3 mm	no	yes	-22%

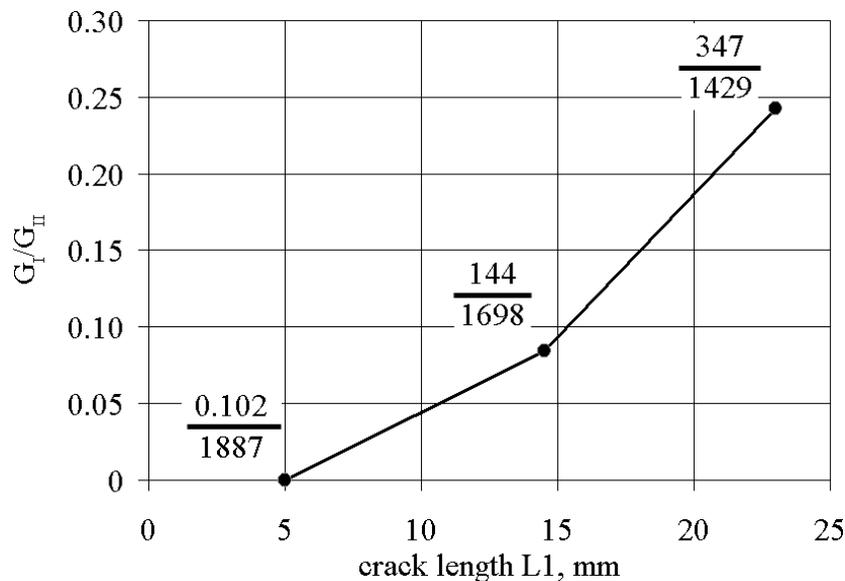


**Figure 22.  $G_I/G_{II}$  ratios during crack growth for EP-1, standard case (1-mm lateral displacement, no L2 and L3, material properties adjusted to experimental fiber volume content).**

### Threshold Analysis

The strain conditions in the near-threshold condition have also been explored. As noted in Figure 22, the L1 crack tip condition approaches pure mode II for small values of L1. Figure 23 gives the axial strain field for damage state which consists only of a crack across the ends of the dropped plies (usually the first damage), and a 3-mm long L1.

Through-thickness static axial strain distributions (for damage states observed in fatigue) at the positions (a-n) indicated in Figure 1 are given for three stages of near-threshold damage progression with resin EP-1 in Figure 24. Two conditions assumed for lateral movement, free and fully constrained, are indicated; the left-side plots are for the thin half of the specimen, the right-side for the thick half. The three stages of near-threshold damage development shown (Figure 7) and the critical load for are: no damage (top, 56.4 kN); matrix crack across the ply

ends (middle, 56.4 kN); and matrix crack across ply ends plus 3-mm L1 with biax ply softening (bottom, 82.4 kN and 93.5 kN for constrained and free movement, respectively). The lowest two critical loads are experimental observations, while the highest is a simulation result, which agrees with experimental data; these are all critical static tension loads for the particular stage of damage development.

The results in Figure 24 trace out strain field evolution as the applied tensile load increases and damage develops. The strains far from the ply drop smoothly increase as the load increases and damage develops. Notable shifts are seen for each stage for the strain close to the ply drop, particularly position (a). While these results do not predict fatigue threshold conditions, they do capture the strain distributions associated with each damage state.

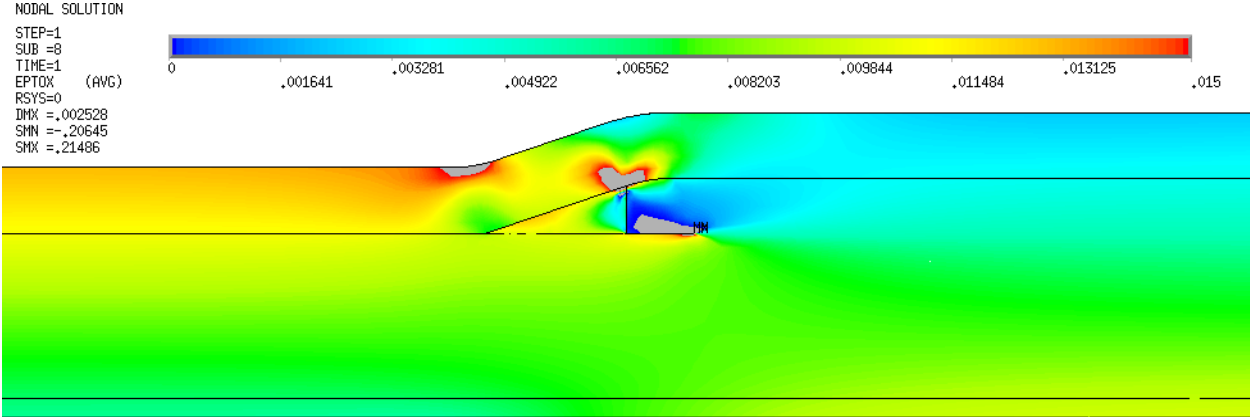


**Figure 23. Axial strain map for 3-mm long L1, 56.4 kN force.**

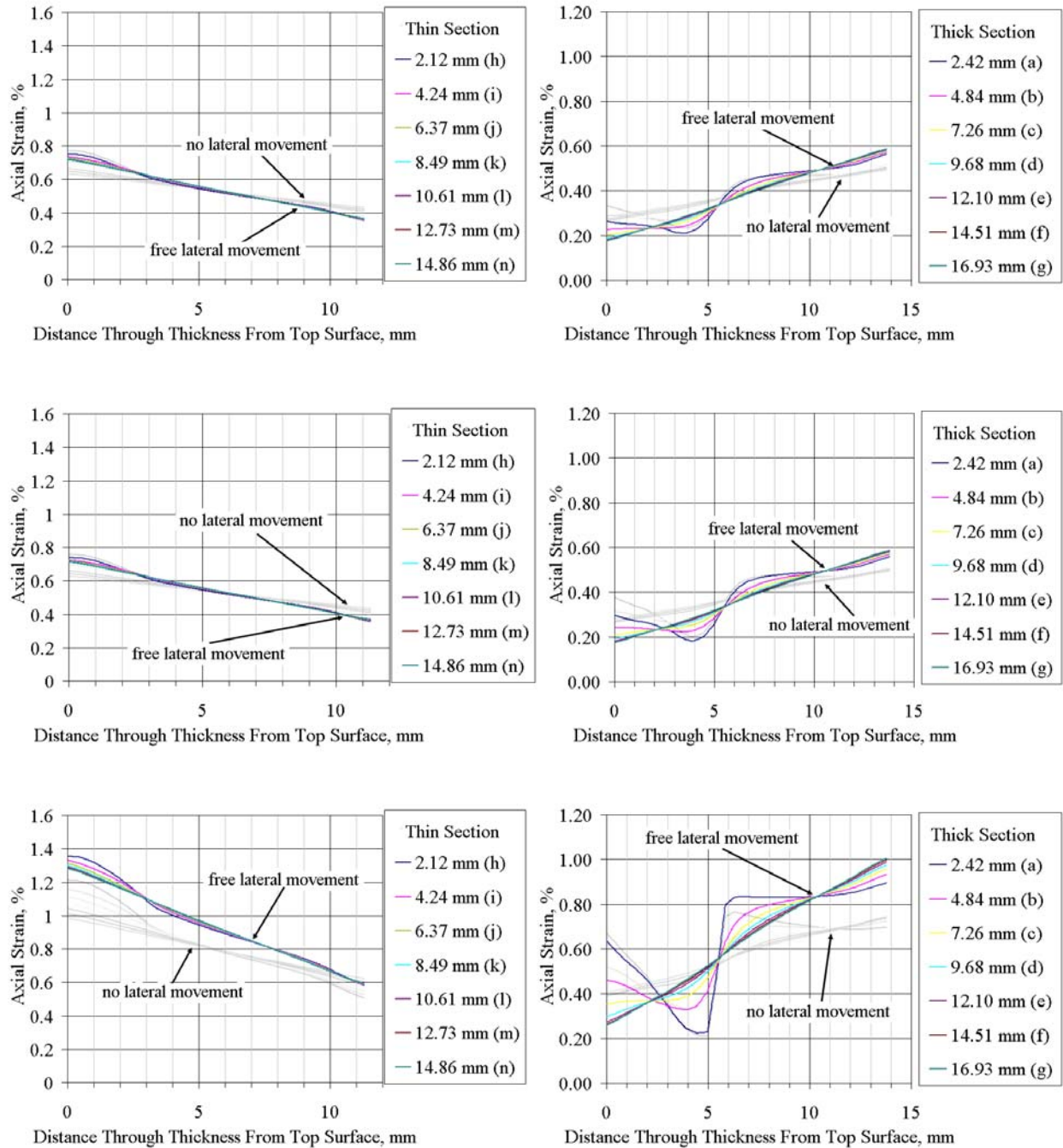


**Figure 24. Through-thickness axial strain distributions along lines (a)-(n) in Figure 1 at the critical load; left, thin side; right, thick side; for the following damage states: no damage, 56.4 kN (top); crack across ply drop ends, 56.4 kN (middle), and L1 of 3-mm with biax softening and crack at ply drop ends, 82.4 kN and 93.5 kN for constrained and free movement, respectively (bottom). Assumed lateral movement either free or constrained as indicated.**

## CONCLUSIONS

This study establishes a new approach to static and fatigue testing of resin infused laminates using complex structured coupons with ply drops, which represent large infused composite structures better than do standard laminate and interlaminar test methods. This approach has been extended to fatigue threshold characterization under this program. The findings of this study provide a more efficient approach to resin selection and internal structure design in an environment of fatigue loading of large, complex infused composite structures, with the potential for improvements in cost, manufacturing and structural integrity.

The experimental results show significant differences between infusion resins for standard delamination tests and delamination at ply drops with the complex structured coupon. Results from both types of tests show the same trend from greatest delamination resistance to poorest: pDCPD, epoxy EP-1, toughened vinyl ester VE-2, vinyl ester VE-1 and polyester UP-1. The results indicate trade-offs between resin toughness and geometric refinement (such as number of plies dropped in a local area), which could impact blade design choices such as steepness of thickness tapering. The fatigue results were consistent with static results in terms of resin and geometric effects. This ordering is also observed for near-threshold reversed loading fatigue conditions for EP, UP and pDCPD resins, and near-threshold loads and strains are determined for each resin. Simulations of static damage growth vs. load, based on measured ply properties adjusted for fiber content and delamination test data, are in general agreement with experimental data for complex coupons containing ply drops. The simulations indicate sensitivity to several test and materials parameters.

## REFERENCES

1. Mandell, J.F., Samborsky, D.D., Agastra, P., Sears, A.T. and Wilson, T.J., "Analysis of SNL/MSU/DOE Fatigue Database Trends for Wind Turbine Blade Materials." *Sandia National Laboratories Contractor Report* (in review, available on [www.coe.montana.edu/composites](http://www.coe.montana.edu/composites)).
2. Agastra, P., Samborsky, D. D. & Mandell, J. F. *50th AIAA/ASME/ASCE/AHS/ASC Structures, Structural Dynamics, and Materials Conference, Paper AIAA 2009-2411*, Palm Springs, CA, May 2009.
3. Mandell, J.F., Samborsky, D.D. and Cairns, D.S., "Fatigue of Composite Materials and Substructures for Wind Turbine Blades," *Contractor Report SAND2002-0771*, Sandia National Laboratories, Albuquerque, NM, 2002.
4. De Charentenay, F.X., "Concluding Remarks on the Application of Fracture Mechanics to Composite Materials," *Application of Fracture Mechanics to Composite Materials*, K. Freidrich, ed., Elsevier, 1989.
5. Trethewey, B.R., Gillespie, J.W., Jr. and Wilkins, D.J., "Interlaminar Performance of Tapered Composite Laminates," *Proceedings of the American Society for Composites, Fifth Technical Conference*, June 11-14, 1990, p. 361.
6. Murri, G.B., Salpekar, S.A., and O'Brien, T.K., *Composite Materials: Fatigue and Fracture (Third Volume)*, ASTM STP 1110, T.K. O'Brien, Ed., American Society for Testing and Materials, Philadelphia, 1991, pp. 312-339.
7. Samborsky, D.D., Wilson, T.W., Agastra, P., and Mandell, J.F., *J. Sol. Energy Eng.*, 2008 130, paper 031001.

8. Cairns, D.S., Mandell, J.F., Scott, M.E., Maccagnano, J.Z., "Design Considerations for Ply Drops in Composite Wind Turbine Blades," *1997 ASME Wind Energy Symposium*, ASME/AIAA, AIAA-97-0953, 1997, pp. 197-208.
9. Mandell, J.F., Cairns, D.S., Samborsky, D.D., Morehead, R.B., and Haugen, D.J., *J. Sol. Energy Eng.*, 2003, 125, paper 009304.
10. Hunston, D.L., Moulton, R.J., Johnson, N.J., and Bascom, W.D., *Toughened Composites*, ASTM STP 937, Norman J. Johnson, Ed., American Society for Testing and Materials, Philadelphia, 1987, pp. 74-94.
11. Wilson, T.J., "Modeling of In-Plane and Interlaminar Fatigue Behavior of Glass and Carbon Fiber Composite Materials," *MS Thesis*, Department of Mechanical Engineering, Montana State University, 2006
12. Krugar, R., and Konig, M., *Composite Materials: Fatigue and Fracture*, ASTM STP 1285, E. A. Armanios, Ed., American Society for Testing and Materials, 1997, pp. 162-178.
13. Edgecombe, B. D., Cruce, C., Stephen, T, McCarthy, T., Mandell, J. F., Samborsky, D. D., Agastra, P. and Wetzel, K. K. , "Effects of a new, high-toughness infusion resin on the fatigue performance and defect-tolerance of glass composite laminates," *AWEA Windpower Conference*, Dallas, May 2010.
14. Reeder, J. R., and Crews, J. H., Jr., "The Mixed Mode Bending Method for Delamination Testing," *AIAA Journal*, vol. 28, 1990, pp. 1270-1276.
15. Agastra, P., "Mixed Mode Delamination of Glass Fiber/Polymer Matrix Composite Materials", *Masters Thesis*, Chemical and Biological Engineering Department, Montana State University, 2003.
16. Raju, I.S., *Engineering Fracture Mechanics* 28:3, 1987, pp. 251-274.
17. Russell, A.J. and Street, K.N., *Toughened Composites*, ASTM STP 937, N. J. Johnston, Ed., American Society for Testing and Materials, Phil., 1987, pp. 275-294.
18. Johnson, W.S. and Mangalgiri, P.D., *Toughened Composites*, ASTM STP 937, N. J. Johnston, Ed., American Society for Testing and Materials, Phil., 1987, pp. 295-315.

# **TASK B. DEMONSTRATION OF ENERGY METHODS FOR DETERMINING ONSET OF DAMAGE UNDER MULTI-AXIAL STATIC LOADS IN LAMINATES AND ADHESIVE JOINTS**

**Doug Cairns, James Schmidt and John Parker**

## **Summary**

It is expensive and time consuming to insert new materials into primary structure. This is especially true of composites and multi-functional materials. In this task, we explored the potential of qualifying new materials with multi-axial testing, wherein the material constitutive response in multi-axial strain space is an empirical parameter instead of an assumed functional form. A special, multi-axial testing machine from previous work was modified for this research. The onset of damage, plus damage progression was monitored for fiberglass/epoxy and carbon fiber/epoxy laminates. A damage metric, known as Dissipated Energy Density (DED) was developed for these materials. Also, nonlinear constitutive relationships were developed for continuum based finite element modeling. A low cost Digital Image Correlation (DIC) procedure was developed to determine onset of damage and damage progression. This work shows great promise for efficiently characterizing new materials for primary structural applications.

# IMPETUS

The insertion of new materials into primary structure is cumbersome and expensive. A typical scenario is shown below in Figure 1 based on Reference [1].

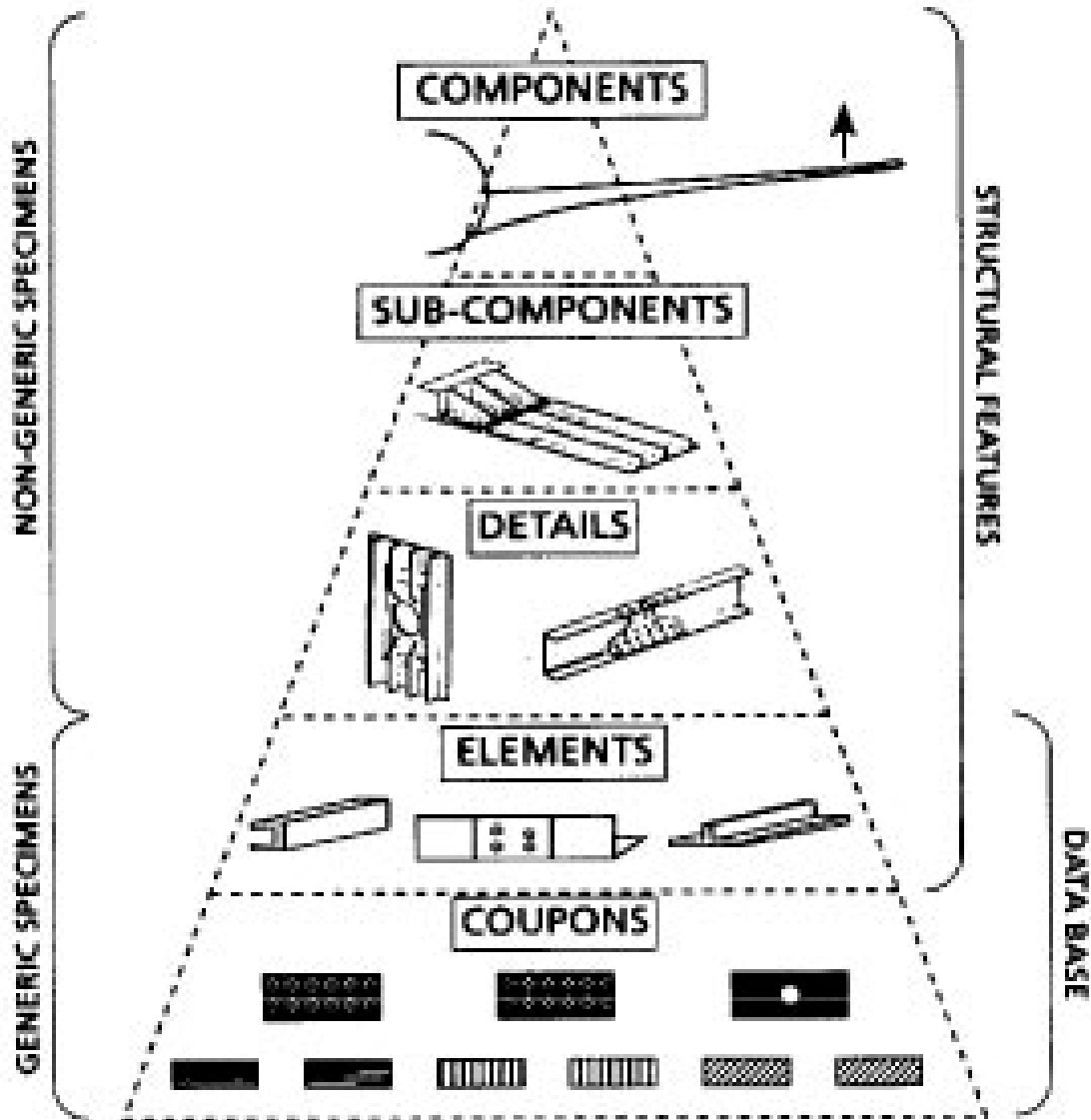
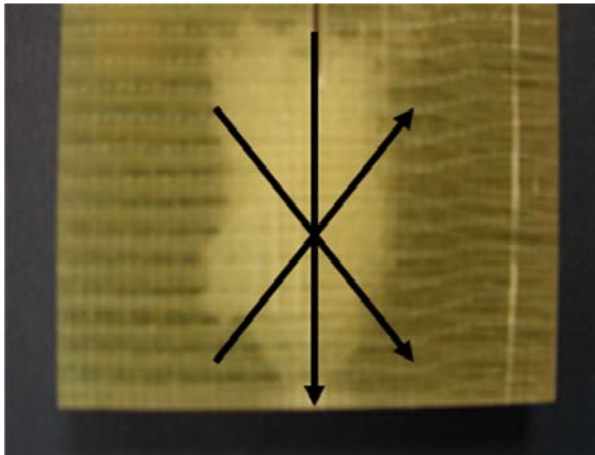


**Figure 1. Building Block Approach for Certifying Composite Materials for Primary Air Force Structure [1].**

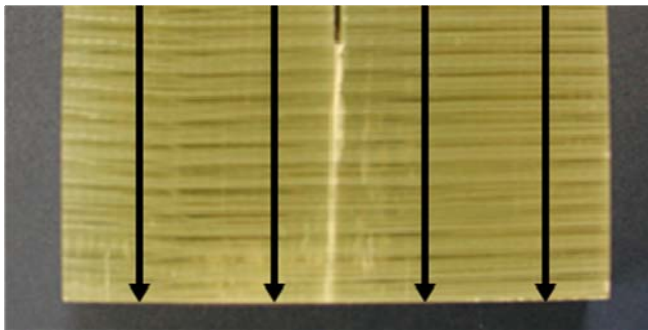
It is difficult to obtain exact industry estimates, but the collaborator for this project, Boeing St. Louis estimates that the cost is over \$80 million dollars to qualify a new material. This has tremendous implications. Even though a material may be much lower cost, it will still take substantial time and money to find its way onto primary structure.

The implications for exciting multifunctional materials are even more profound since these materials may be substantially different than the established materials for primary Air Force structure. Consequently, this research was conducted to streamline the process for inserting new and multifunctional materials into primary DOD structure.

Part of the problem is that there is not a universal failure criterion for composite materials. Hence, many tests are required for certification in Figure 1. An example is shown in Figure 2.



**a) Damage with delaminations**



**b) Fiber/Matrix Damage**

**Figure 2. Different Damage Types, Same Material**

The basic materials are the same in Figures 2a and 2b (a fiberglass reinforced polymer), but they have different stacking sequences. This affects the onset of damage and damage progression. However, in both cases, the damage can be quantified by the metric of Dissipated Energy as shown in Figure 3.

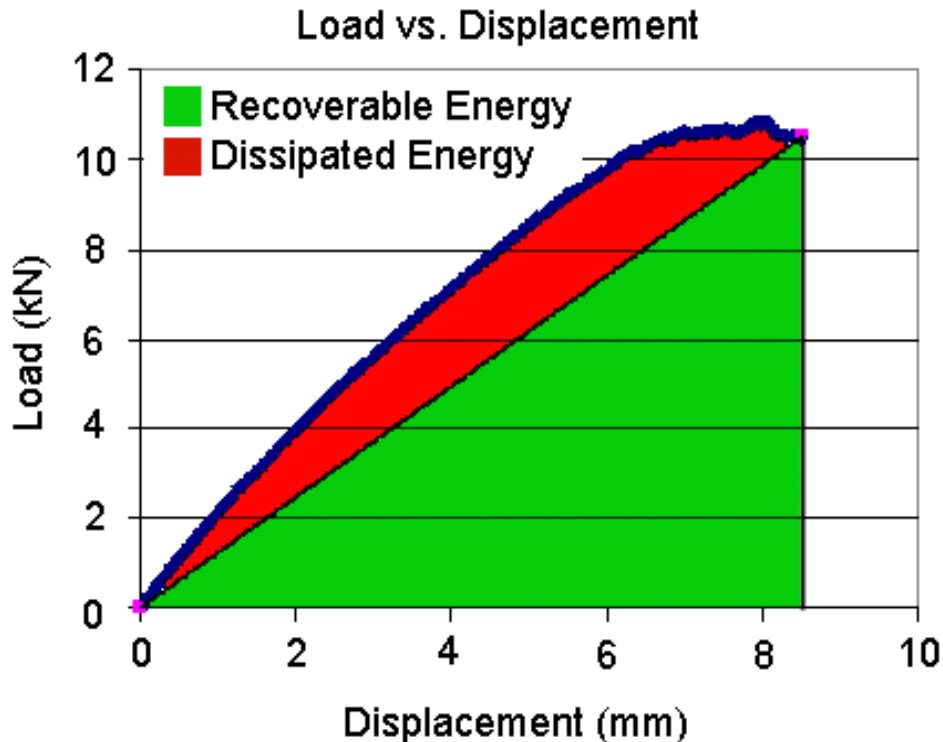


**Figure 3. Dissipate Energy as a Function of Loading (Red is dissipated energy, Green is recoverable energy from loading)**

This curve can be constructed from a property at the material level which is defined as dissipated energy density, the energy dissipated/volume for multi-axial loading. It is analogous to strain energy release rate in conventional fracture mechanics. However, it is a scalar quantity, representing the dissipated energy/volume as a function of strain.

With such a metric, the geometry can be eliminated, and fewer tests are required to complete materials qualification, ala Figure 1.

### **APPROACH**

During this project, we extended some previous work on multi-axial testing to determine the failure of composite materials with true multi-axial loading. The multi-axial testing machine is shown in Figure 4.

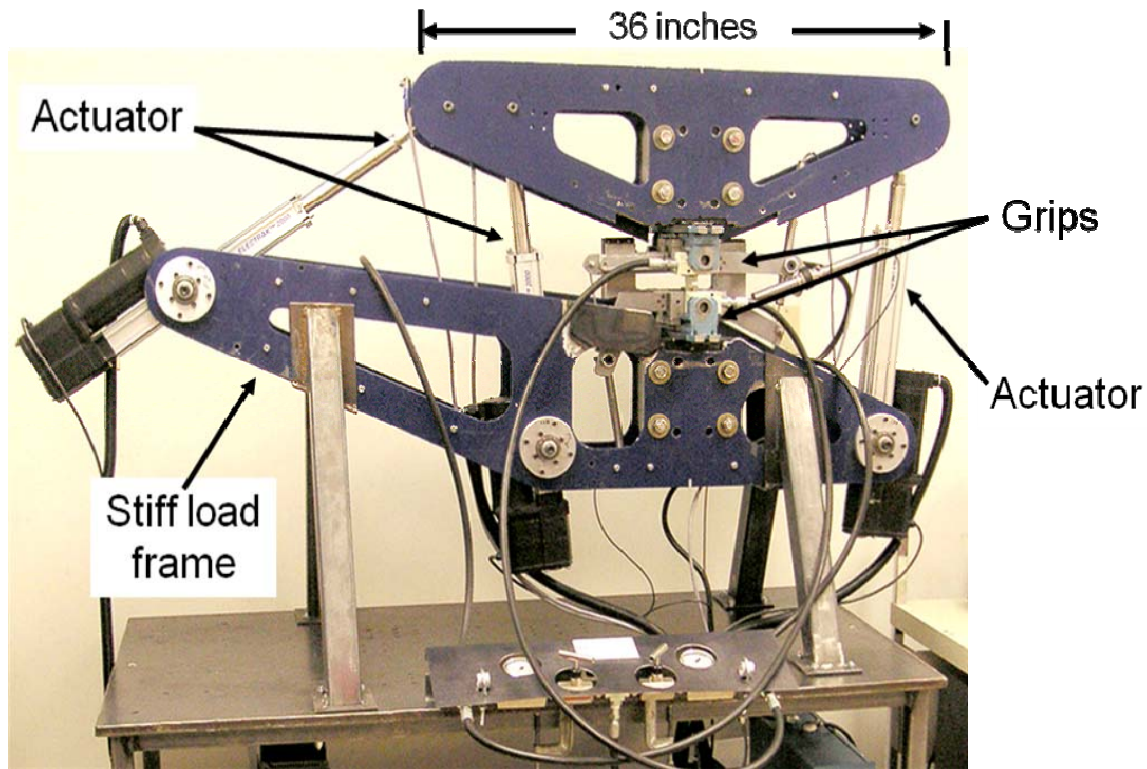


**Figure 4. Montana State University In-Plane Loader**

The testing machining Figure 4 is capable of providing any combination of in-plane displacements, plus a rotation.

The actuator kinematics are shown in Figure 5. The triangles represent closed loop kinematics to obtain any desired displacement. Since the actuators are non-orthogonal, any pure displacement or rotation requires the movement of all actuators.

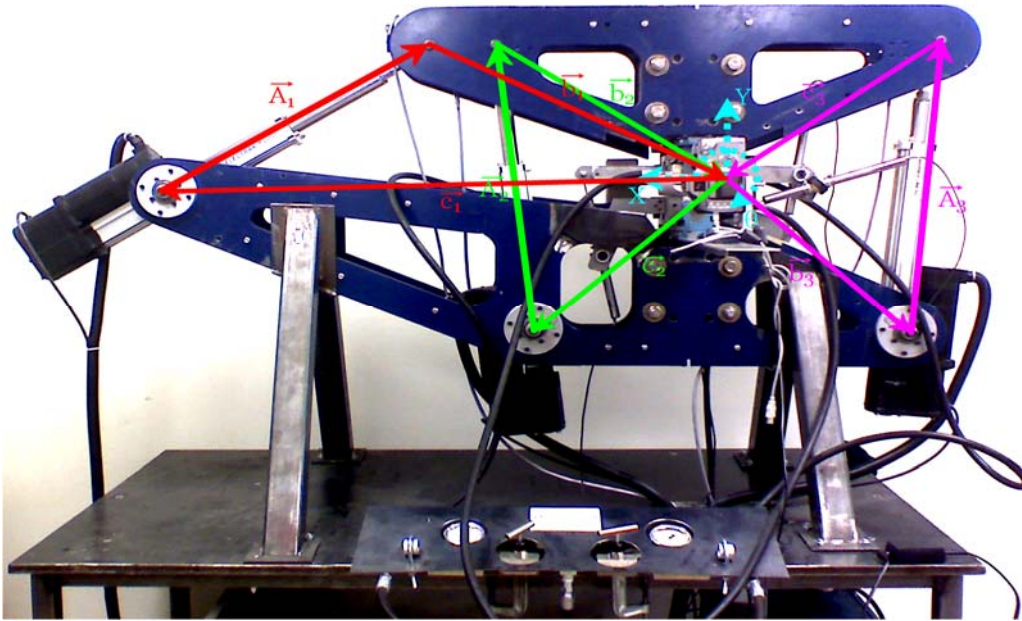


**Figure 5. In-Plane Loader Kinematics for any displacement plus a rotation**

A typical sample configuration is shown in Figure 6. This sample consists of a grip section, plus a gage section. There is a strain concentration in the gage section to promote damage initiation and progression. The interpretation of this geometry requires finite element modeling to resolve strains in material principal axes. The details of this process are provided in Reference [2].

The pure, in-plane displacements in the test section are shown in Figure 7. These consist of an x axis displacement ( $u$ ), a y displacement ( $v$ ), and an independent rotation ( $\omega$ ). Hence any loading combination can be obtained.

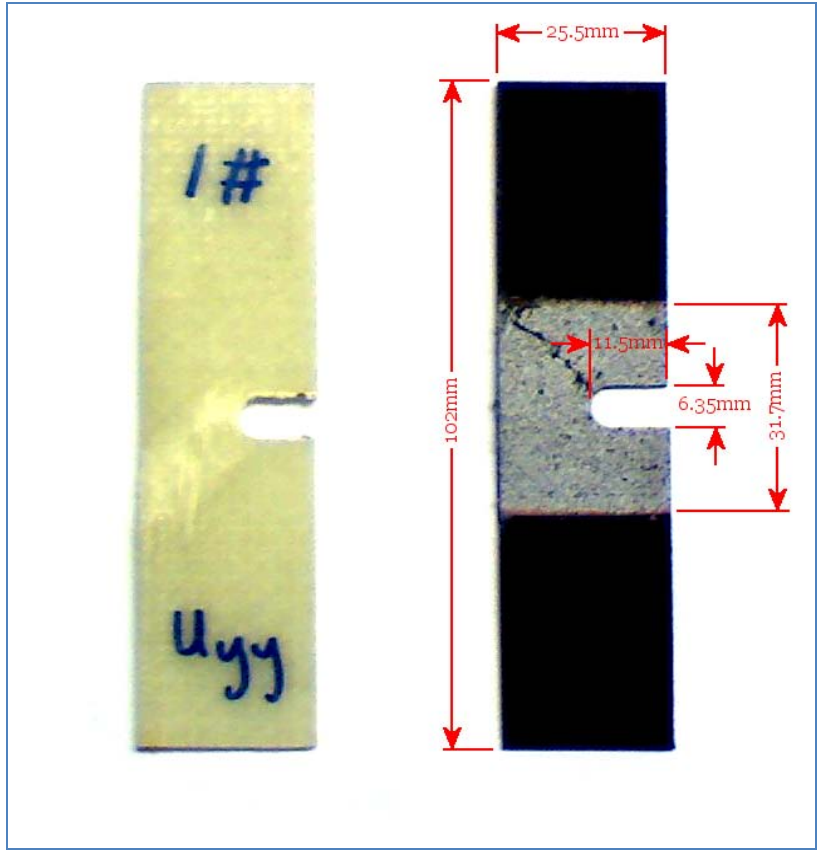


**Figure 6. In-Plane Loader Sample (grip section plus gage section)**

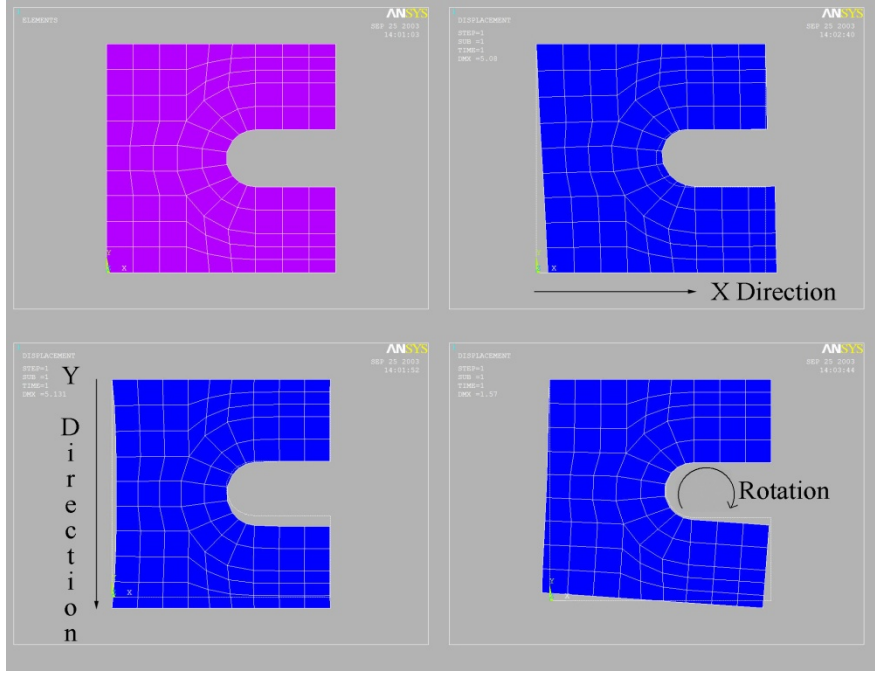


**Figure 7. In-Plane Loader Pure Displacements (u,v) plus a rotation**

A finite element of the sample is shown in Figure 8. Solving the inverse problem of dissipated energy does not require a fine mesh because the analysis utilizes interpolation functions in strain space for the dissipated energy density as described in Reference [2].

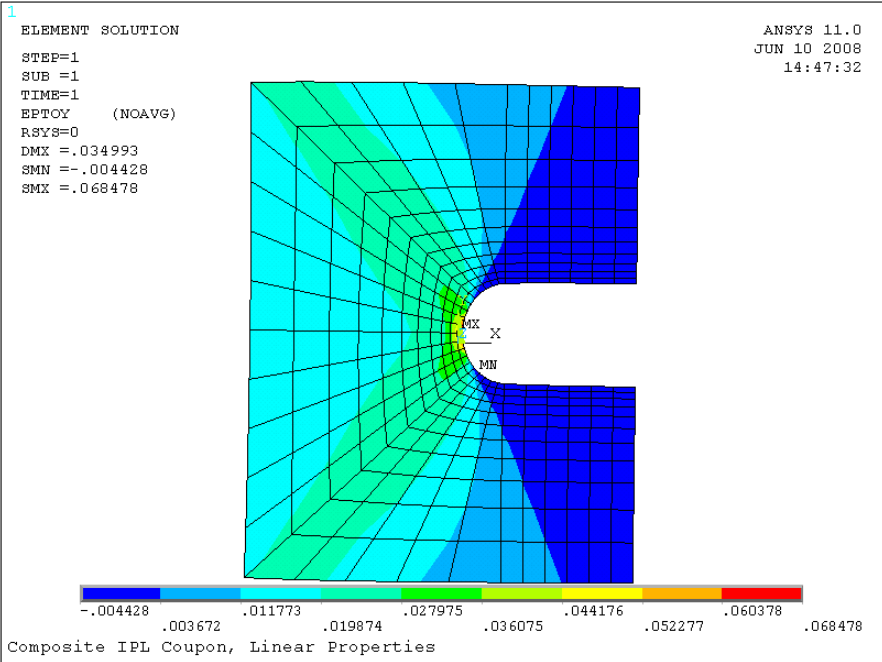


**Figure 8. Finite Element Mesh for Determining Dissipated Energy Density as a Function of Strain [2]**

By solving the inverse problem, a dissipated energy density surface in material principal axes is obtained as shown in Figure 9. Each color represents an isocontour of dissipated energy density in strain space. The axes are material principal strains  $\epsilon_{11}$ ,  $\epsilon_{22}$ , and  $\epsilon_{12}$ . Hence, multi-axial material properties, independent of geometry (unlike Figure 1) are obtained as a materials qualification database.

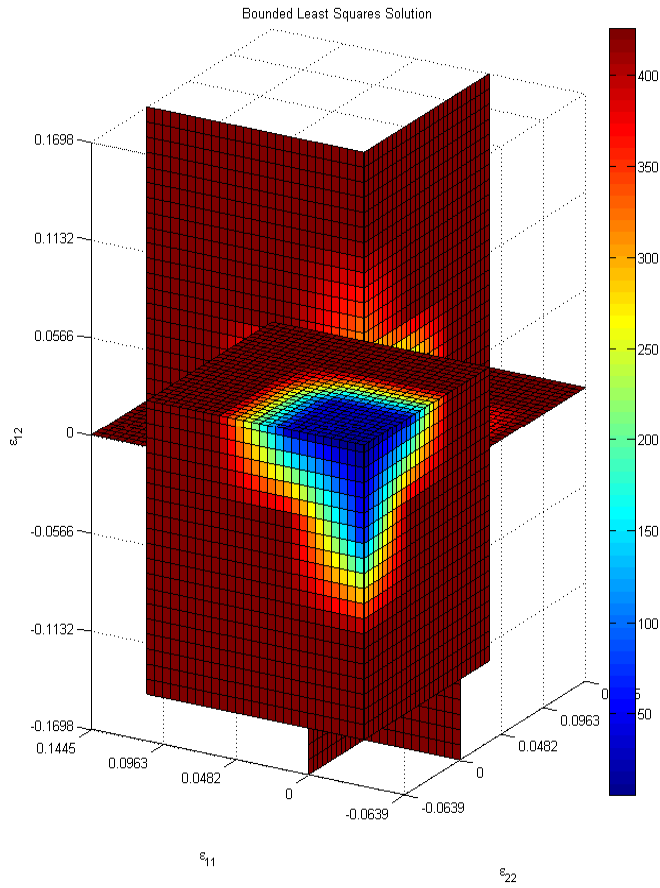


**Figure 9. Isocontours of Dissipated Energy**

Using this testing, a good prediction can be found between the predicted and actual dissipated energy density. The functional relationship leading to Figure 9 is shown in Equation 1.

$$\phi = f(\varepsilon_{11}, \varepsilon_{22}, \varepsilon_{12}) \quad 1)$$

Equation 1 is a scalar quantity in strain space representing the amount of energy dissipated at a given multi-axial strain level. The integral of this quantity throughout the volume of a material/structure is the total energy dissipated during the initiation and progressive damage process and leads to the result at a structural level similar to Figure 3. A typical result is shown in Figure 10.

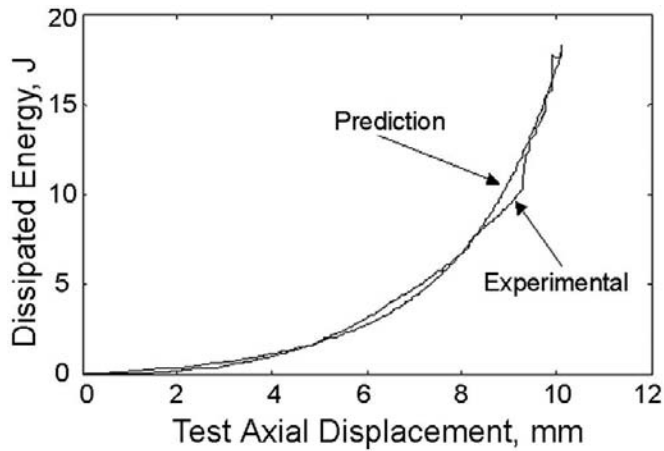


**Figure 10. Predicted vs. Experimental Dissipated Energy for progressive damage**

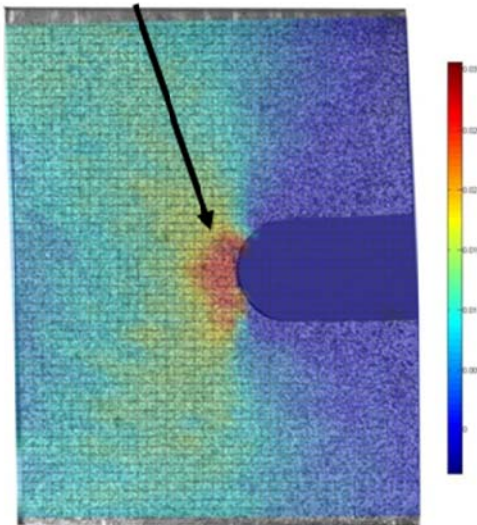
Some comments on Figure 10 are warranted. The prediction was made from dissipated energy density at the material level. The laminate stacking sequence was not part of the experimental database. It is a prediction from a database, not a curve fit to the test. Furthermore, these results are geometry-independent, and can be utilized to obtain the performance at various levels in Figure 1. Consequently, the testing in Figure 1 can be significantly streamlined wherein a small number of tests are needed only for validation, and not as part of the materials qualification database.

There is also a threshold in strain space where no energy is dissipated. This is the elastic region of the material. This has utility for design limit load analysis of composite structures. If no energy has been dissipated at design limit load, the static strength of the design is adequate.

## **PROGRESSIVE DAMAGE RESPONSE**

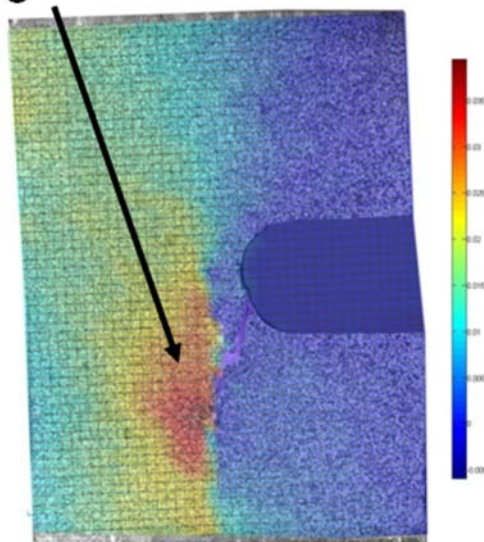
As described in Reference [2], a finite element model was used to analyze the test samples. A more desirable method is to actually measure the progressive damage. A Digital Image Correlation (DIC) process was developed with very low cost hardware for this project. Using a low cost camera, DIC software was developed to monitor the progressive damage on the test samples. Typical results are shown in Figure 11. In Figure 11, the red is high strain, and the blue is lower strain. As damage progresses, the material locally softens, and the higher strain moves along with that damage as shown in Figure 11b. This led to the development of a strain softening model in multi-axial strain space as shown in Figure 12.

## Damage Onset



a) Onset of damage (red is high strain)

## Damage Progression



b) Progressive damage after onset  
**Figure 11. Progressive Damage in Test Sample**

In this project, the feasibility of using Digital Image Correlation (DIC) for progressive damage monitoring and modeling in composite materials was demonstrated as described in Reference [3], but to link the progressive damage response to the material response without any finite element analysis will require more work. The DIC was used primarily as a validation tool, but not as a data analysis method in this task.

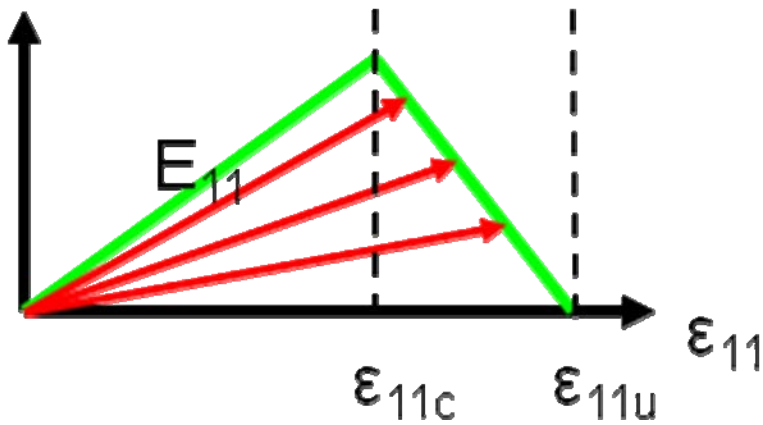


**Figure 12. Bi-linear strain softening model**

In material principal axes,  $\epsilon_{11c}$  is the critical point where strain softening begins, and represents the elastic limit of the material. A similar curve is associated with the other strains.

Predicted versus experimental curves are shown in Figure13 and 14. These nonlinear load versus displacement curves were predicted with the optimized, bi-linear constitutive models in strain space [2].

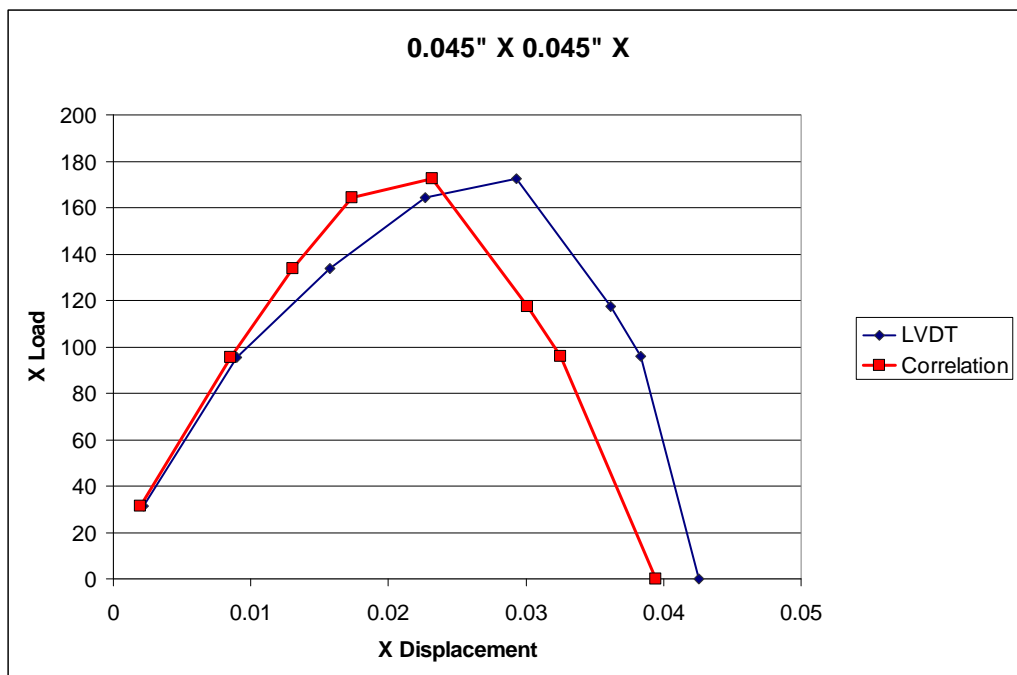


**Figure 13. Load vs. Displacement of a Test Sample, Experimental vs. Correlation (predicted)**

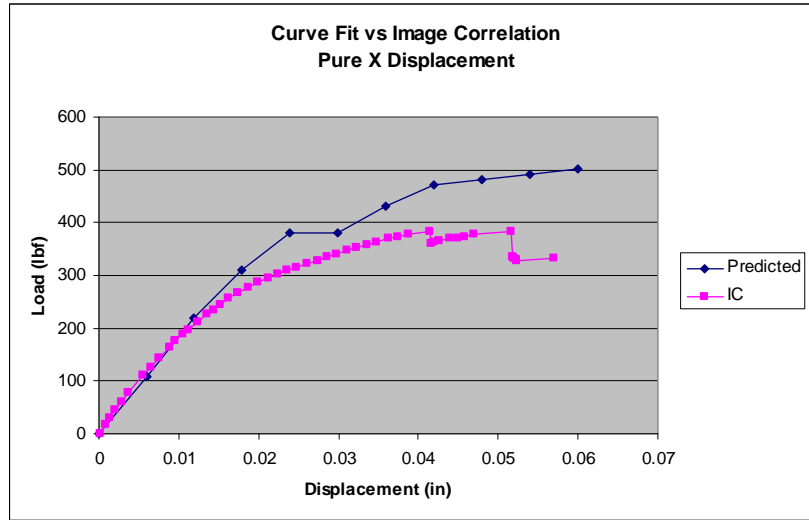


**Figure 14. Load vs. Displacement of a Test Sample, pure x displacement, Experimental vs. Predicted**

The results are not perfect, but show great promise for modeling the nonlinear response of structures as a consequence of nonlinear constitutive behavior.

## **APPLICATIONS**

During the course of this research, several applications were identified and work was done toward that end.

The first application is to perform multi-axial testing on a composite “patch” material for composite structural repair. The basic idea is to characterize a laminate through a very large, multi-axial strain space. If the material is within the strain space with no catastrophic failure in the structure as verified through analysis, the patch should be adequate. This means that the patch is essentially pre-qualified for a variety of repair situations.

The testing and procedures developed in this project were utilized in a funded research project with Goodrich Aerospace as the lead. It is entitled “CMC Airfoil Capability Enhancements for Military Aerospace Gas Turbine Engine Systems”; REQUEST FOR PROPOSAL NO. V80328, Dr. Ruth L. Sikorski, AFRL/RZTS, Wright-Patterson. The methodology was applied to ceramic matrix composites for multi-axial testing and characterization. The end date of this contract is March 31, 2010 and details of the testing will be provided then. However, preliminary analysis indicates that under certain modes such as pure tension, these materials have little capability for progressive damage; damage initiation is coincident with failure. Under other multi-axial loadings such as tension plus shear, the materials show some capability for post damage load carrying capabilities.

Throughout the course of this work, discussions were initiated with GE aircraft engines for fan containment cases. In some sense, this is the perfect application of the philosophies and technologies developed in this research. A quantifiable kinetic energy must be dissipated and contained to preclude a failed aerofan blade from penetrating the outer surface of an engine. If the dissipated energy capability of the structure as analyzed with dissipated energy density from tests exceeds that which is to be contained, a successful design can be obtained.

The potential application for characterizing “self-healing” materials was developed. In this scenario, the undamaged material can be characterized with multi-axial testing. Then, the “healed” material can be characterized and directly compared to an undamaged or baseline material. The differences can be quantified with respect to the onset of damage, dissipated energy density, and constitutive response.

## **FUTURE WORK**

The results from this project have shown great promise to streamline the characterization of materials for primary DOD structure as currently practiced via Figure 1.

Future work will include a proposal to Boeing Commercial Aircraft Group in Seattle for a universal repair patch. This patch will be of two configurations, quasi-isotropic and orthotropic with some capability to optimize directional properties. It is expected that this will be funded with Boeing monies, but AFOSR or other DOD sources could augment this work for military applications.

There is an ongoing emphasis for multi-functional materials for a variety of purposes within AFOSR. This work could be instrumental to characterize the combined multi-functional aspects of a material, and its influence on mechanical properties under multi-axial loading. If a multi-functional material has compromised mechanical properties compared to established structural materials, it is important to understand these compromises and determine if they are acceptable. The multi-axial testing capability is necessary to answer these questions.

There has been much discussion and research on “self-healing” materials, and it will be necessary to characterize these materials to determine the limitations and to quantify the potential for applications to primary structure.

Two technologies were developed for this work. The first is a multi-axial testing machine. Several important technologies have been brought together for success. This includes machine design, data acquisition and control, and testing. A new multi-axial testing machine, capable of testing in three dimensions will help to extend this work. Also, larger servo-hydraulic actuators will provide a higher loading capability, and a fatigue loading capability.

The second technology has been the development of a Digital Image Correlation (DIC) capability. Through this effort, Montana State University has developed an understanding and investment in DIC for multi-axial testing and progressive damage analysis. The PI for Task B wrote an NSF Major Research Instrumentation (MRI) which included the purchase of an ARAMIS 3-D optical measurement system [4]. One of the successful aspects of this proposal was the fact that we are technically vested in DIC through this research program. This is distinctly different than researchers who simply purchase equipment and apply it. We fully expect to be able to extend the technology of DIC, as well as utilize the results. The ARAMIS system will be augmented and advanced with our knowledge of DIC and progressive damage modeling.

## REFERENCES

1. <http://www.cmh17.org/>
2. <http://etd.lib.montana.edu/etd/2008/schmitt/SchmittJ1208.pdf>
3. <http://etd.lib.montana.edu/etd/2009/parker/ParkerJ0509.pdf>
4. <http://www.trilion.com/Products/aramis.html>

# **TASK C. CHARACTERIZATION OF ADHESIVES AND DAMAGE GROWTH IN JOINTS**

**Aaron Sears and Robert Badaliane**

## **Summary**

Adhesive bonding is an attractive and highly efficient method in joining composite structural components and repair of new, damaged, or aged airframe structures. Certainly, there has been much research in bonded joints, so some elaboration regarding the uniqueness of the current project is warranted. The current project is unique in using dissipative energy as the metric to determine the damage threshold in bonded joints. Furthermore, methods were developed for determining damage thresholds for a large domain of strain space.

A test geometry, the notched Tee joint, was developed for studying joints with a multi-axial testing machine. The strain states and damage initiation zones in the adhesive were directly related to the load path. A wide strain space for adhesive characterization is available in this geometry.

Additionally, a test geometry was found which develops a relatively wide strain space for characterization with a uni-axial testing machine. A damage progression model and method for characterizing the nonlinear response of an adhesive joint was developed for use with either geometry. This method optimizes the material properties of the adhesive by matching finite element results to test results for multiple cases in a single process. The nonlinear material properties are functions of the strain state as defined by the principle strains. Using this process the nonlinear material response of the adhesive FM300 was found for tests on aluminum/FM300 and carbon-epoxy/FM300 joints.

## **INTRODUCTION**

There are several factors that dominate the design and consequently the performance of adhesively bonded joints. These factors can be grouped into materials (adhesives and adherands), processing that includes surface preparation, and geometric configurations (e.g. lap joints with continuous ply drop offs, and step lap joints with discontinuous ply drop offs). Another important issue is the interface characteristics, which plays a highly dominant role in the integrity and performance of bonded joints.

In adhesives and polymer based composite materials, damage threshold is the onset of appearance and accumulation of micro cracks that can be quantified by dissipated energy density as the metric. However, the independent characterization of the interface as a unique entity is a very difficult if not undoable task. It is for this reason that the whole joint is tested rather than relying on neat adhesive tests to characterize the adhesive. From a unified viewpoint, the quantified damage threshold (in the constituents separately, the interface and the joint collectively) can be used as a parameter in the design and integrity assessment of bonded joints. By testing a joint in multiple load paths, the joint can then be characterized over a large strain space domain. Ideally the multiple load paths are achieved by a multi-axial testing machine.

### **Characterization**

Characterization of the joint necessarily includes characterization of the adherend, adhesive and interface. The bulk of the joint is the adherend. As such, it is argued that the adherend can be characterized in separate tests as any changes due to the interface will be very small and potentially insignificant. Because we cannot effectively characterize the interface region separately, it becomes necessary to include the interface into the adhesive characterization. Thus the joint characterization effectively becomes the material characterization of the adhesive and interface. For the purpose of characterization of damage in the adhesive, it is also necessary to insure that the damage in the joint is not in the adherend, but instead occurs in the adhesive or interface.

### **Goals**

The goals of this research program were: (1) to develop test methodologies to better define the parameters which determine damage thresholds; (2) to improve the performance of joints in terms of damage thresholds; by considering gradient adhesives as well as adhesives fortified by nanoparticles; and, (3) ultimately, to establish a design paradigm for joint structures that would be based on rationally defined and measured damage thresholds. The latter two goals require the first goal to be met, which makes this goal the most important.

## METHODOLOGY

### Dissipative energy

The dissipative energy of a composite structure is the energy that is lost due to internal damage in that structure which is irreversible and not plastic in nature. Thus, having no permanent strain, on unloading the structure returns to its original undeformed state. The structure will then load up on the secant modulus. Graphically, the dissipative energy is the shaded (orange) region in Figure 1. The dissipative energy density is thus the energy dissipated at a point in the structure.

In the present study, the dissipated energy density function is used as a metric to define damage. The dissipated energy density function,  $d^p$ , is postulated to be a property of the material. The volume integral of the function returns the total dissipated energy,  $D^p$ , in the structure. The value of  $d^p$  at a point is a measure of the load induced internal damage. The internal damage is a collective damage and is not separated into damage types or failure mechanisms. As alluded to earlier, the value of  $d^p$  is related to the stiffness change of the material in the structure. Failure micro-mechanisms, and their complex interactions, are inherently captured in the  $d^p$  as a function of strain,  $\epsilon$ . Thus for a load path and resulting strain vector at a material point,  $d^p$  has a different value. Hence, the challenge is to obtain values of  $d^p$  over a large strain domain (space). Once  $d^p$  obtained the material response at any strain can be determined as a function of the linear properties and an interpolation of the stiffness changes due to the damage and determined by  $d^p(\epsilon)$ . For a more in-depth discussion and theoretical development of dissipated energy the reader is pointed to NRL/FR/683- -92-9369 [1].

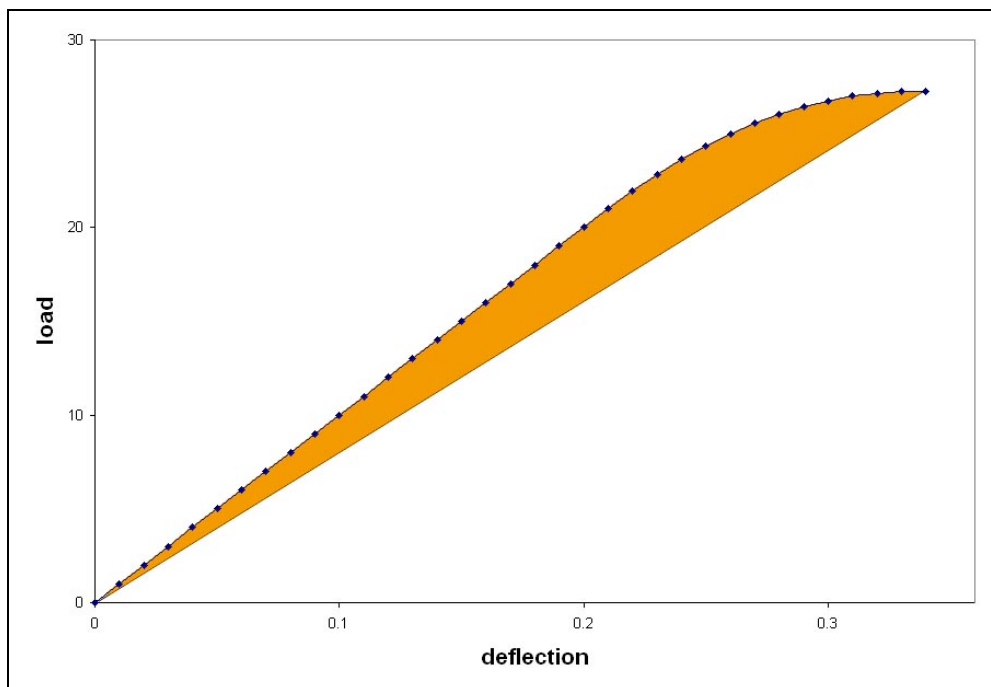


**Figure 1. Example of an idealized test response of a structure with the strain energy dissipation shown as the orange region.**

## **Constitutive characterization through optimization methods**

The current constitutive characterization method is a derivative of the inverse method. In the present study, changes must be made to accommodate the resources available and the nature of adhesive responses and the testing of joints. Like the inverse method, this method attempts to minimize the error between FE predictions and test data (objective function) by changing the material response (design variables).

In the NRL study, the design variables were the strain energy dissipation values in the material along strain vectors (directions). These studies were based on linear FE predictions for composite materials demonstrating a linear behavior. The present study attempts to characterize adhesive material properties along strain vectors. However, adhesives exhibit more nonlinear behavior. Thus, the present study must include the nonlinear response of the adhesive. Thus, the design variables of the optimization change to those which define the nonlinear response.

The NRL study used more data sets than it had design variables in order to have an overdetermined system to optimize. The current method works best with the same stipulation although less robust solutions (material characterizations) can be found with fewer data sets.

## **Multi-Axial Loading & the MSU-IPL**

To avoid guesswork or extrapolation during design, a damage envelope encompassing a full spectrum of strain states developed from extensive testing is necessary. Thus, the test matrix requires either numerous joints, with different maximum stress/strain states, or a single joint tested under many load paths. The MSU-IPL offers the ability to test a sample under any combination of in-plane displacements (vertical, lateral or rotational directions). Thus, with a suitable joint geometry, it is possible to obtain the damage behavior over a full spectrum of strain states.

The In-plane loader (IPL) offers the unique ability to test a sample under a variety of loads and consequently place the sample under a number of strain states. It is capable of putting a sample under any combination of (in-plane) axial, lateral, and rotational deformations. It achieves these through three electric linear actuators placed in a specific geometry to avoid binding. A picture of the IPL and its loading paths is shown in Figure 2. Grip movement is controlled and defined by three LVDTs parallel to the actuators. Pictures of three different test geometries are shown in Figure 3, including two samples tested to failure under rotation. The actuators of the IPL are limited to loads of 2000 lbs each. Thus the maximum load capacity of the IPL in tension is ~4000 lbs and laterally ~ 2000 lbs. Out of plane deformations are limited by guides (cannot be seen in Figure IP1).

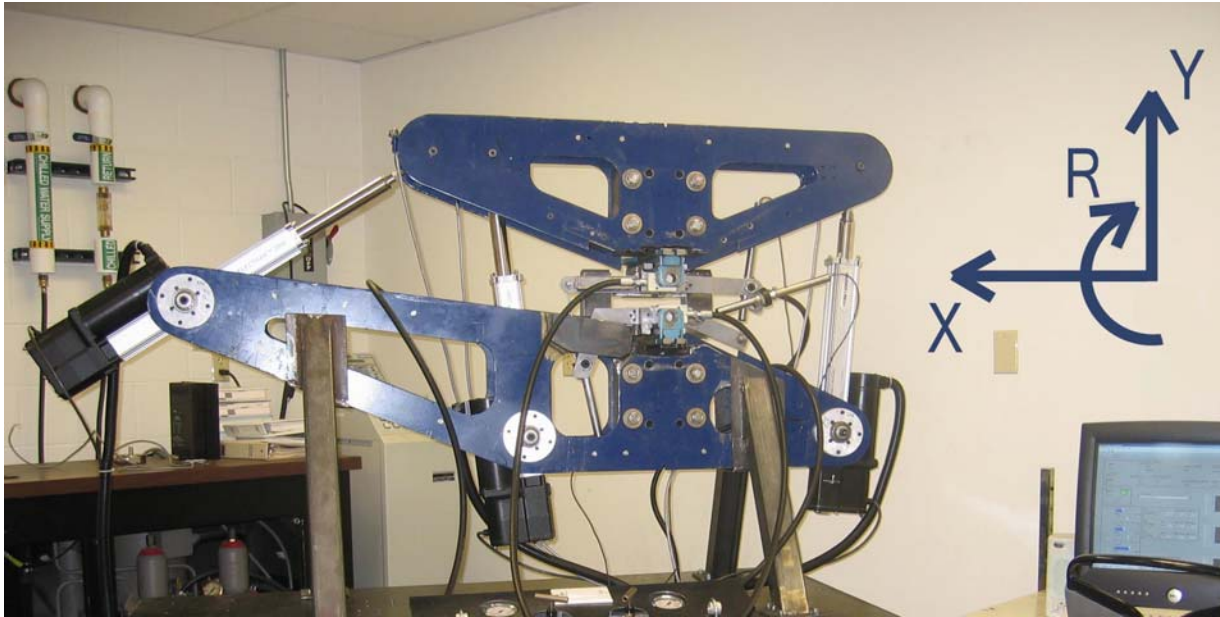


**Figure 2. Picture of the MSU-IPL**



**Figure 3. Series of photographs showing the loading history of a composite specimen tested in the MSU-IPL in a rotational load path (speckled paint applied for image analysis)**

Since the IPL is an original, complex test machine, it is necessary to show that accurate data can be acquired from a test. Specifically, it is necessary to show that the IPL can reproduce a simple tension test commonly performed by standard uni-axial testing machines. Thus, a tension test of an isotropic material with a constant cross section was chosen to validate the IPL and image correlation test and data acquisition procedures. Aluminum was chosen for its well known response and similar stiffness to the tests to be performed in this study. Here, the linear elastic modulus of the material is calculated by linear regression to be 9.95 Msi. This value is within a reasonable region for 6061 aluminum. The LVDT response was found to be 18% lower than the image correlation data which places it well below typical accepted values for aluminum (8.15 Msi). The LVDT response was also found to be consistently dropping in the linear range. Since the strains were not high enough to plausibly cause plasticity, this is most likely due to slipping of the grips and or bending of the grip mechanism.

## **Image Correlation Analysis**

Image correlation offers the best option for accurate data acquisition for the IPL because it directly measures the displacements of the sample. The LVDT data indirectly measures the grip displacements and errors may propagate due to grip or fixture bending, sample slipping or other effects. To obtain full displacement fields for a test the sample is painted a speckled black and white pattern with common spray paints. A typical notched composite test specimen is shown in Figure 3.

The image analysis software correlates two images by analyzing discrete points. A point is defined by its circular neighborhood of pixels. The number of points used to correlate two images, and the neighborhood size and the search zone for the second image are among the parameters that can be controlled by the user. The neighborhood of the points translated from pixel grayscale to a mathematical, binomial function. This is done since the same location on a sample will not have the exact same pixel pattern between two images because they will be offset by some unknown fraction of a pixel which changes the pixel pattern. This problem occurs because the continuous natural image is discretized into pixels with a grayscale number to store it digitally. However, by fitting a function to a neighborhood of pixels, a local continuous 'image' is recoverable. This local continuous image will remain constant, or at least close enough, to correlate two locations from two different images. From there it is easy enough to determine point to point displacement and thereby develop a full sample displacement field from a full set of points. This is the reason behind the speckled paint pattern. The randomness of the speckled pattern means that any location on the sample can be taken as a sample point due to its unique neighborhood image pattern. Another benefit of this method is that sub-pixel accuracy is possible. The image correlation analyses used in this study was developed in concert with the Task B [2].

## **INITIAL JOINT STUDIES**

### **Joint Design & Gradient Adhesive Joints**

From a combined materials and geometric perspective, the challenge lies in matching the structural impedance, i.e. the stiffness and constitutive properties of the constituents and joint geometry, and reducing stress singularities. In general, adhesives tend to be much more in-plane compliant than the adherand materials; however, this disparity can potentially be overcome by introduction of stiff nanoparticles such as nanocarbon platelets and nanocarbon tubes. The introduction of nanoparticles would enable us to functionally tailor the adhesive stiffness for mitigating the stress singularities at edge discontinuities and laminate ply drop-offs. A more simple method to achieve gradient adhesives is to use adhesives of different stiffnesses (e.g. FM300 & FM400). This is demonstrated in the following section through a double lap shear joint.

The possibility of matching mechanical impedance to minimize stress discontinuities in adhesive joints holds promise to advance the understanding and application of adhesive joints in

composite materials and structures. Furthermore, the ability to apply and analyze multi-directional loading on a bonded joint is attractive to obtain a database which encompasses the expected loading for the joint, rather than the traditional simple, unidirectional tests.

### Double Lap Shear Joint & Gradient Adhesives

Double lap shear (DLS) joints are commonly tested geometries for joints due to their symmetry and similarity to joints in structures. After sharing knowledge on joints, Boeing St. Louis and MSU ran concurrent analyses on simple and hybrid double lap shear joints. The premise was to compare the Hartsmith closed form solution [3] to finite element solutions and to evaluate the performance of hybrid adhesive joints. A hybrid adhesive joint is a stepped functionally gradient joint where the stiffer adhesive is placed in the center. A generic hybrid joint is shown in Figure 4.

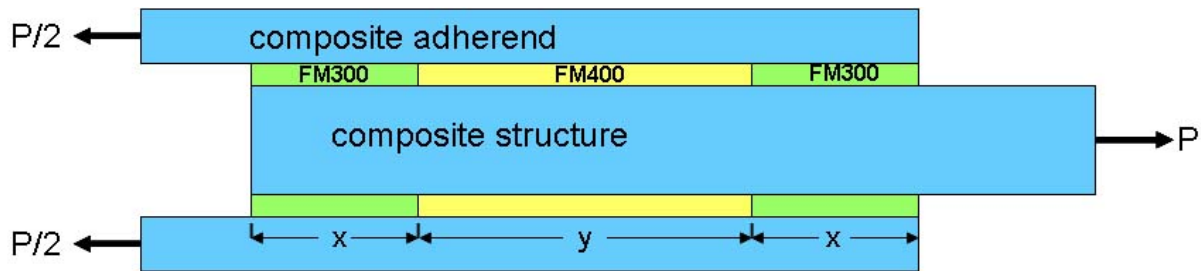


**Figure 4. Sketch of the half symmetry geometry of a hybrid double lap shear joint**

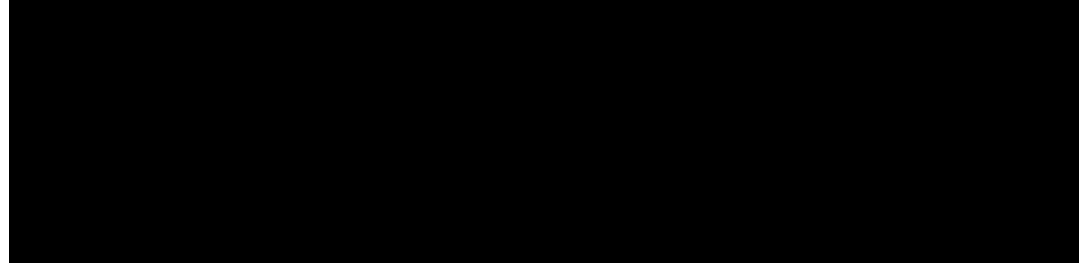
The comparison of simple DLS joint solutions are shown in Figures 5 and 6. The linear Hartsmith and FE analyses of the simple DLS joints (single adhesive) provide shear stresses in the adhesive layers which are in agreement with each other. For both analyses the shear stresses in the adhesive in Figure 5 are symmetric with maximum values at the edges. For longer DLS joints, the shear stresses can be seen to flatten out in the central region. Thus, most of the load in a DLS joint is transferred at the edges. The FE analysis also provides peel stresses which are more complicated in nature and neither symmetric nor asymmetric. However, the maximum peel stress occurs at the leading edge of the joint. The adhesive is assumed to be linear elastic in nature and thus the stresses directly correlate to strain. For the DLS joint in tension, the location of damage onset is most likely to occur at the leading edge with peel and shear strains roughly equal.

The analysis demonstrates the advantage of hybrid joints is the ability to carry higher loads across the whole of the joint. As observed earlier, most of the load in a DLS joint is carried at the edges while little is carried in the center which can be the bulk of the joint length. Thus, the idea of the hybrid joint is to have a higher stiffness adhesive in the center which can then carry a higher load, thereby reducing the stress concentration at the edges. The stresses in a hybrid FM300/FM400 DLS joint are shown in Figure 6.

An optimization analyses to maximize the load carrying capacity of this joint by changing amount of the two adhesives was performed by Boeing analysts using the Hartsmith solution.

For the elastic plastic solution the adhesive was assumed to be perfectly plastic. The results are shown in Table 1. The optimized hybrid joint does show a 29% advantage in elastic loading and a 19% advantage in elastic-plastic loading over an all FM300 joint for room temperature dry properties.

**Table 1. Results from Hartsmith analyses of a DLS joint (analyses performed by Boeing)**



\*hybrid cases have the FM300 split evenly around the FM400 (see Figure HDL)

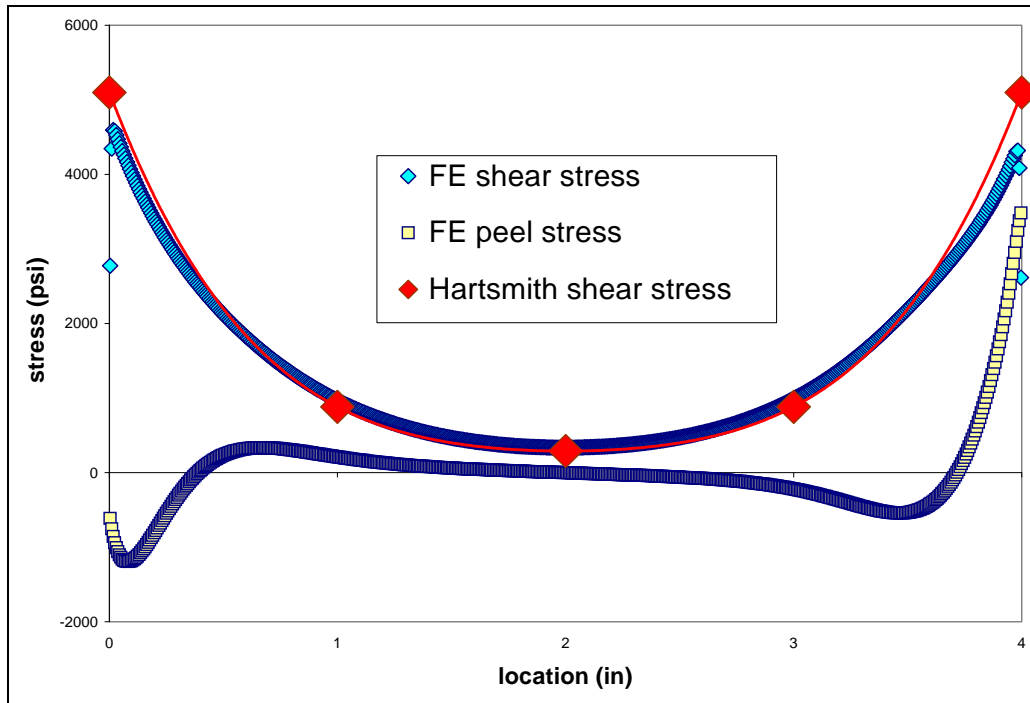


**Figure 5. Stresses in a single adhesive DLS joint**

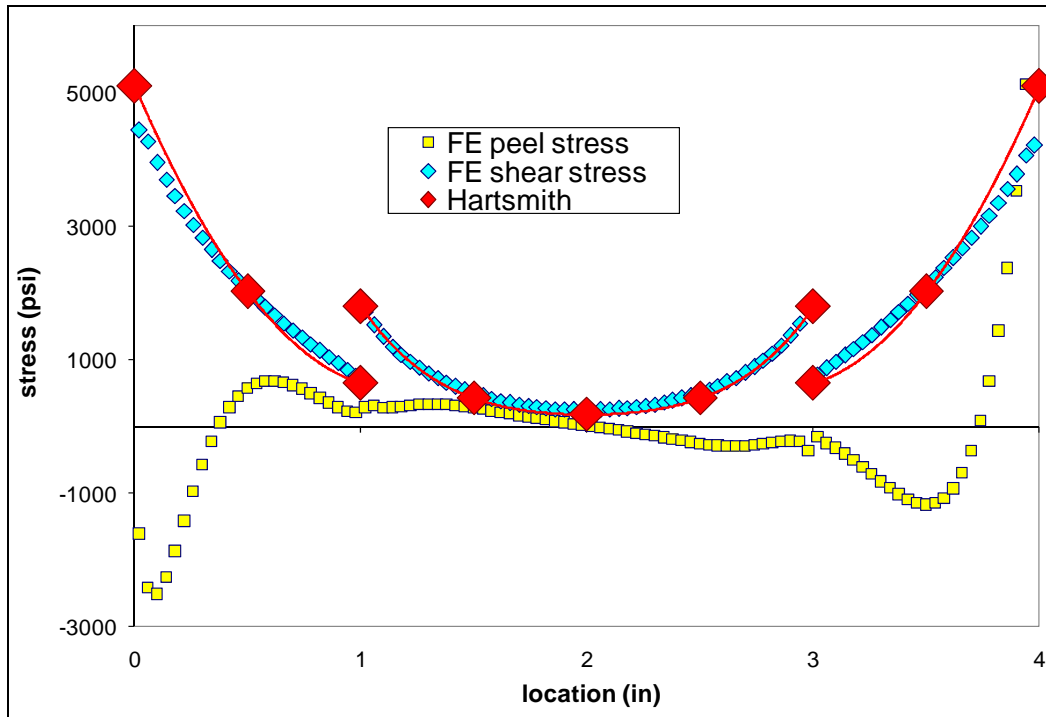


**Figure 6. Stresses in a hybrid DLS joint**

### Edge Geometry Studies

One of the primary goals of the study is to determine damage onset for a wide range of strain vectors. FE analysis of DLS joints showed high stress concentrations at the leading free edge. Thus, this is the most likely site for damage to initiate (see next section for experimental confirmation of this initial damage site). The strain vectors at these stress concentrations tend to have a mixture of peel (tension) and shear strains. A number of edge geometries were studied to understand their impact on the damage site and strain space. Some of the geometries studied were tapered adherends, rounded edge adherends, and edge adhesive geometries (such as radial 'blobs', flat ends, and rectangular and triangular extensions). Examples of some of those studies are shown in Figure 7 which plots the peel and shear strains for two cases. The net conclusion for the study was that no matter the geometry, the potential damage site will have a combination of peel and shear strain. Secondly, this potential damage site is heavily influenced by the edge conditions. Lastly, those influential edge conditions are difficult to control during sample preparation, and thus are not a good method by which to control the damage site.

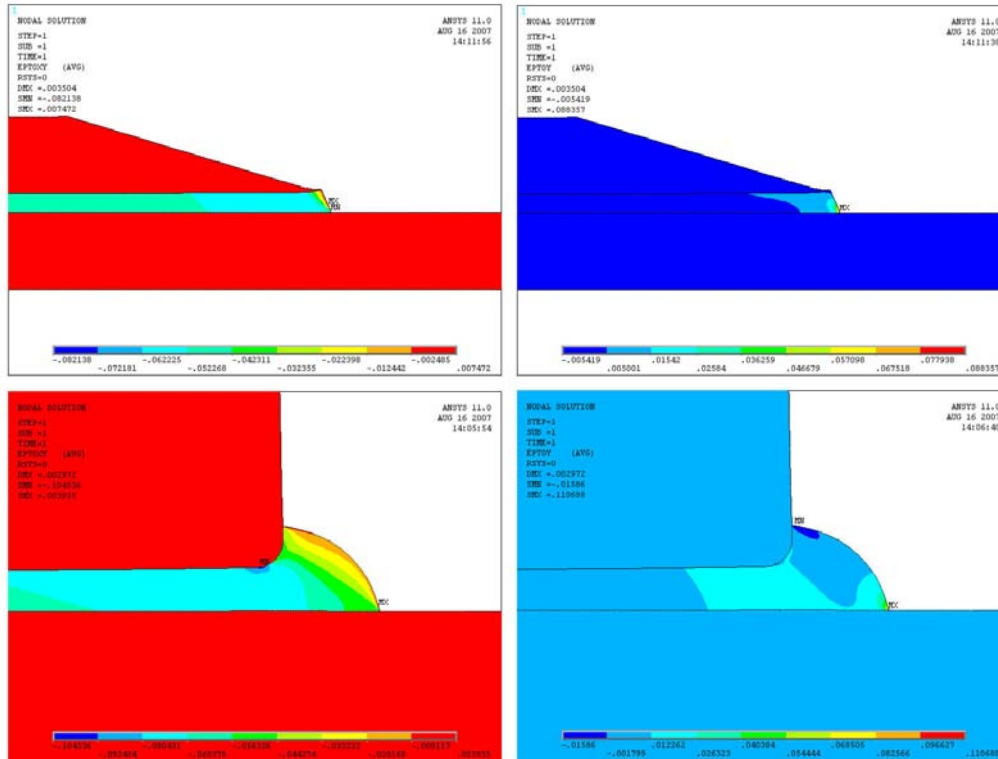


**Figure 7. Representative results from edge condition studies of DLS joints**

### Joint Geometry Selection

To properly utilize the MSU-IPL a single sample geometry is put under various load paths to generate a wide range of strain spaces at which damage occurs. Thus, one of the first steps of the project was to determine a suitable joint geometry. A number of typical, common joints were considered in this program. In particular the double lap shear (DLS) joint was analyzed by FE (above) as well as tested in the IPL. In Figure 8, a DLS joint is shown during a test in the MSU-IPL. The case shown, a rotational load path, exemplifies the problems associated with DLS joints for use with the MSU-IPL. First, damage initiation occurs at the free edge, which according to FE analyses will result in tension-shear strain states no matter the load path. Second, the stiff joint will tend to slip in the rotational load path.

However, these common joints do not take advantage of the multi-axial load capabilities of the MSU-IPL testing machine. For these joints, the bond-line, or more precisely the bond-plane is parallel to the loading plane of the machine. Thus, no matter the load path, the joint will primarily be in a shear dominated regime. In contrast, the tension and compression regimes are controlled by secondary effects of the load path such as free edge effects and out of plane bending. This means that changing load paths doesn't have a direct effect on the strains in the joint.

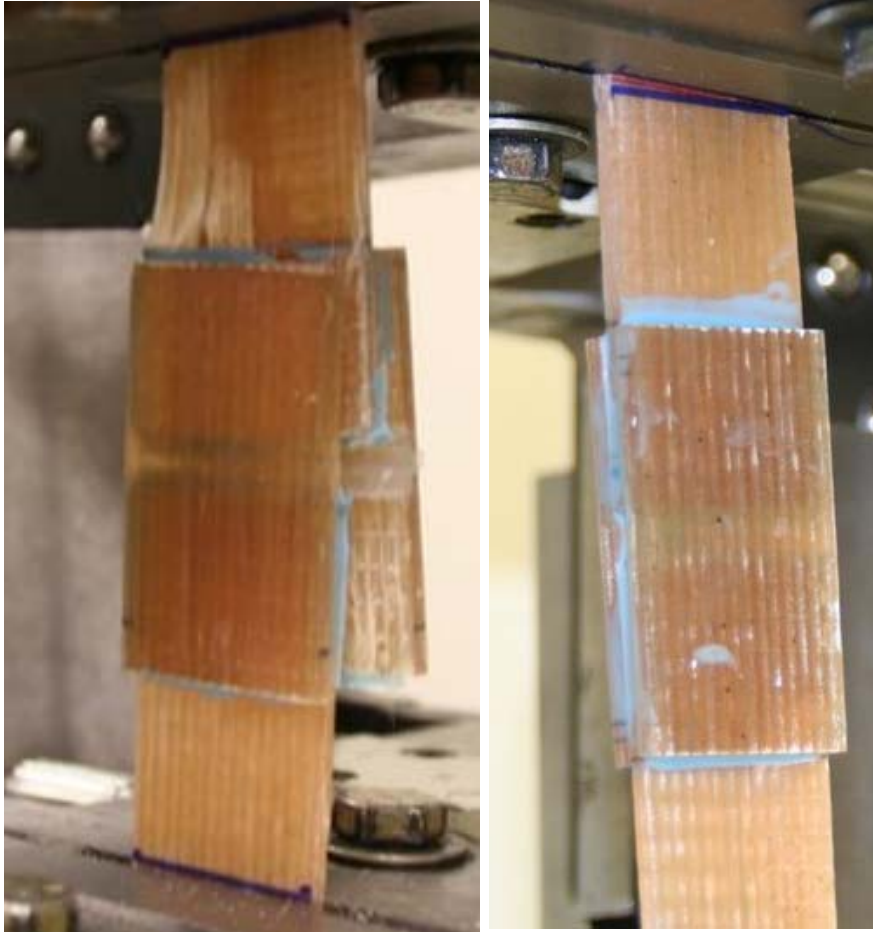


**Figure 8. DLS joint tested in the IPL under the pure rotation load path (left). showing failure, (right) showing grip slipping**

Thus, new joint geometries were investigated which are able to take advantage of the MSU-IPL loading paths. In the previous section, it was stated that the having the bond-line parallel to the load path (and gripping planes) of the IPL restricted the potential strain states in the adhesive. By shifting this argument, placing the bond-line perpendicular to the load paths of the IPL should enable a wider available strain space in the adhesive. In a simple thought experiment, by applying a vertical (tension) displacement by the IPL to this basic geometry should cause peel strains in the adhesive. Similarly simple vertical compressive movement causes compressive strains in the adhesive. Lateral displacements should cause shear strains while rotational paths will cause tension/compression gradients. These simple arguments were later verified by analyses with Tee-joints (see following sections).

Butt joints are the most obvious choice to produce an adhesive layer normal to the grips. A butt joint is simply 2 strips of adherend bonded together at their ends. Unfortunately, the adhesive area of the butt joint is also the adherend area which produces several problems. First, the area of the bond is the same as the cross sectional area of the adherend. This results either in a very limited bond area or very thick adherends. Small bond areas will most likely limit the damage growth potential of the joint, while large adherends will cause very stiff joints which may require

custom grips (or major alterations to the IPL). Also, butt joints are poor geometries for composite material adherends due the direction of the layers. If the adhesive is parallel to the layers, then the composite will most likely fail first due to its weak through-thickness strength. Placing the adhesive normal to the fibers creates an uncommon joint and the joint will not be studying the correct interface characteristics. By adding a crosspiece to the strip, thereby making a T-shape, we can potentially solve these problems.

To summarize, the joints considered in this study were double lap shear, butt, Tee and mixed mode bending style joints that include end notch flexure and dual cantilever beams.

## TEE JOINTS

Tee joints (which make a plus or cruciform shape) also place the adhesive normal to the loading plane, as shown in Figure 9. Tee joints solve the problems found in the butt joint by allowing a wider adhesive zone while retaining a thinner grip section. Another advantage is that the load path wants to follow a straight path through the center of the joint which cases a load gradient across the bond area and is concentrated in the center. This concentration helps to produce damage in a controllable location. Also, because the adhesive in the flange areas is not loaded significantly, this ‘extra’ adhesive does not give the joint more load carrying capacity than the testing machine can apply. However, as the central adhesive area is damaged, the load path will expand to engage more of the adhesive. This loading pattern results in a slower damage growth profile to the test.

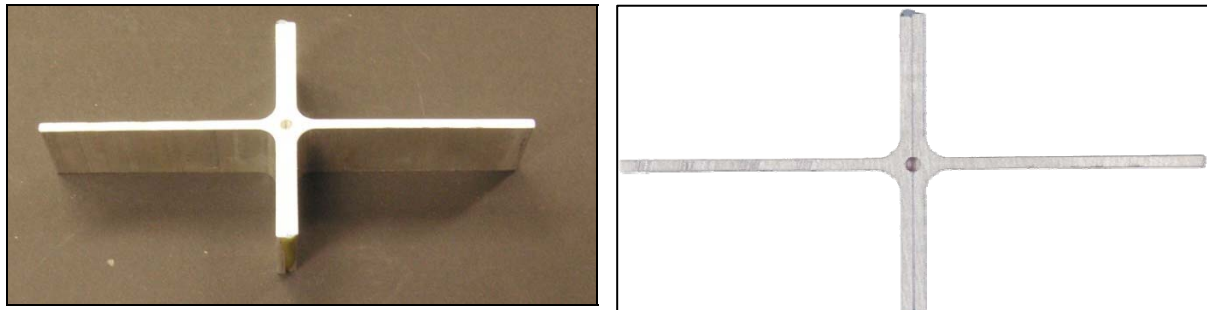


**Figure 9. A photograph of a Tee joint (left) and a scan of a Tee joint which shows off the bond-line better (right)**

Potential problems do exist with this joint, primarily that damage will likely occur at the noodle (leg-flange union) of a composite Tee [4]. This damage would obscure the damage at the joint rendering the test data unsuitable. Thus, modifications are required to use the Tee joint geometry for composite bonding.

The specimens used in the NRL study [1] use a notch in the composite sample to concentrate the stress state in a controllable manner. This strong geometrically induced strain concentration results in damage and failure zones well away from the grips and at a specific, desired location. This idea is similar to ‘dogbone’ shaped test specimens which attempt to force failure in the sample midsection, away from the grip stress concentrations. However, it goes well beyond this traditional technique in stress concentrations by causing well defined and localized stress/strain

states. The straight T-joint does not have the same grip failure problem because the joint is much weaker than the adherend. However, it does have a symmetry problem, in that most damage will occur at either of the free edges. A stress concentrator was desired similar to the composite notches and dogbone technique. Two methods were proposed and studied. The first was a drilled hole into one side of the joint at the interface. The second was a ‘reverse dogbone’ idea which can concentrate the damage at the center of the joint. Manufacturing and testing obstacles caused the ‘reverse dogbone’ geometry to be abandoned. The notched Tees were found to be easier to manufacture and provide consistent test results for tension tests.

Boeing provided the two sets of similar Tees used during testing and both film adhesives, FM300 and FM400. Light positive pressure was applied to the joints in the form of clamps or set screws. The bondline for all of the FM300 Tee joints was found to be a consistent 0.013” regardless of the type of pressure applied. This consistency is directly the result of the carrier mat in the placed in the film.

Parametric studies were performed with FEA to determine a good width and depth for the cylindrical drilled notch. An 1/8” diameter, 1/4” deep hole was found to produce desirable load concentrations in the joint for an aluminum/FM300 Tee joint. The test matrix of Tee joints is listed in Table 2. The Tee dimensions were; 0.10” thick x 2.5” flanges x 1” width (except for Tw & TLw which were 2”) with varied leg lengths (2.5 for T and 5.5” for TL series).

**Table 2. Test matrix for Tee joints**

series	sample #s	failure	machine	load path & comments
T	1,2,	mixed	Instron	tension, low failure loads
T	3,5,6	mixed	IPL	tension, low failure loads
T	4,12	none	IPL	lateral & moment paths, large slip
T	6a,7,8	cohesive	Instron	tension, good data
T	9,10	cohesive	Instron	tension
T	11,13,14	varied	Instron	tension, varied failure loads
Tw	1	cohesive	IPL	tension
TL	1,2	varied	Instron	tension, varied failure loads
TLw	1,2,3	varied	Instron	tension, varied failure loads

\*total of 20 Tee joint tests performed

### Test Results

A total of twenty Tee joints were tested in tension on both an Instron 8550 and the MSU-IPL. No differences in failure load or failure surface were found between the testing machines. However, displacement data acquisition was quite different between the machines. Head stroke and extensometer were used in the Instron tests while LVDT and image correlation were used for the MSU-IPL. Neither Instron head stroke nor MSU-IPL LVDT data was found to be accurate compared to image correlation data which is assumed to be more accurate. However, the image correlation data was found to be more noisy and difficult to work with.

For ten tension tests which had adequate data, the data were subdivided into sets of five based on preparation methods. The first five (T1-5) came from the same batch and failed at an average of  $1180 \pm 71$  lbs. All five failure surfaces showed interface failures as the dominant failure mode. The second five (T6-10) failed at  $1870 \pm 76$  lbs. These five consistently failed cohesively at the carrier mat (the mat grid is easily observable). While the mat provides a consistent bondline, it also acts as a saw, cutting the adhesive neatly in half. Due to the marked and consistent difference in failure load and type, it was concluded that poor preparation resulted in the interface failures and lower loads found in the first five tests.

All ten tests showed the same progression of damage observed as distinct changes in the failure surfaces. A picture of a Tee-joint showing the crack opening is shown in Figure 10. Representative failure surfaces with damage zones highlighted are shown in Figure 11. The first damage stage is always found near the free edge of the notch (highlighted by the red lines). The second stage is defined by a cone surrounding the notch (orange lines). The dashed lines connecting the cone with the opposite end define a possible extension of the second damage zone. This area is much more difficult to see than the cone region and it is uncertain whether it belongs with the conical damage zone or is a separate intermediate damage zone. FEA load predictions suggest that the damage does extend all the way through the joint as shown by the dashed lines. The next damage zone migrates out to the flanges and ends with a relatively rectangular shape (yellow lines). The next zone results in the final failure of the Tee.

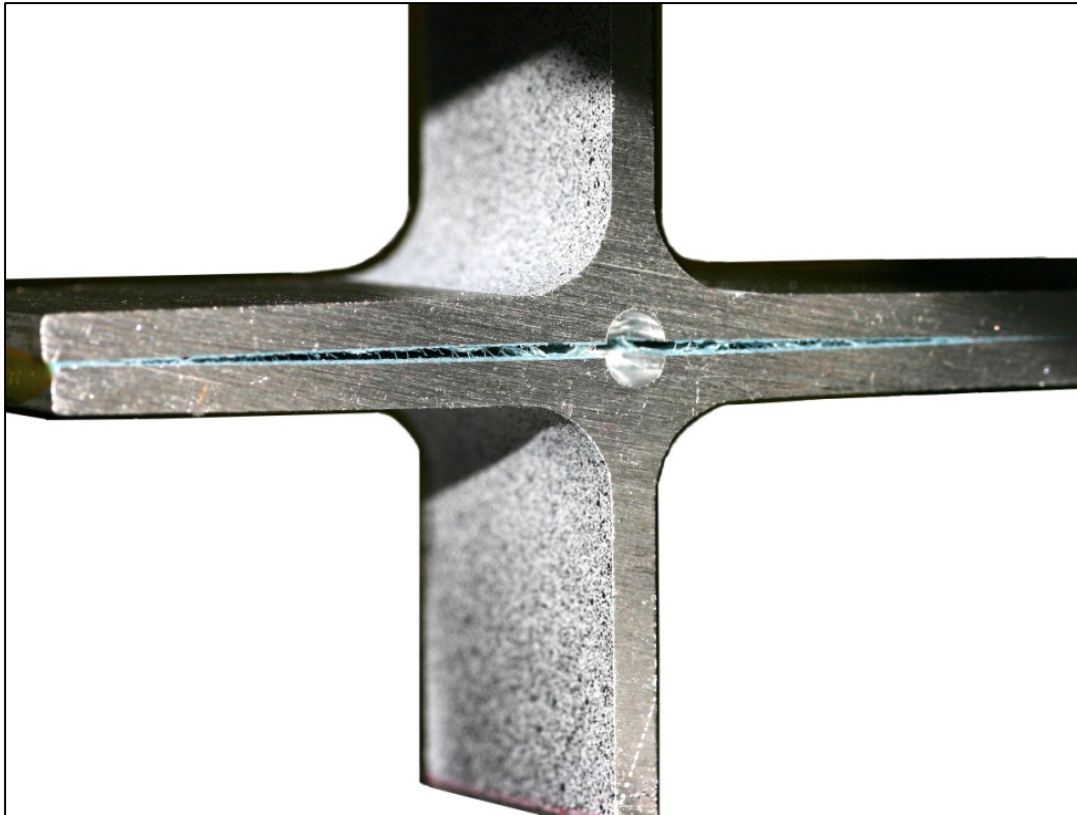


**Figure 10. Picture of a Tee under a tension load showing an expanded crack.**

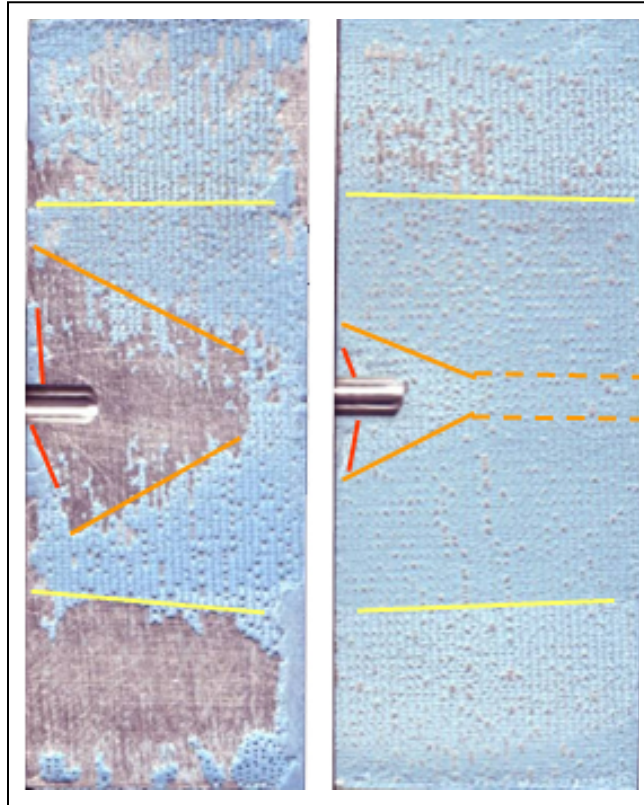


**Figure 11.** images of the failure surface of a Tee joint tested in tension (left) poor adhesion (right) good adhesion

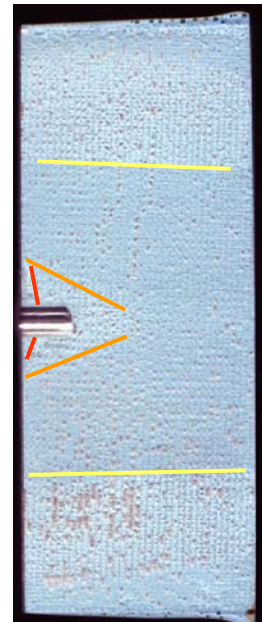
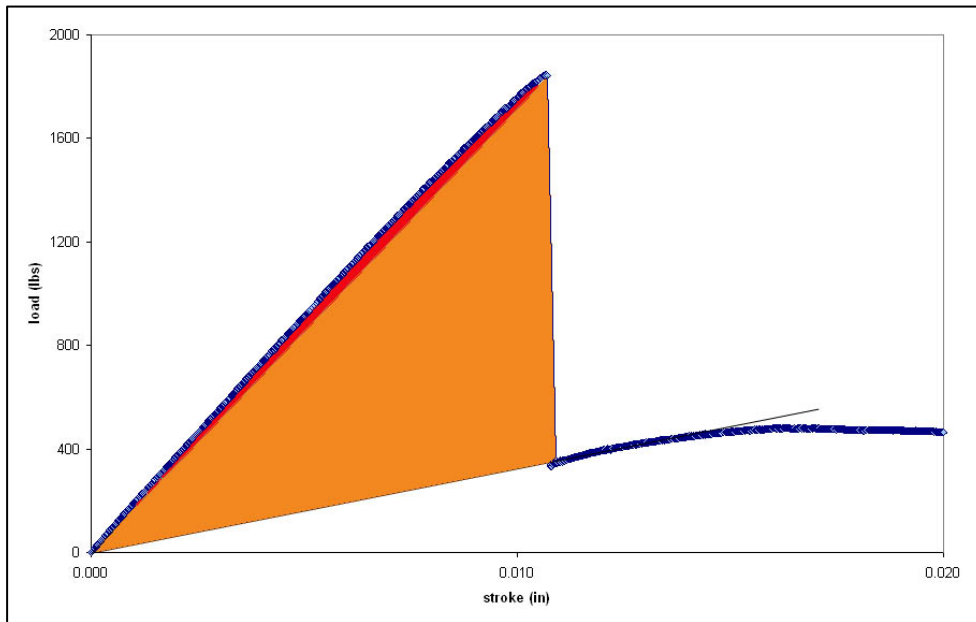


**Figure 12.** Dissipated energy of a Tee joint tested in tension (left) load history with two areas of dissipated energy, red & orange, (right) which correspond to the colored lines in the image

A typical load history of a tension test is shown in Figure 12. The initial linear response of the structure begins to deviate as it damages. The softening that occurs suggests that the adhesive is undergoing some damage beginning from ~1100 lbs. The sharp drop in load is associated with a crack jumping through the adhesive. The drop is associated with a loud pop and a small crack was observed at this time. The dissipated energy associated with red and orange damage fronts (right picture of failure surface) are the red and orange areas of the load-deflection curve (see FE section). After the load drop the joint reloads along the secant modulus before damage begins to soften the response again.

### Finite Element Analysis

The Tee joints were modeled in Ansys with a half symmetry 3D model using 20-node brick elements. The loads were applied as uniform displacements at the grip. The adhesive was modeled using manufacturer supplied material properties ( $G = 57$  Msi). An example of the FE results is shown in Figure 13, which shows the tensile strain of a Tee joint under tensile loading. Note the strain is concentrated in the adhesive layer at the notch tip.

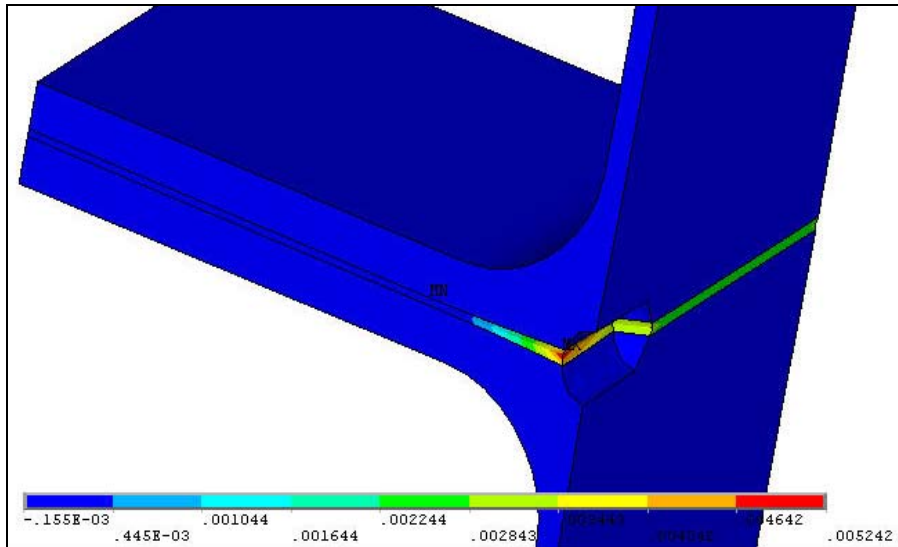


**Figure 13. Example results of the tensile strain of a Tee joint under tension**

By comparing the results of the FE model to the test results, a damage estimate can be made for the state of tension. The initial deviation from the linear response gives us an approximate load at which damage begins from peel strains. By equating this load with the FE model we can predict the strain energy density at which damage begins for FM300 in the pure peel strain condition as  $1060 \text{ in-lb/in}^3$ , which is at a stress of 10200 psi and strain of 5.2%.

It was postulated that the Tee joint would allow the IPL to more directly apply the types of strain to the adhesive layer due to its perpendicular alignment to the loading plane. FE analyses confirms that this is the case. Figure 14 plots the strain energy densities in the adhesive layer for

Tee-joints loaded in vertical and lateral directions. In the vertical case (tension), the strain energy density is highest at the notch tip which is in a strain state of general tension (peel strain). For a lateral loading, the hotspot is located near the center of the adhesive, near the notch root. The adhesive in that region is in a shear dominated strain. Thus, the Tee joint seems to be a good choice as a MSU-IPL test geometry because the strain states can be controlled and the potential damage sites are distinct.

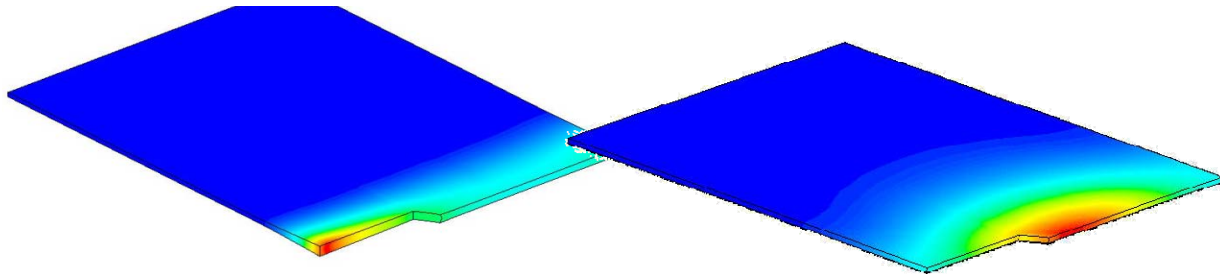


**Figure 14. contour plots (3d) of the strain energy density of the adhesive layer in a Tee joint (left) in tension (right) in lateral deflection (shear)**

To better understand the load-deflection curves and the damage fronts found in the tension tests, two finite element models incorporating cracking were developed to study the second, conical damage zone. The first models the just conical damage region by subtracting a thin volumetric region, creating a crack. The second model starts with this conical crack and extends the crack from the cone, straight back to the opposite edge (as seen by the dashed lines in Figure 11). The crack front dimensions for both were taken as the average of the measurements taken from samples T8 and T9. The results are plotted in Figure TDM next to the response of test T8. The undamaged FE stiffness is slightly lower than T8 but close enough to be considered an adequate model of test T8. The stiffness of the conical damage model falls too far to be the slight damage associated with the first damage region but does not drop enough to be a reasonable model for the crack front after the major load drop. The stiffness of the extended conical damage model is much nearer to the stiffness of T8 after the load drop. Thus, it is concluded that the major load drop drives the crack all the way through the sample and is associated with the extended conical damage region. From there it is argued that the softening is associated with some small damage accumulating around this damage zone. The next major load drop (not shown in any figures) is then associated with the jump to the third damage zone in Figure 15 (yellow lines). Further load drops follow the same pattern until final failure of the joint.

Material characterization was not performed for the adhesive using the Tee joint tests because of difficulties obtaining adequate test data from these tests. However, it may be possible to use some of the tension test data for characterization.

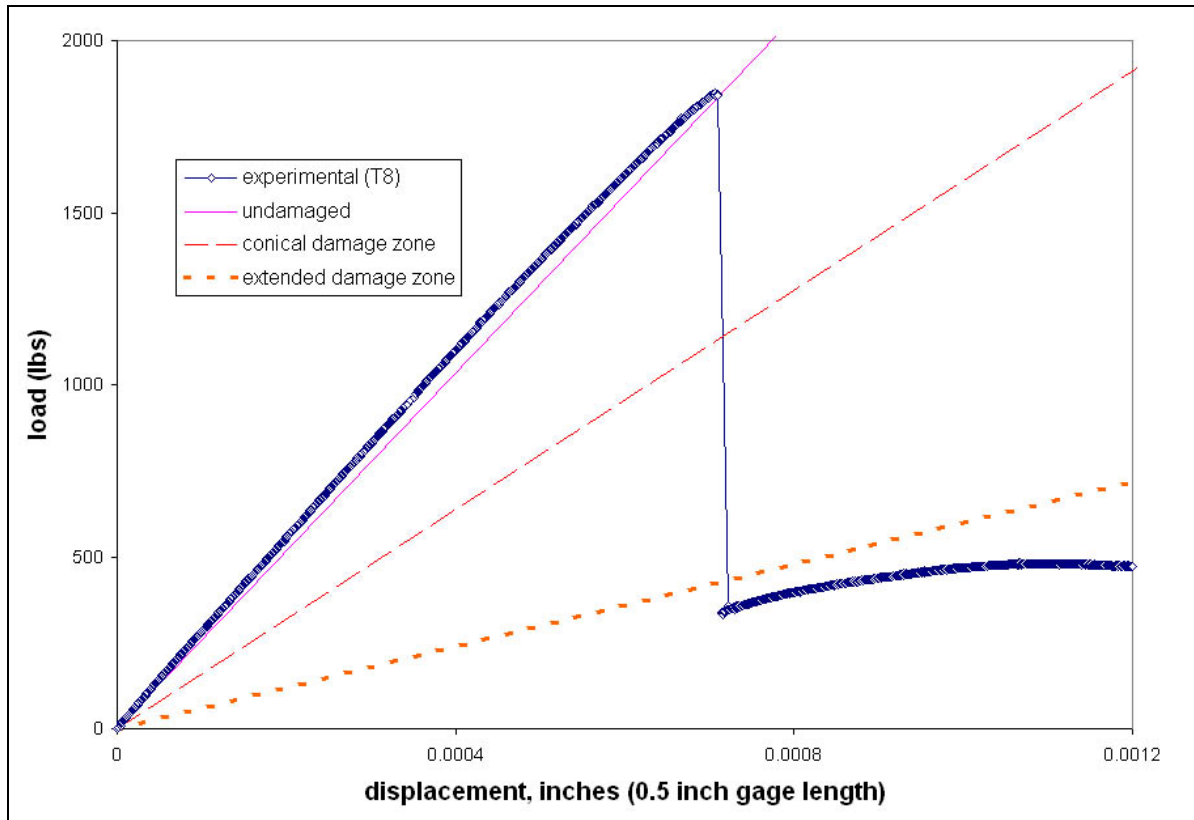


**Figure 15. Comparison of FE predictions to test T8**

### **MSU-IPL Joint Related Problems**

The MSU-IPL was designed and constructed by a series of students to study small notched fiberglass samples. In subsequent testing of carbon/epoxy samples, it was found that these samples needed to be very thin to limit the sample stiffness. The problems with the stiff carbon samples were related to out of plane deformations and reaching or exceeding the load capacity of the machine. These problems became exaggerated due to the high stiffness of the Tee joints. Other problems included large amounts of grip slipping in rotation and lateral load paths (see Figure 8) and data resolution. The output of a Tee joint test, sample T8, is plotted in Figure 16. Compared to the data shown in Figure TTD (which is from a uniaxial Instron 8??) the IPL data is sparse and jumpy. Both the LVDT and image correlation (IC) data have unexplainable jumps in stiffness. The scattered nature of the data also makes it difficult to discern whether damage has initiated or if the modulus drop is data scatter. The lateral and rotational paths showed even greater data scatter. These paths also resulted in off-path output that was very significant. For example, for one lateral path the tension loads were of higher magnitude than the lateral loads. For these reasons, the current MSU-IPL was found to be inadequate to properly test Tee-joint samples. Modifications to the Tee-joint geometry to make the Tee more compliant will result in an unsatisfactory joint. A more compliant (softer) Tee joint under lateral loads will bend and rotate which will result in adhesive no longer in nearly pure shear but rather some combination of tension and shear.

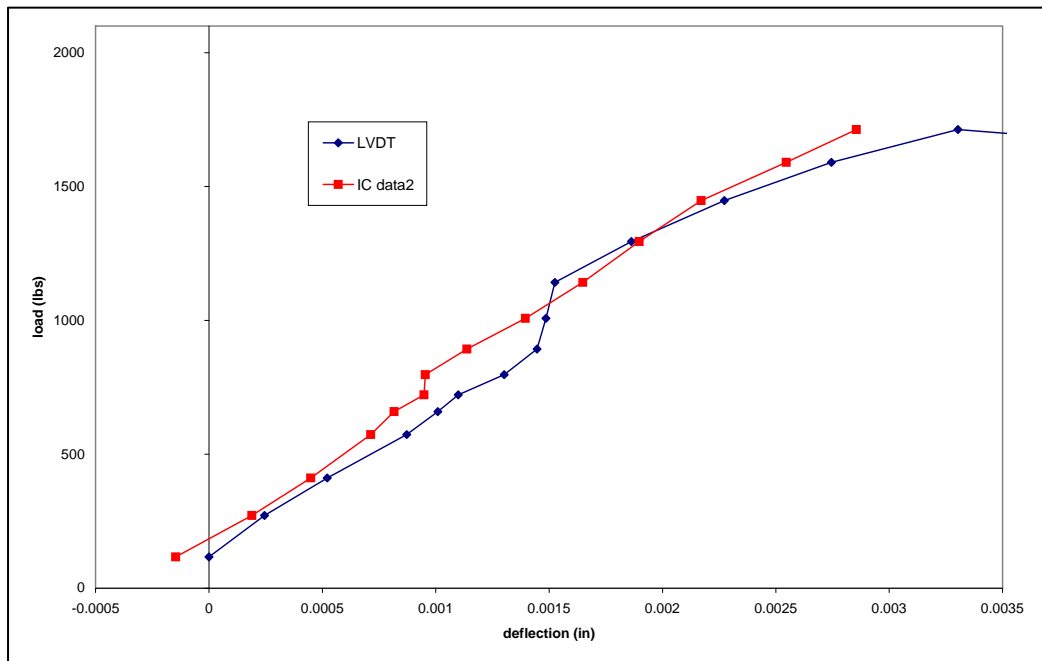


**Figure 16. example of the data output of the IPL testing a Tee joint in tension**

## MIXED MODE BENDING JOINTS

The inadequacies of the MSU-IPL to test the Tee joints necessitated a new approach to the testing of joints. The original approach was to use one joint geometry and test it under multiple load paths in a multi-axial testing machine. The modified approach is to use a uni-axial testing machine with multiple geometries or a testing jig that transform the single load path into multiple paths.

A series of tests that applies the latter approach uses the mixed mode bending (MMB) testing jig. The MMB jig is shown in Figure 17 along with the end notch flexure test (ENF). The MMB test is used to calculate the energy release rates of cracks grown with varying degrees of mode I (opening) and mode II (shear) fractures. The extremes of the MMB tests are the dual cantilever beam (DCB) for pure mode I and ENF for pure mode II fractures. If these tests are viewed from the perspective of dissipated energy instead of fracture mechanics, the stress concentrations causing failure would be nearly pure tension (DCB) or nearly pure shear (ENF). The MMB tests would then represent damage along a strain vector with a significant combination of both tension and shear. Further, the Teflon in these tests is not viewed as a crack, but rather as a material discontinuity that is a stress concentrator like the notches in the IPL sample. Similarly the MMB testing jig serves as a substitute for a multi-axial testing machine by changing the uni-axial loads to multi-axial loads.

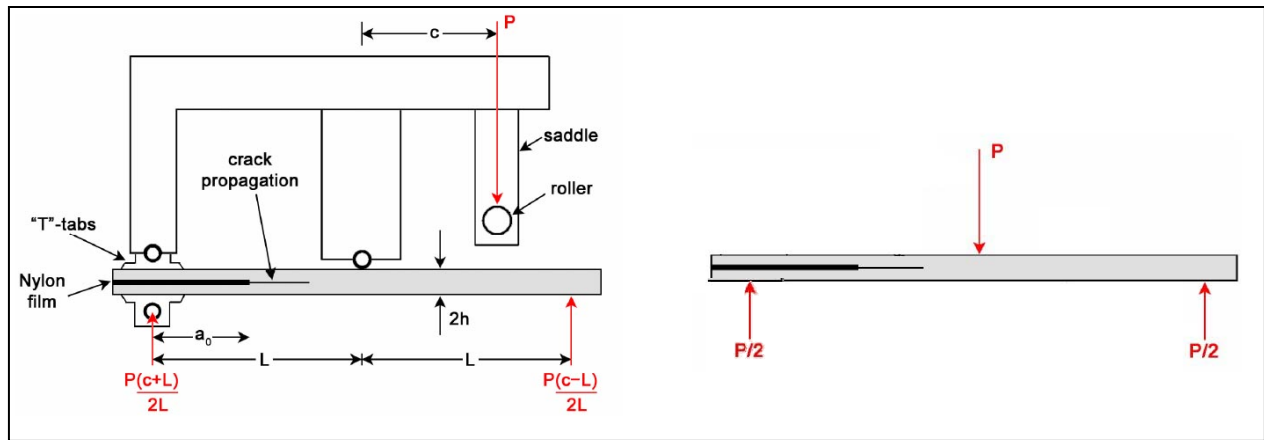


**Figure 17. Schematics of the MMB (left) and ENF (right) tests**

An ENF style test and the resulting failure are shown in Figure 18. While the ENF test is basically a three point bending test, the deformation is not symmetric. The Teflon strip allows the adherends on that side to move partially independently of each other/without the effects of shear. This causes a stress riser at the Teflon/adhesive interface. The Teflon insert can be seen in both images. As seen in the close-up image, the single Teflon sheet is folded to match the natural thickness of the FM300 due to the carrier mat which is ~ 0.013 inches. The failure site is located at or near the Teflon interface. For this sample it occurs approximately halfway up the curve of the Teflon radius from the bottom (~1/4 of the total adhesive thickness). The failure then jumps to the top interface and then back down to the bottom interface.

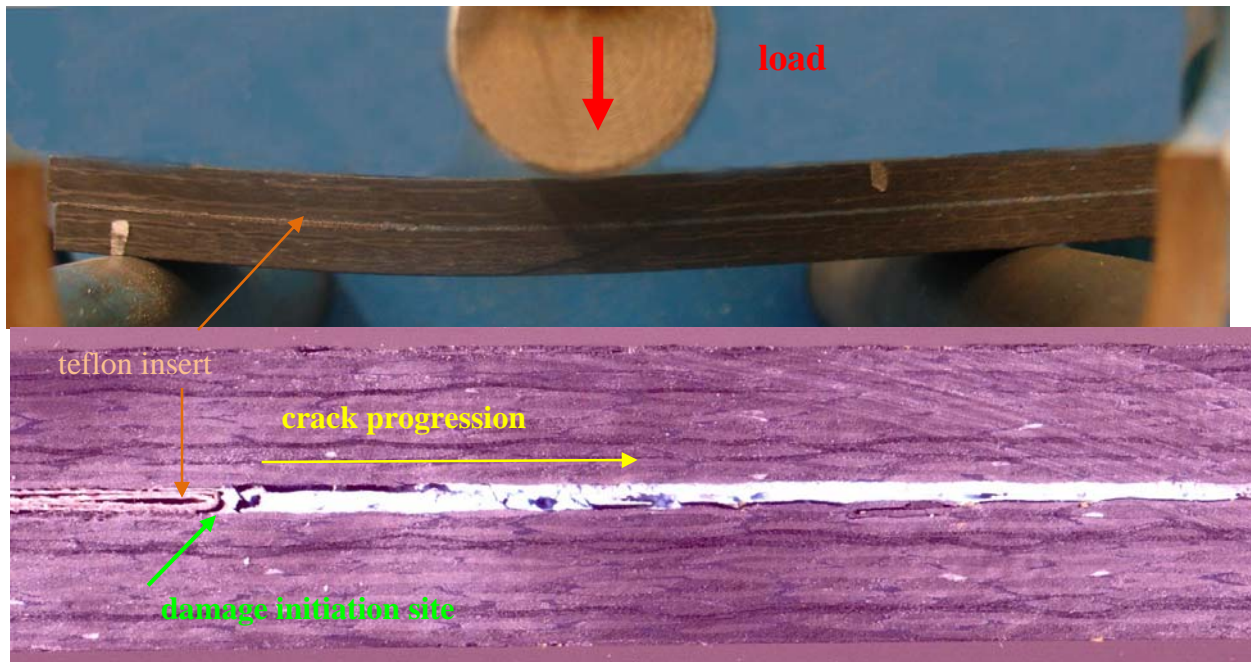


**Figure 18. (top) An ENF joint being tested (bottom) a close-up of the failure region of the ENF test shown above**

A sample load history for the sample B3-ER04 ENF test is shown in Figure 19 (see Table 3 for a listing of the ENF test matrix). Two loadings of the same sample are shown. The first data set shows the initial loading and the unloading of the test. This data set shows the loading response features of all the subsequent ENF samples tested. First, the linear response covers a majority of the response, starting just after a slight load nose engagement period and ends with damage onset. A red dashed line has been superimposed on the response to help define the linear region. Damage onset occurs at the deviation from the linear response. It is unclear what type of damage is occurring at this time. At the maximum load the crack begins to grow very quickly and reaches the loading nose. When the crack reaches the loading nose its growth is arrested and a stable response begins. Continued loading results in eventual damage to the adherends. The unloading curve shows a slight curve as it returns to zero load. While a residual strain seems to be present no permanent damage is seen in the sample when fully unloaded. (Note: samples with damage to the adherend always show a permanent ‘V’ shape when unloaded). When this sample was loaded a second time, the response follows the secant modulus and runs through the point at which the crack self arrests. This means that most of the damage is dissipative and not plastic. (It is still possible that plasticity is accruing at the Teflon interface.) The dissipated energy of the structure is the area between the two loadings. For some tests, a large gap in data points occurs as the crack jumps quickly to the nose. These jumps were accompanied by a loud pop. In contrast the more populated drops in load give off no sound or lighter cracking noises.

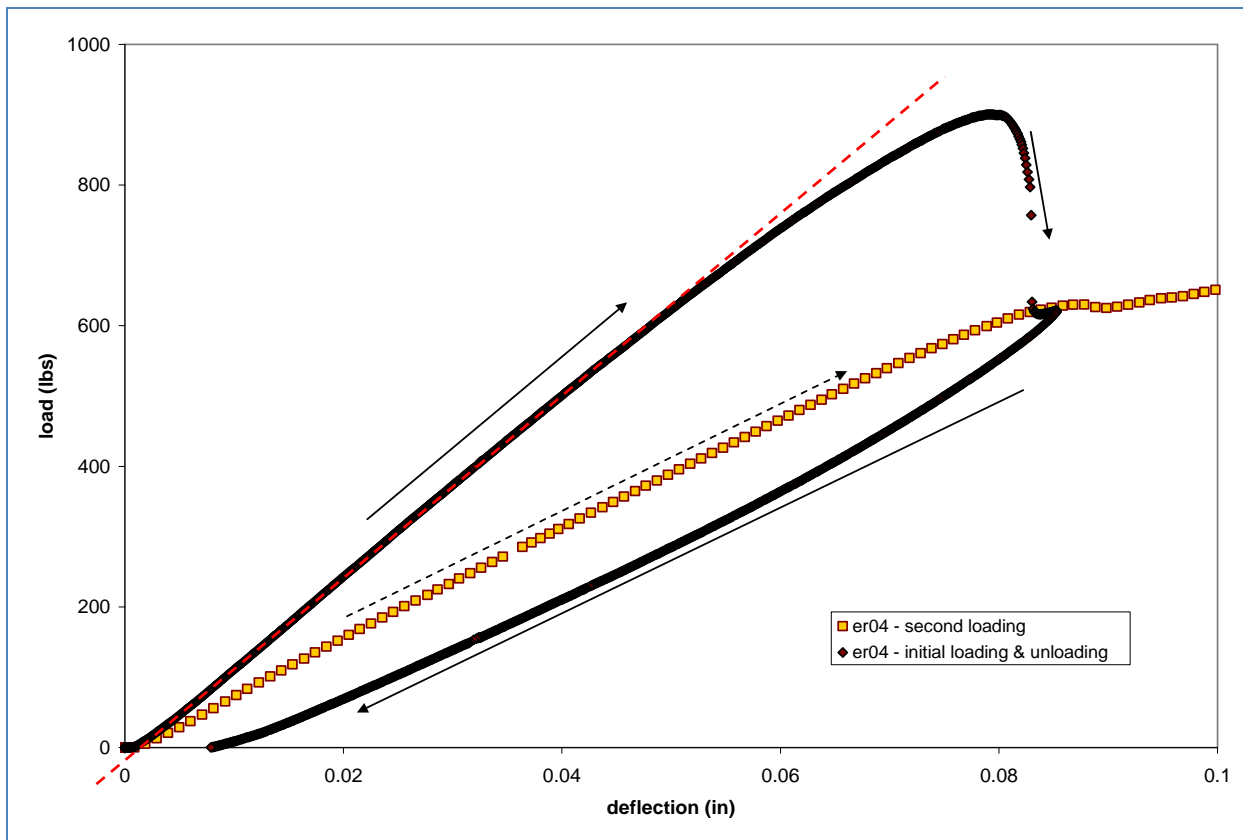


**Figure 19. Load history of an ENF style test with loading & reloading**

## ENF geometry limitations & options

During testing it was found that some aluminum ENF geometries were too thin which caused plasticity in the adherend rather than damage in the adhesive. An example of the response is plotted in Figure 20. The unloading of these tests follow the same slope as the linear region of the loading curve which is a characteristic of plasticity. These samples also remained in a ‘V’ shape confirming residual strain and thus plasticity did occur.

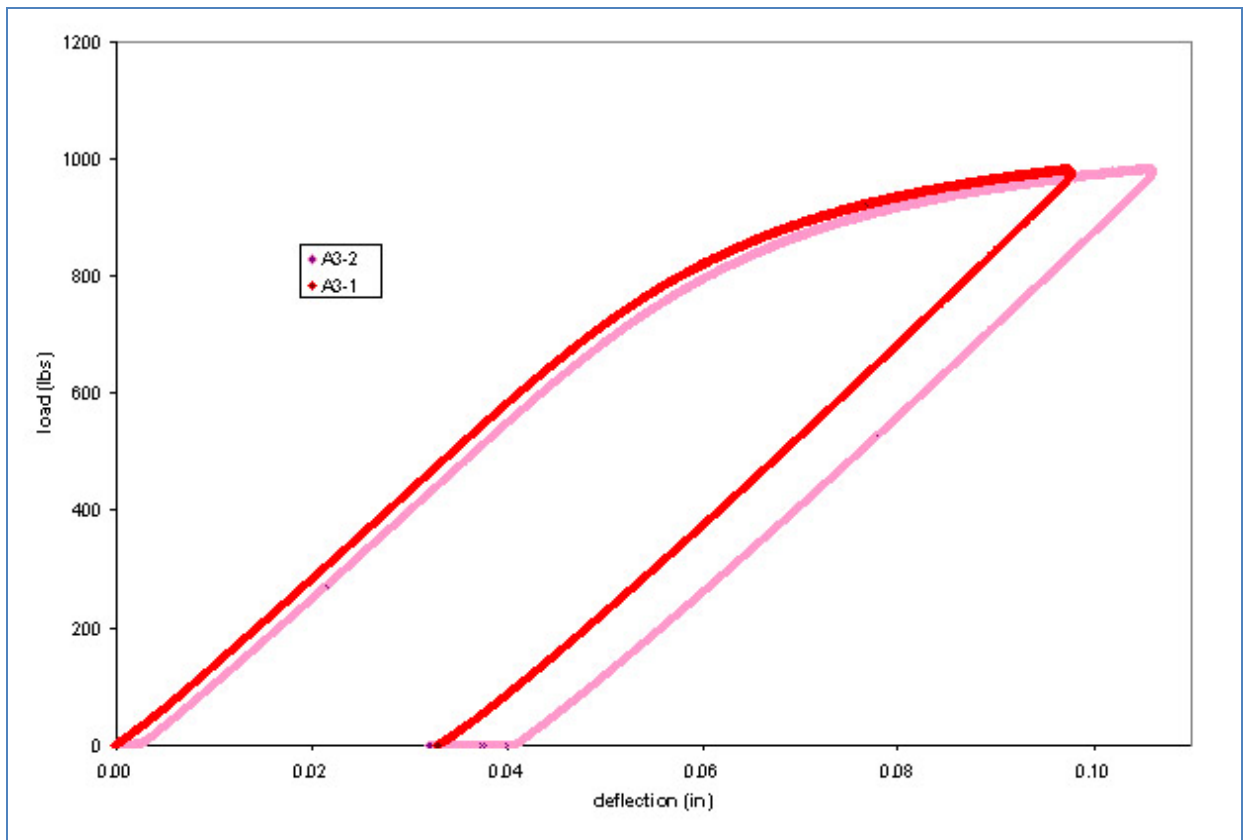


**Figure 20.** Example of the loading and unloading response of an ENF test which underwent plastic deformation rather than adhesive damage.

ENF joint tests with equal adherends on either side place the adhesive in the neutral axis of the structure during bending. This causes the adhesive to strain mainly in shear. To capture a larger strain space for material characterization, adherends with unequal thickness are used to move the adherend away from the neutral axis and shift the strain space toward more tension or compression. This is a philosophic change from the multi-axial testing which used one sample geometry and multiple load paths to achieve a wide strain space. However, it is still possible to perform the same analyses procedure to characterize the adhesive. It is also possible to slightly alter the strain state or its intensity by changing the length of the Teflon insert.

The following test matrix, Table 3, shows the tests performed with the ENF joint geometry and Figure 21 is a picture of four of the test geometries.

**Table 3. Matrix of ENF style tests**

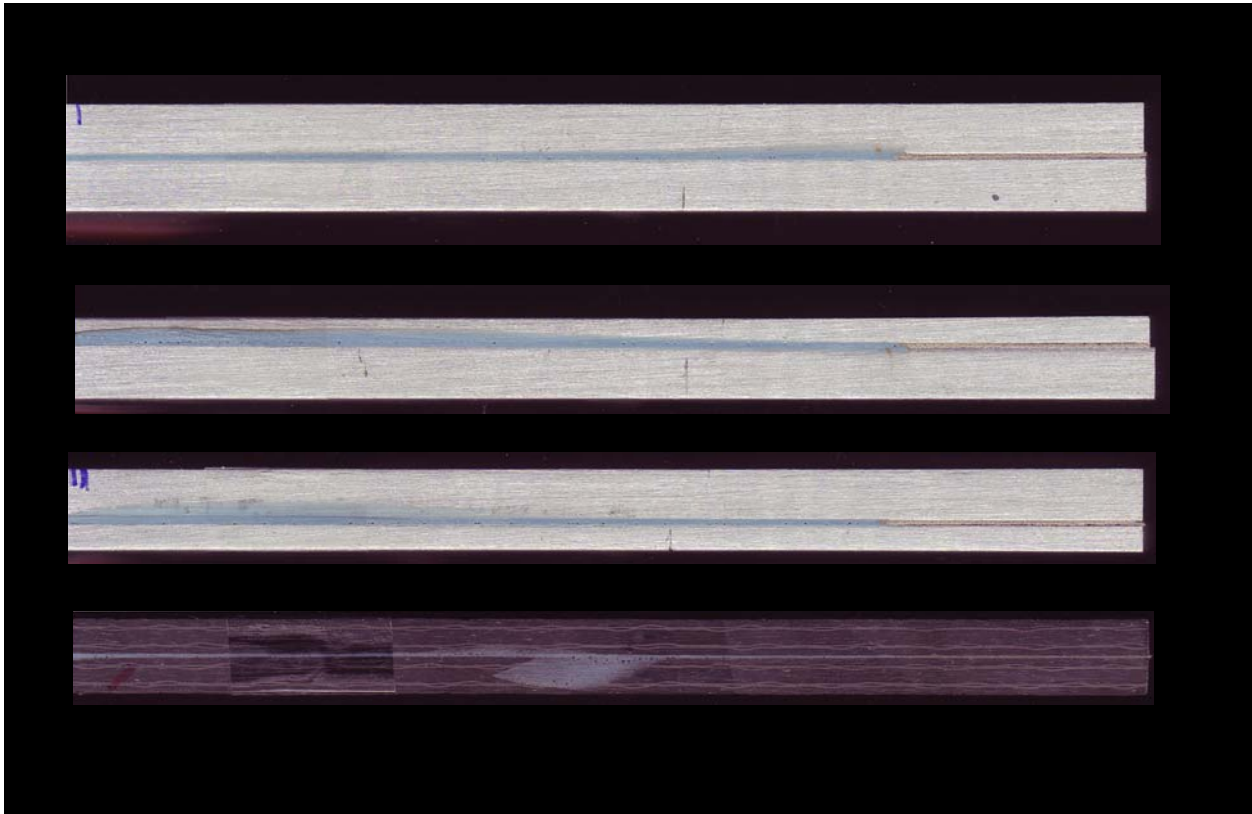
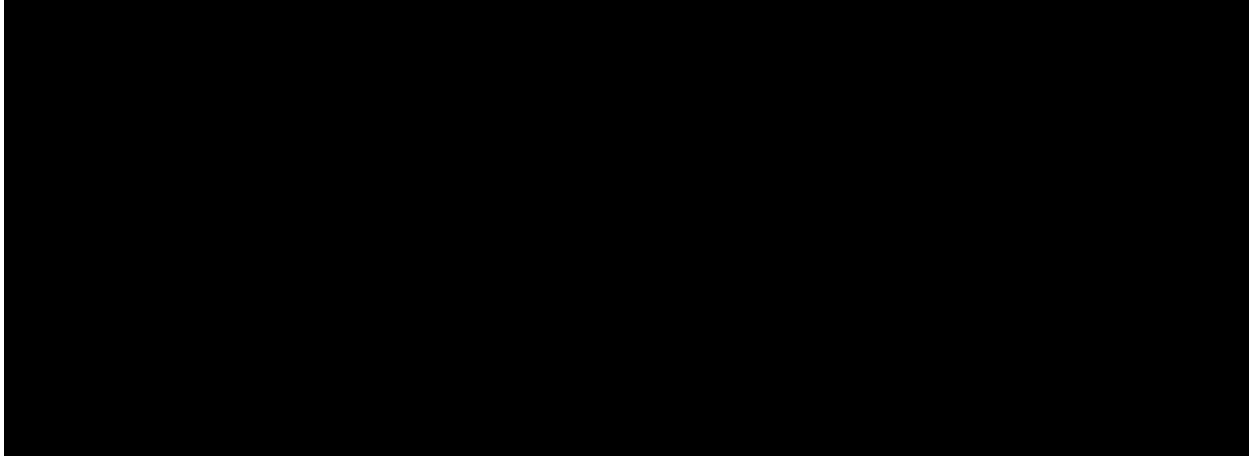


**Figure 21. Examples of various ENF samples, from top down, A3Q, A3Ua, A3Ub, B3-ES**

## Test Results

Results for three test geometries with different aluminum adherend thicknesses are plotted in Figure 22 (six tests total). Test Cases A3-Ua and A3-Ub have unequal adherend thicknesses which are opposite of each other. Series A3-Ua has the thinner adherend as the top adherend while A3-Ub has the thinner adherend on the bottom. These two test cases have the similar responses which is expected because they have equal linear bending stiffnesses. The two stiffer cases, which have equal thickness adherends, have equal thickness but different Teflon lengths. Sample A3QS-2 has a longer Teflon length which makes it slightly more compliant in the linear region as well as damage and fail at lower loads.

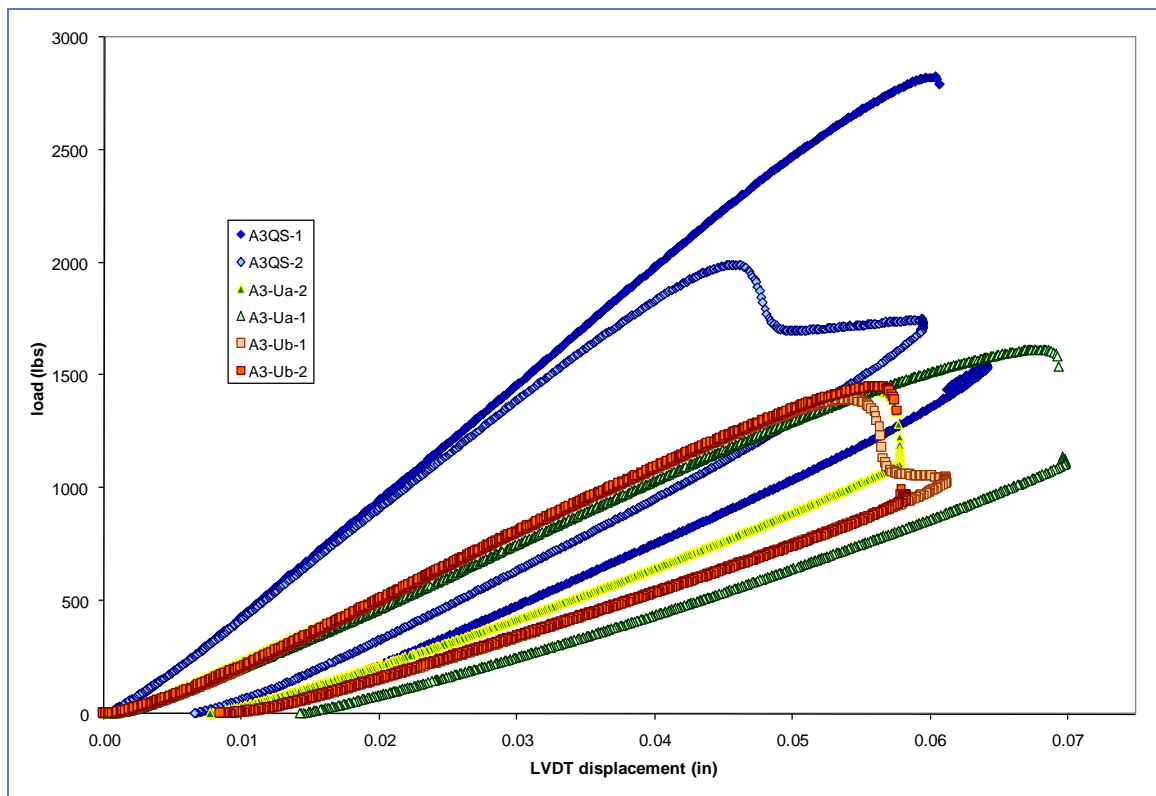


**Figure 22. Example Plots for six ENF tests**

The B3-ER and B3-ES series only differ by the surfaces which were bonded together. The carbon/epoxy adherends supplied by Boeing have a smooth surface on one side (call plate side) and a rough surface finish on the other due (bag side) to manufacturing methods. To determine which side was superior for bonding strength, tests were performed with bonding to the smooth sides (ES) and rough sides (ER). The results are tabulated in Table 4. Statistically there was no significant difference between the maximum loads of the two test series. However, the smooth surface bonded test cases would typically fail with a loud pop while the rough surface tests would usually fail without any audible signs (however, the test machine is quite loud and lower volume sounds will be lost to the observer). A supporting trend is found in the load deflection curves of the two cases, plotted in Figure 23. After the load drop due to crack initiation the ES

sample data tend to have a large gap which is most likely due to very high crack speeds and the audible pop heard. By contrast the rough surface data tends to contain more data points throughout the load drop which supports the idea of a slower crack speed. A mixed surface test was also performed (EM) which but few conclusions can be made from this single test.

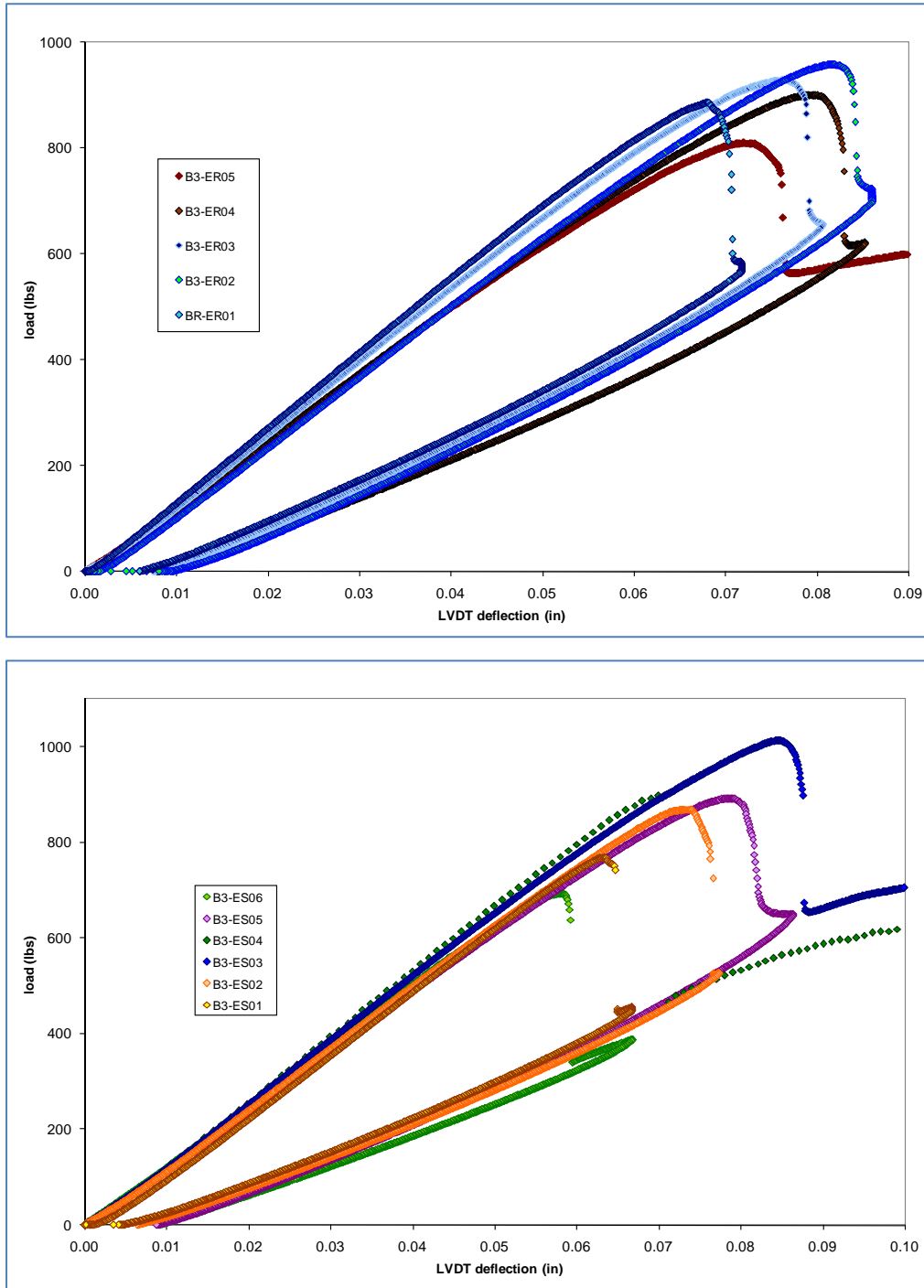


Figure 23. Load-deflection plots of test series B3-ER (top) and B3-ES (bottom)

**Table 4. Maximum loads of ENF style tests which had rough or smooth bonding surfaces**

interface	max load (lbs)	st. dev	# tests
smooth	863	103	7
rough	897	56	5
total	881	88	13

### Finite Element Model

Due to the asymmetries of the MMB style tests, a full 2D model is required to properly model the response. All bulk materials (adherend, adhesive and teflon) were modeled with 8-node plane elements (plane82). The material properties of the composite adherends were modeled by layers. The most likely area for damage onset is the teflon/adhesive interface. The mesh in this region is extensively refined to obtain better, more continuous strain fields. The teflon interfaces are primarily modeled with contact elements. Normal contact is governed by lagrangian methods (no penetration) while sliding contact is governed by penalty methods. However the bulk of the teflon to lower adherend interface is directly meshed together. This is done to mitigate solution problems and solution times. The lower teflon interface near the adhesive interface is not meshed together and is governed by contact elements to make this important area more self-similar (symmetric). A sample mesh of the interface region is shown in Figure 24.

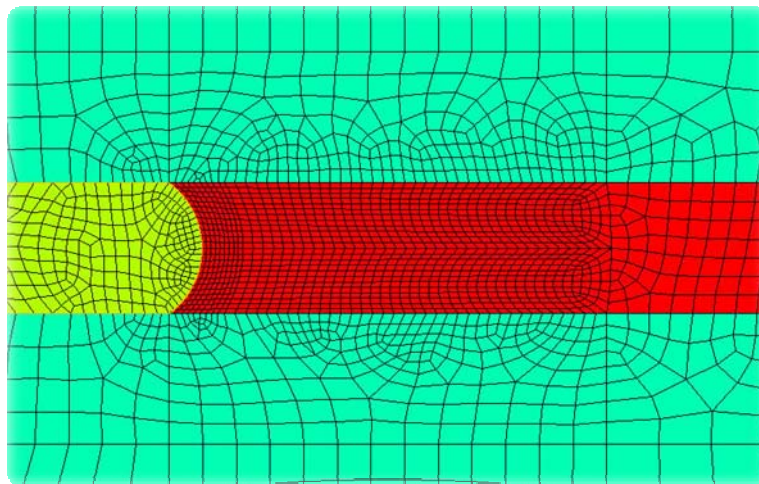


**Figure 24. Teflon interface of a MMB mesh (the adhesive material is red, the Teflon is green and the adherends are cyan).**

### FE Results

A strain energy density plot of the teflon edge interface is shown in Figure 25. The hotspots are located at the  $\sim 1/4$  and  $3/4$  of the adhesive thickness just off the teflon interface. The lower hotspot coincides with the initial failure site shown in Figure 18. Three plots of the strain energy

density and deformed shape are plotted in Figure 26. These plots are from loads in the nonlinear response of the structure. The adhesive in this model uses a tri-linear nonlinear response and all three plots have adhesive material in the nonlinear regime. The loads in these three plots correspond to the loads used for the nonlinear characterization of the adhesive (detailed later). The white gaps in these figures represent the separation of the adhesive from the Teflon.

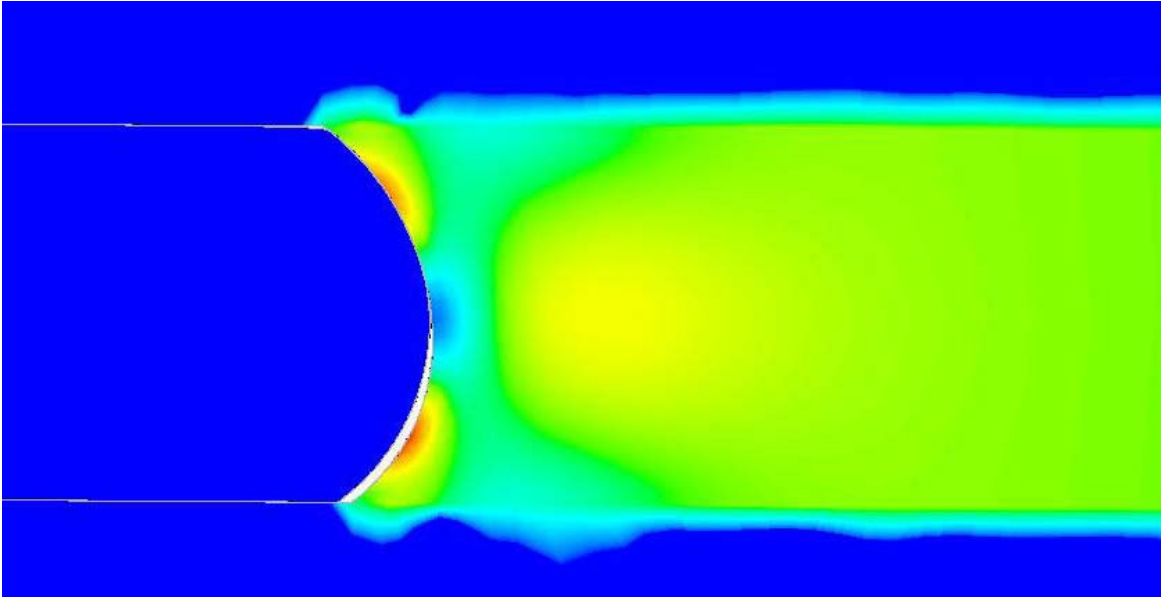


**Figure 25. Example of the strain energy density contours of around the Teflon interface of case ALC2 in the linear response of the structure and adhesive. Red colors indicate the highest strain energies while blue are the lowest.**

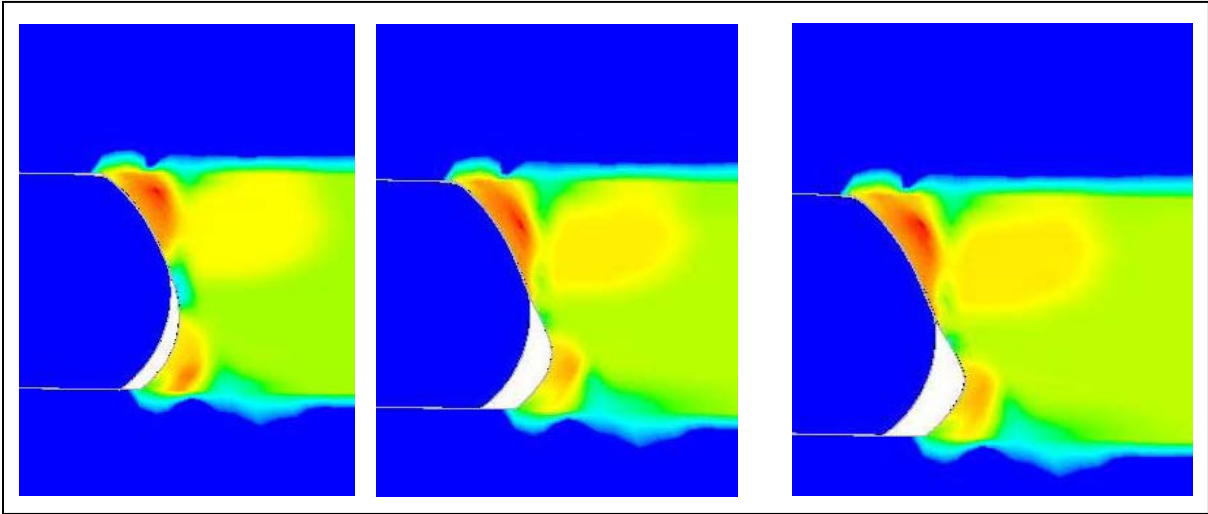


**Figure 26. Evolution of the deformed shape and the strain energy density at the Teflon interface for the model of ALC2. All three pictures are in the damage zone and have nonlinear response in the adhesive material.**

## **Effect of unequal adherend thickness**

The idea behind testing unequal adherends is to shift the adhesive from a state of mostly shear into states that include more tension or compression. Unfortunately, the stiffness mismatch between the adherends and adhesive tends to cause the adhesive to primarily shear. This results in the two adherends bending semi-independently. This behavior is most prevalent with the aluminum adherends. Thus, while the strain states do change, large areas do not shift into the combined states. Thus, to obtain a wide strain space for characterization ENF geometries will not fully suffice, and MMB and DCB geometries are required.

## **MATERIAL CHARACTERIZATION**

### **Approach & Assumptions**

The accuracy of the deflection data from the uni-axial machine has significant error due to grip movement, engagement and other unknown sources. The error is also a function of the sample stiffness. The expected linear region of the response does follow a linear path and thus we deduce that the error is of a constant proportion in this region. Several three point bending tests of simple aluminum strips were performed to assess the error. The known modulus of the aluminum is 9.7 Msi, and so the error can be calculated by its difference from the linear solution. For the three thicknesses tested, 0.130, 0.190, and 0.250" (0.001"), the error was 1 , 4 and 8% respectively. These are the same stock of aluminum used as adherends in the ENF joint tests. The error can be seen to increase with sample stiffness. The stiffness of the ENF geometries are much higher because the total thickness is at least 0.44" for the aluminum based geometries and 0.35" for the carbon geometries. Thus we can expect large errors in the LVDT readings of the ENF tests.

Through a simple parametric study varying the adhesive modulus, the overall stiffness of a typical ENF sample (ALC-1) only changed by 4% with a 50% change in adhesive modulus. This is a significant observation as it defines the dominance of the adherend in the overall joint stiffness. A major goal of the study is to characterize the adhesive response in the joint. This is to be accomplished by optimizing the FE model to match the test data. In our analysis we assume to know the adherend properties while the unknowns are the adhesive properties. Thus any small error in test data will cause the solution for the adhesive properties to have a much greater error, even up to an order of magnitude greater. The data collected is known to have large, but unknown error, hence either better (and excellent) data collection methods must be used or the analyses needs to be altered to accommodate the error. One solution was to use optical methods similar to those employed in the IPL study. However, those methods were found not to be very precise and we would still end up with errors high enough to produce very large differences in the adhesive characterization values.

A primary goal of the study is to define the onset and growth of damage in the adhesive of a joint. The linear modulus of the adhesive can be obtained more straightforwardly in a neat adhesive test. The manufacturer provides this data and if this is assumed to be correct, hence all of the linear properties in the joint are known. With this accurate knowledge, an FE model is

assumed to accurately predict the linear response of the structure. Any difference between the FE model and the experimental data is then due to the unknown error in data collection. Thus, by correcting the input deflection by an error coefficient we may assume the FE joint accurately represents the experimental joint. In this way we treat the error as an unknown and solve for it. At this point, we must concede that this assumption of FE accuracy is only a means to help us characterize the nonlinear adhesive response.

Unlike the linear properties, which are dominated by the adherends, the damage in the joint is wholly due to damage in the adhesive (this assumption must be checked for each test case). For example, looking at the typical ENF response in the preceding figures (ENR,SRT,FEN) we can safely state that the softening of the response (deviation away from linear) is caused by damage to the adhesive. Since we know that any changes in the adhesive properties must be large to overcome the dominance of the stiff adherends, we deduce that the adhesive properties have changed drastically away from the linear response. This results in a strange paradox, in that it is more difficult to find the linear effects of the adhesive than the nonlinear effects. In this manner, by assuming the linear properties are known, the nonlinear adhesive properties may be found by optimizing the FE model response to the corrected experimental data.

It is worth stating that taking the value of the maximum strain in the adhesive, at the load which the structure begins to deviate from linear, will not give an accurate damage onset strain. The two reasons for this are as follows. First, by the point the structure sees nonlinear behavior, the adhesive has surely damaged over some small area. This will result in a non-conservative value for damage initiation strain. Secondly, the highest strains will often occur at discontinuities or hotspots which are difficult places to obtain accurate results as they are often highly mesh sensitive. Thus, the damage initiation strain must be found through methods which incorporate damage growth. This brings up another point, in that for the structure to see significant change a moderate area of adhesive must be damaged. This tends to blunt out the effect of strain concentrations, but may lead to problems with material characterization for a wide strain space.

For a point in the adhesive, the onset of damage is defined as the strain point at which the response deviates from linear. At this point, the material begins to dissipate energy and its material properties degrade. This damage onset point will change depending on the strain state. For example, the state of pure tension will begin to damage at a different strain than it might in compression. The damage growth will also take a different form for different strain states. In this study the material nonlinearities are dependent on the strain state and left as variables to be solve for via optimization techniques. Each unit strain vector (which can also be thought of as a strain ratio state or strain direction) will have a distinct damage initiation point determined by a strain energy density damage initiation value,  $U^*$ . The values of  $U^*$  over the strain space defines our damage initiation envelope.  $U^*$  is a function of the modulus and strain state. Since the modulus at this point is linear,  $U^*$  can also be defined as the strain vector,  $\{\epsilon\}^*$ . An example of this state is shown for a tri-linear material response in Figure 27.

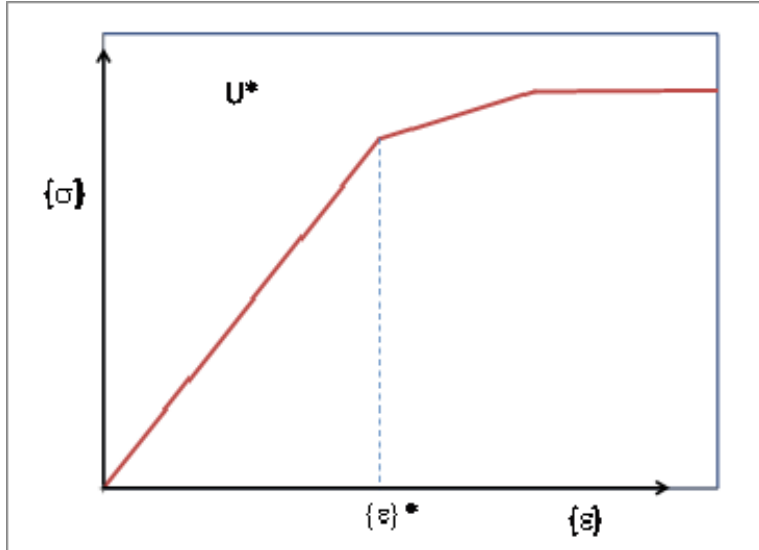


**Figure 27. Tri-linear constitutive response**

The unit strain vectors make a continuous set. To apply strain dependent material properties for FE modeling these sets must be discretized into strain ranges, here they are called sectors. The MMB style tests can be accurately modeled using a two dimensional model. The carrier mat in the FM300 is assumed to have a negligible effect on the linear properties and is modeled as an isotropic material. This results in the adhesive strain field having only two independent values. These independent states are usually defined as the first and second principle strain. However, since adhesives are usually discussed in terms of shear strains, the strain state can also be expressed as the maximum shear and average axial strain. With two variables, the unit strain vectors define a circle as shown in Figure 28 and described as strain state angles. This circle can be reduced to a half circle since there is no difference between positive and negative shear strains. If we divide the circle into 18 sectors each sector is 10 °wide.

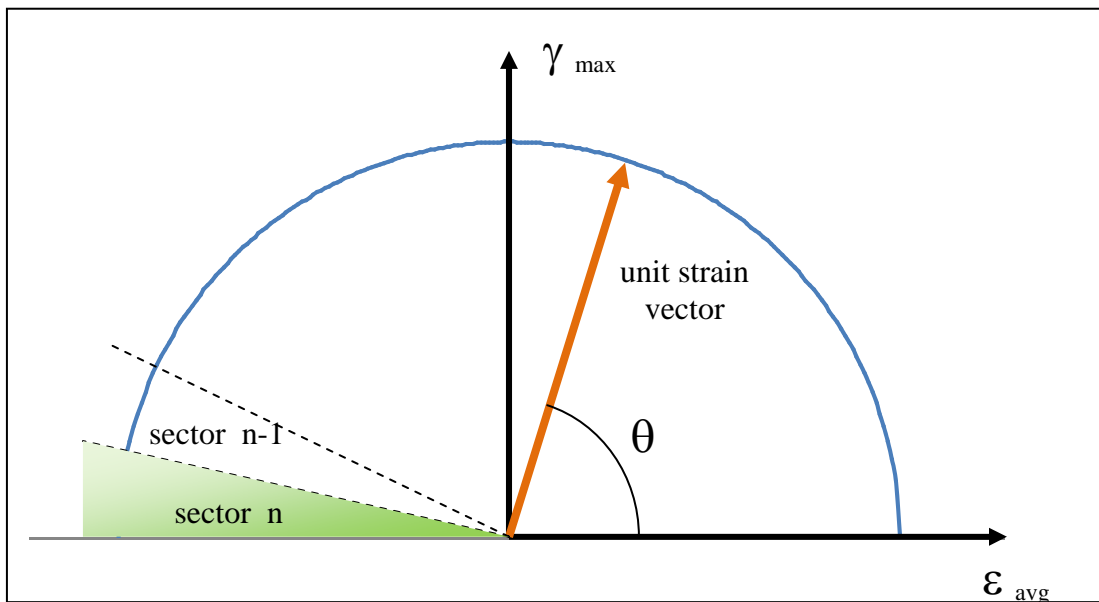


**Figure 28. Two dimensional unit strain vector space divided into discrete strain sectors**

As mentioned before, in the linear range the strain energy density is fully determined by the strain state. To make the FE solution routine more efficient, we do not calculate the strain energy density to find  $U^*$ , instead we may just work with the strain state  $\{\varepsilon\}^*$  directly.

In Ansys, this either cuts out a step into the post-processor or the creation of a custom material model. Instead, a multi-linear elastic model may be used to define the adhesive response (Note: this is only valid without unloading in the model). If each sector is small, the variation of strains is necessarily also small, and  $U^*$  may be considered constant for each sector. In this manner a discrete number of multi-linear models, one for each sector, may be defined and later characterized.

Due to their simplicity, The two models used were bi-linear and tri-linear models with nearly flat end tangent moduli. The reason for the flat end moduli is to simulate a state of high damage where the material is no longer providing much stiffness. The bilinear material adds one unknown per strain sector ( $\varepsilon^*$ ) while the trilinear adds three ( $\varepsilon^*, \varepsilon^2$  and  $E^2$  or  $\sigma^2$ ) to the characterization procedure. For the ease of use in applying the variable limits the tangent modulus  $E^2$  is preferred over the stress  $\sigma^2$ .

Ansys does not have a direct routine defining material response with strain vector, so a multi-step approach must be used to apply this type of material response. The first step is to load the FE model to a point at which the structure is still known to be in a linear state. The strain state of each node is captured and assigned a sector. In Ansys, non-linear material properties may be defined at different temperatures. So, temperature is used as a dummy variable and each node is assigned a temperature according to its strain sector. This ties the material properties to the strain state. The temperatures are ramped into the solution routine so it is best to apply another load which stays well within the linear region of the material response. Finally, the model is loaded to its desired loads which take the model into the non-linear response of the material and structure.

A sample of the temperature, or strain state, profile of test case ALC is shown in Figure 29. In this case, the adhesive properties are broken into 18 strain sectors (each 10 degrees wide) with temperature increments of 100 degrees. Only sectors 8-12, temperatures 800-1200 are present in the material response for this structure. These sectors represent high shear strains with little average axial stress. It is also worth noting that sectors 8, 11 and 12 do not have a high area of presence and will most likely not have a significant impact on the solution.

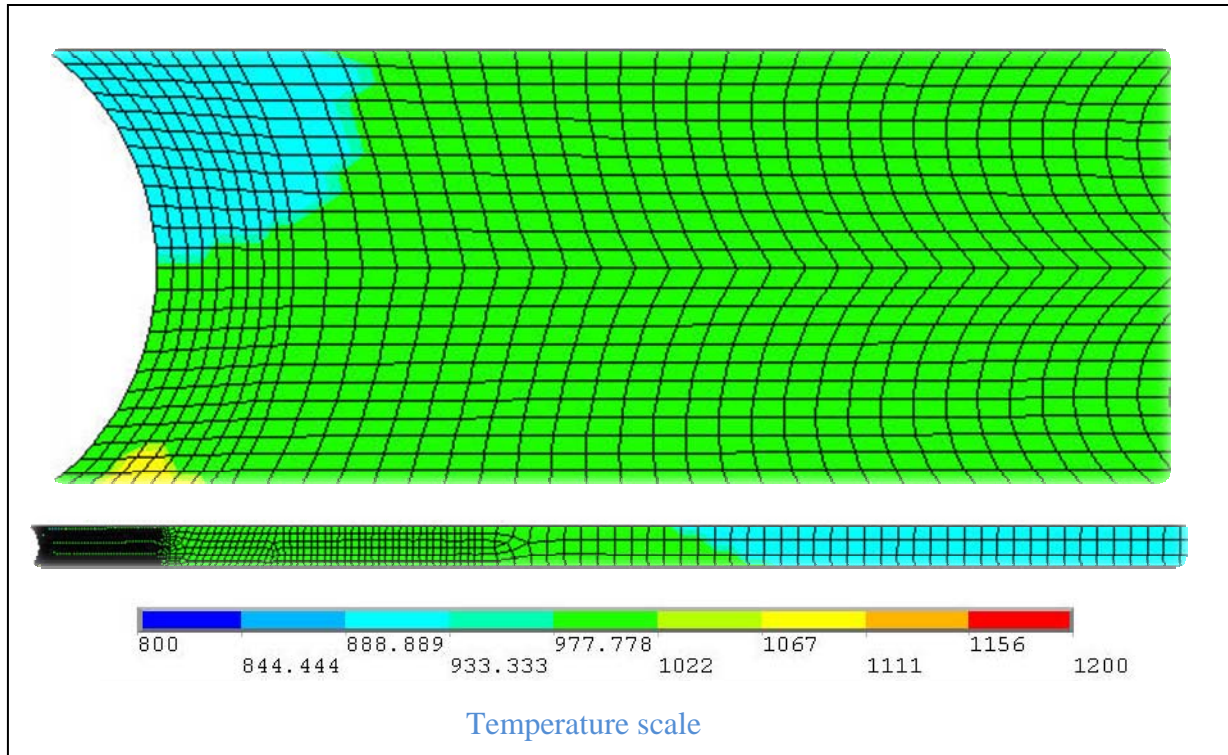


**Figure 29. Example contour plots of nodal temperatures which are representative of the strain sectors defining the material properties of the adhesive (top: closeup of interface region, bottom: wider view)**

### Optimization Procedure

The material response of the adhesive is optimized with respect to the error between the FE model and experimental data. The output data from the experiments are load and displacement. In the FE model, the deflections are input as loads with the resulting reaction forces as output. The absolute difference between the FE force and the experimental load is the error in the FE model. Three points in the response of a test case are chosen to define the nonlinear response of the test. The first point is chosen just at or after the deviation from linear. The third point is chosen as the last point before crack initiation and load drop off and defines the point of maximum pre-crack damage. The second point is chosen as an intermediate point between those two helping define the curvature of the nonlinear path. The objective function is the error at each load point, and explicitly stated below:

$$F_{obj} = \sum abs(P_i - R_i)$$

where  $P_i$  and  $R_i$  are the experimental load and FE reaction force at each load step,  $i$ , respectively.

This simple objective function is expandable to include multiple models with differing geometries. In these cases each model is performed in series with the individual terms summing.

For example, test case series A3Q, A3Ua and A3Ub (which have different adherend thicknesses) are run sequentially for a total of nine error terms in the objective function. In this manner a wider range of strain state responses (sectors) are characterized with more interaction and fidelity.

The variables of the optimization process, the design variables, are those variables which will define the nonlinear material properties. For the bi-linear case, only  $\epsilon^*$  is required for each sector. Thus the total number of design variables is,  $j$ , which is the number of active and significant strain sectors in the model(s). For the tri-linear case the design variables are  $\epsilon^*$ ,  $\epsilon^2$  and  $E^2$ . Here,  $E^2$  is the middle tangent modulus and  $\epsilon^2$  is the strain at which the modulus changes to the nearly flat tangent modulus. It is recommended that the linear model results, with temperatures applied, is analyzed prior to optimization to runs to eliminate unnecessary design variables.

### **Adhesive Characterization Results for FM300**

It was found that a bilinear material response would optimize well for the first and third load points for the ALC test geometry. However, the second intermediate point was more difficult to minimize. To better model the curve in the structures response profile, a tri-linear material response was used. The increase in the number of design variables by a factor of three was found to cause numerous local minima problems during optimization. These local minima were usually found near the input values. Therefore several approaches were attempted to find the best input variables so that the global minimum was found.

The first approach is to treat the adhesive as an isotropic material and optimize the results for each case separately (ALC, A3QS, A3Ua, and A3Ub) using the subtype optimization procedure. This method is an advanced zero order method that only requires the design variable and objective function variables from more than one solution. An approximation of the objective function is then used to estimate the next variable values. The initial values were estimated as reasonable values. This method begins with random changes to the design variables and tends to make large jumps for the next few iterations. The combination of fewer variables and early random jumps removes some of the problems associated with the local minimums. However, these solutions are not unique, which can be observed when viewing all of the design sets in the solution, where several other distinctly different solutions have objective function values very close to the best solution. A plot of the best solution found for each case is shown in Figure 30.

By viewing the design variable solution sets for the individual cases, a common solution set can be estimated as an average of the best design sets. Using the extreme values of those solution sets as the variable limits, the optimization of the material properties for the collective set of tests can be performed. Here, each case is modeled with the current design variables consecutively, and its objective function terms added to the total objective function. The objective function is again optimized using the subtype method. The results for an analysis of the four equal aluminum adherend cases (ALC1, ALC2, A3QS1 and A3QS2) is shown in Figure 30 as, isotropic characterization 1. Each of these cases has a unique Teflon length which changes the FE model enough to have significantly different response. The total error of this characterization was 2%. The relevant values defining this response are,  $E_{\text{linear}} = 153900$  psi (manufacturers

value),  $\epsilon^* = 0.0614$ ,  $E^2 = 57900$  psi, and  $\epsilon^2 = 0.0674$ . The unequal ENF cases, A3Ua and A3Ub were added for an optimization routine which produces the following results,  $\epsilon^* = 0.0607$ ,  $E^2 = 44100$  psi, and  $\epsilon^2 = 0.00621$ . The optimization routine for this analysis used a first gradient method performed on the best results from a set of 30 random solutions.

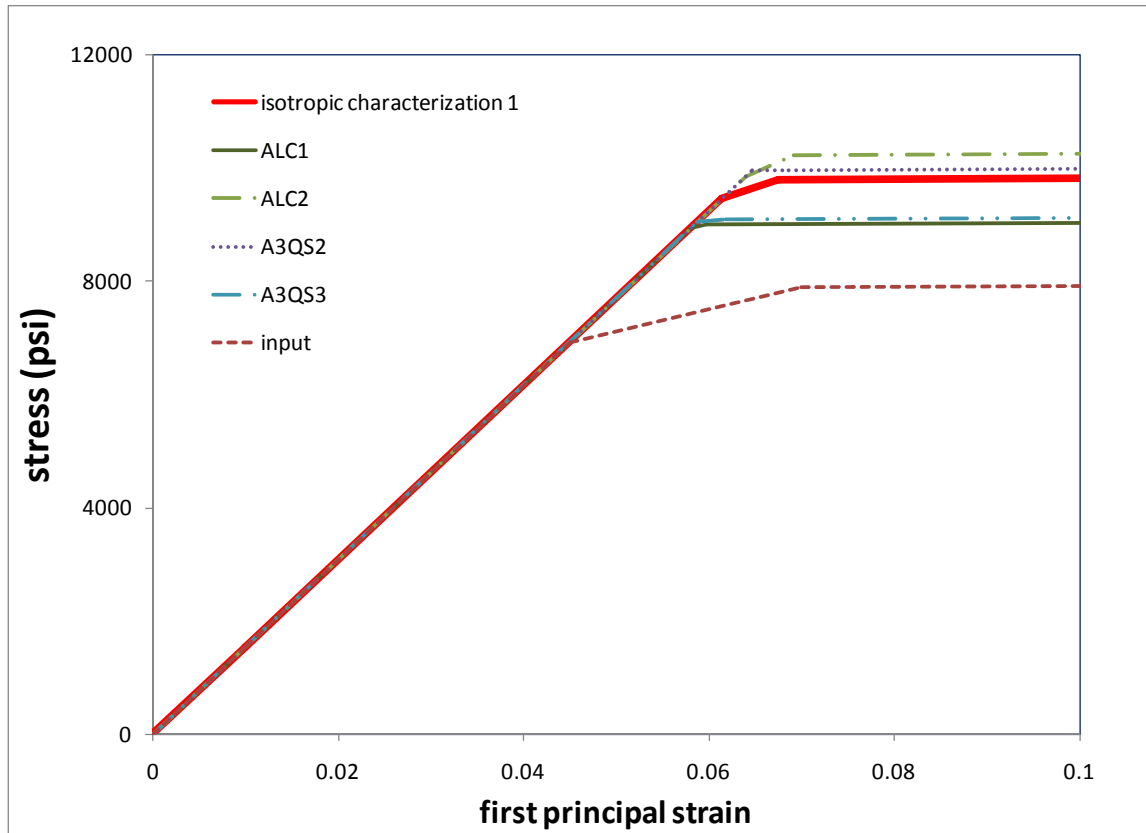


**Figure 30.** optimized solutions for each case using an isotropic non-linear response for the adhesive.

The final step in the characterization process is to separate the response into the strain sectors. Due to time constraints, this process was not finished at the time of writing. However, the strain separated response for the individual sample ALC2 was obtained and plotted compared to the isotropic response in Figure 31. By area, the major stress sectors present in the adhesive are sectors s9 and s10 which are shear dominated sections with some average tension in s9, and compression in s10. The results from this optimization should not be used to model FM300 for several reasons. First several of the sectors do not highly impact the structural response their optimized values can change significantly without affecting the optimization. Secondly, by only optimizing from a single case, the results are not robust and really only ‘work’ for this case. However, these results do highlight the process and forecast the characterization process for strain state dependent characterization.

The damage initiation envelope is shown in Figure 32 as a vector plot. The strain sector gives the strain angle,  $\theta$ , while the magnitude is the value for  $U^*$  (the damage initiation strain energy

density value). The actual values for the sectors s8 through s12 are 614, 439, 388, 497 and 334 lb-in/in<sup>3</sup> respectively.

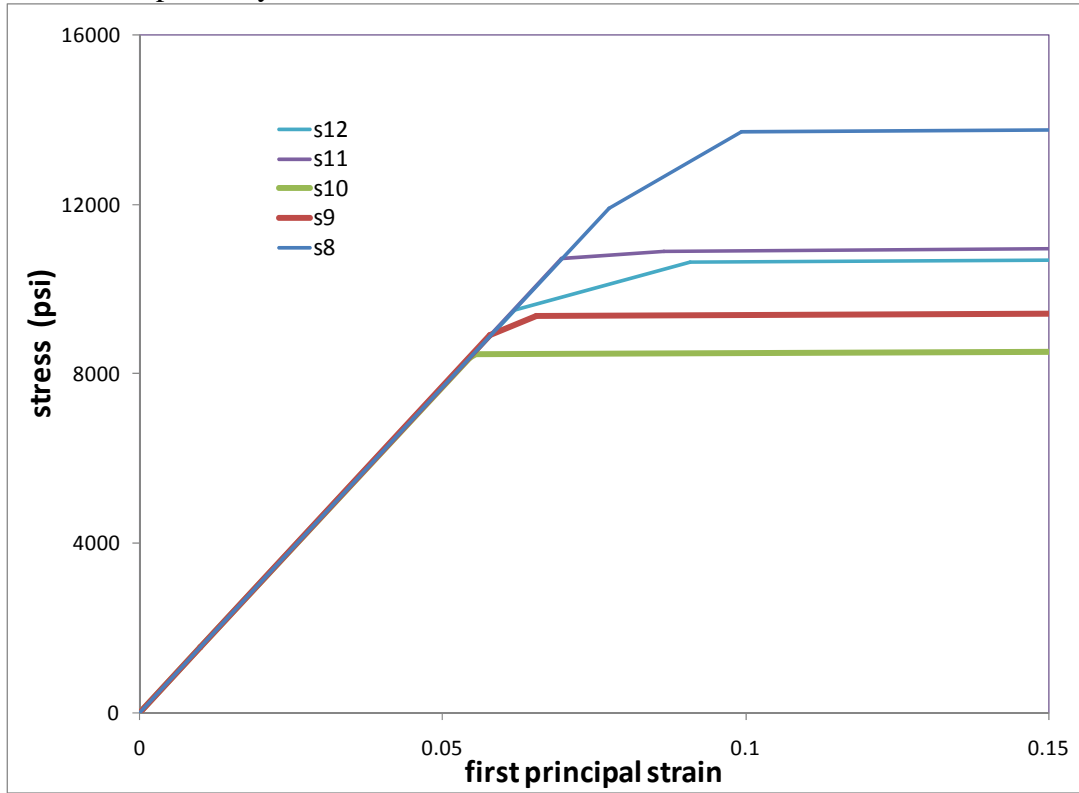


Figure 31. Optimized solution sets for the adhesive nonlinear response for case ALC2

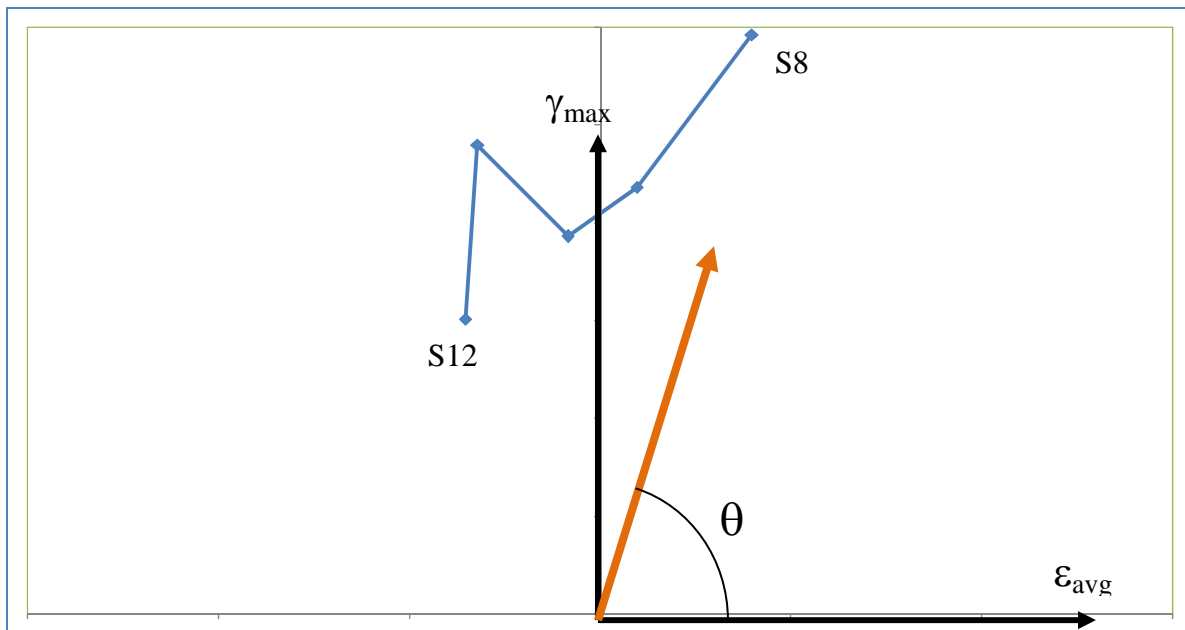


Figure 32. Normalized damage initiation strain energy density ( $U^*$ ) envelope for FM300 characterized by optimization of test case ALC2

## CONCLUSIONS

The present study has taken numerous changes of direction during its course and the conclusions found mirror those differing directions. These efforts included; 1). double lap shear joint analysis; 2). development for the testing methods and geometries of joints in a multi-axial test machine; 3). development of methods and geometries for testing mixed mode bending style joints 4). development of procedures for characterizing the strain state dependent nonlinear response of adhesives 5). characterization of FM300 from ENF style tests.

From the double lap shear joint study, it was found that the load carrying capacity of a joint can be increased by using joints with differing stiffness adhesives (hybrids). A 29% increase was predicted for a double lap shear joint with FM300 & FM400 sections optimized by location and length.

It was found that common joint tests do not take advantage of the new load paths available by testing in a multi-axial test machine. Considerable time was spent developing a suitable test geometry for the MSU-IPL multi-axial test machine. The best sample geometries to control the strain states in the adhesive during a test in a multi-axial testing machine place the bond-line perpendicular to the loading plane. This orientation allows the loading directions to directly control the overall strain state of the adhesive. The most suitable joint geometry for a multi-axial testing machine is a notched Tee-joint. The Tee-joint provides several features that make it a good geometry choice; 1). Proper orientation of the bondline to the loading paths; 2). A stress concentrator that controls the site of damage initiation; 3). Distinct damage initiation sites for different load paths; 4). Slow and stable damage growth.

Twenty Tee-joint tests were performed on either the MSU-IPL or an Instron uni-axial testing machine. The Tee-joints were found to give consistent failure results for the tension load path. The Tee joints test geometry looks to be a promising test geometry for multi-axial testing. However, the MSU-IPL was found to be an unsuitable testing machine for the specific rigors associated with testing joints, and specifically Tee joints. The bonded joints tested the MSU-IPL were too stiff which caused numerous problems in the proper loading of the sample as well as large errors in the data acquired from these tests.

A suitable joint geometry for controlling the adhesive strain states using a uni-axial machine are the mixed mode bending (MMB) style tests, which include the end notch flexure (ENF) and dual cantilever beam (DCB) tests. These tests also place the bond-line in perpendicular to the load direction. These tests place the adhesive into the tension, shear and combined tension shear strain space. Over thirty tests were performed using aluminum/FM300 and carbon-epoxy/FM300 ENF style joints. The carbon-epoxy bond surface, rough or smooth, was found not to have an effect on the failure load of the joint. However, the crack was found to generally propagate faster for the smooth bond surface.

From testing and FE analysis it was found that dominance of the adherend stiffness over the adhesive caused difficulties in characterizing the linear response of the adhesive. In short, any error in the experimental data will become magnified greatly in the characterization process and result in inaccurate linear predictions. However, if the damage is contained to the adhesive, then

damage initiation and growth models may be characterized under certain conditions and assumptions. Using these assumptions, a method for characterizing the nonlinear adhesive properties using an optimization approach with finite element analysis was developed. This method characterizes the material response as a function of the strain state. It also incorporates an optimization routine over several test geometries and experiments to make the characterization results more universal and robust. The nonlinear FM300 adhesive response was characterized for end notch flexure style joints as both an isotropic material and by strain state for a small strain space. The values for the isotropic tri-linear models are defined by the following stress-strain points (9450, 0.0614), (9796, 0.0674) and (9900, 0.2). At the time of writing a second characterization set was found for a larger set of tests made up of the following set of points (9342, 0.0607), (9403, 0.0621) and (9503, 0.2).

## RECOMMENDED FUTURE WORK

In general, adhesives tend to be much compliant than the adherend; however, the joint performance limitations associated with this disparity can potentially be overcome through the use of hybridized and/or gradient adhesives. E.G. introduction of stiff nano particles such as nano carbon platelets and tubes would enable us to functionally tailor the gradient of the adhesive stiffness to mitigate stress singularities associated with edge discontinuities and laminate ply drop-offs. Another approach would be by hybridization of different stiffness adhesives (e.g. FM300 & FM400) to create a functionally stepped gradient adhesive joints with the potential of carrying higher loads.

Through the knowledge gained from the present study, a potential method for studying gradient adhesives has presented itself. First an experimental study on the effects of hybrid double lap shear joints would provide a good starting point for the optimizing the load carrying capacity of hybrid and gradient joints. Secondly, a modified three point bending test would be an intriguing method for studying the load transfer of hybrid joints.

Currently, only two multi-axial testing machines are known to be active at present, the MSU-IPL and the six degree of freedom loader at the Naval Research Laboratories. The current MSU-IPL has limitations due to its design and development. Thus there is not currently a high precision, high load multi-axial testing machine in the university system. The lessons learned during the development of the current IPL, as well as the unique set of talents at MSU makes the production of a multi-axial testing machine intriguing and feasible for MSU.

## REFERENCES

1. Mast, P.W., Nash, G.E., Michopoulos, J., Thomas, R.W., Badaliane, R., Wolock I. "Experimental Determination of Dissipated Energy Density as a Measure of Strain-Induced Damage in Composites." *NRL/FR/6383--92-9369*
2. Parker, J.W., "Development and implementation of a low cost image correlation system to obtain full-field in-plane displacement and strain data", *Master's Thesis*, Department of Mechanical and Industrial Engineering, Montana State University, 2009

3. Hart-Smith, L.J., "Adhesive-bonded double lap joints" *NASA Technical Report 19740005082*, 1974
4. Moorehead, R.B. "Fatigue of Skin-Stiffener Intersections in composite wind turbine blade structures" Department of Mechanical and Industrial Engineering, Montana State University, 2000